CAD MODELS AND FORMULATIONS FOR ELECTRO-/MAGNETO-THERMAL SIMULATION OF POWER SEMICONDUCTOR AND MAGNETIC DEVICES

By

JIA-TZER HSU

A DISSERTATION PRESENTED TO THE GRADUATE SCHOOL
OF THE UNIVERSITY OF FLORIDA IN PARTIAL FULFILLMENT OF THE
REQUIREMENTS FOR THE DEGREE OF DOCTOR OF PHILOSOPHY

UNIVERSITY OF FLORIDA

1995

UNIVERSITY OF FLORIDA LIBRARIES

ACKNOWLEDGEMENTS

I would like to express my deepest gratitude to Dr. Khai D. T. Ngo, the chairman of my supervisory committee, for his support and guidance during this research. I am also very much indebted to Dr. Loc Vu-Quoc, the cochairman of my supervisory committee, for his guidance and encouragement. I also want to thank Dr. J. Kenneth Watson, Dr. Dorothea E. Burk, Dr. Dennis P. Carroll, Dr. Renwei Mei, Dr. Kenneth O and Dr. Carla Schwartz for helpful discussions and for attending my defense.

I also wish to express my greatest love and thanks to my parents and my sister, Dr. Lie-Fern Hsu, for their initial support and encouragement.

TABLE OF CONTENTS

page

ACKNOWLEDGEMENTS ii

ABSTRACT vii

CHAPTERS

1 INTRODUCTION 1

1.1 New Contributions of the Present Work 2

1.2 Circuit Models for Electro-Thermal Simulation 3

1.3 Circuit Models for Magneto-Thermal Simulation 5

2 FORMULATION OF FINITE-ELEMENT CIRCUIT MODELS FOR THERMAL SYSTEMS 7

2.1 Introduction 7

2.2 Coupled Electro-Thermal Equations 9

2.3 Background 13

2.3.1 Finite Element Formulation for Circuit Elements 13

2.3.2 Analogy between Thermal and Circuit Systems 16

2.3.3 Circuit Networks from Symmetric Matrices 17

2.4 Thermal Networks of 1-D Finite Elements 18

2.4.1 Thermal Network of 1-D Linear Element 19

2.4.2 Thermal Network of 1-D Cubic Hermite Element 21

2.5 Thermal Networks of 2-D Finite Elements 24

2.5.1 Thermal Network of 2-D Triangular Element 25

2.5.2 Thermal Network of 2-D Rectangular Element 27

2.6 Thermal Networks of 3-D Finite Elements 29

2.6.1 Thermal Network of 3-D Tetrahedral Element 30

2.6.2 Thermal Network of 3-D Cube Element 32

2.7 Verification 33

2.8 Summary 36

3 FORMULATION OF REDUCED THERMAL CIRCUIT MODELS FOR ELECTRO-THERMAL SIMULATION 37
3.1 Introduction 37
3.2 Reduced Thermal Models by Model Reduction and Substructuring.. 39
3.2.1 Modal Superposition Method 39
3.2.2 Component Mode Synthesis (CMS) 40
3.2.3 Model Error Estimation 43
3.2.4 Ritz Vector Approach 44
3.2.5 Implementation of the CMS Models 47
3.3 Different Approaches 49
3.3.1 An Alternative Method 49
3.3.2 Boundary Element Method 51
3.4 Verification and Application 55
3.4.1 Verification of Reduced Thermal Models 55
3.4.2 Electro-Thermal Simulation 59
3.5 Summary 65
4 BEHAVIORAL MODELING OF POWER SEMICONDUCTOR DEVICES FOR EFFICIENT CIRCUIT SIMULATION 66
4.1 Insulating Gate Bipolar Transistor (IGBT) 66
4.1.1 Introduction 66
4.1.2 Model Description 68
4.1.2.1 Static (DC) model 68
4.1.2.2 Dynamic model 70
4.1.3 Parameter Extraction 73
4.1.3.1 Extraction of R_1 and C_x in the h_1 block 73
4.1.3.2 Extraction of C_{gk}, C_{ag}, and parameters in the V_4 block 74
4.1.4 Model Evaluation and Validation 78
4.2 Vertical Double-Diffused MOSFET (VDMOS) 85
4.2.1 Introduction 85
4.2.2 Model Description 86
4.2.3 Model Evaluation and Validation 92
4.3 Summary 97
5 A RATE-DEPENDENT AND TEMPERATURE-DEPENDENT HYSTERESIS MODEL 98
5.1 Introduction 98
5.2 Physical Background 99
5.2.1 Magnetic Dipole Moment 99

5.2.2 Hysteresis 101
5.3 Model Description 103
5.3.1 Static (DC) Model 104
5.3.1.1 Major loop 107
5.3.1.2 Minor loops 111
5.3.1.3 Wiping-out property 115
5.3.1.4 Inclusion of reversible magnetization 117
5.3.2 Dynamic Model 118
5.4 Parameter Extraction and Implementation 120
5.4.1 Extraction of Static Model Parameters 120
5.4.2 Extraction of Dynamic Model Parameters 123
5.4.3 Implementation 125
5.5 Verification 126
5.6 Summary 132
6 FIELD-BASED FINITE-ELEMENT CIRCUIT MODELS FOR MAGNETIC COMPONENTS WITH HYSTERESIS 133
6.1 Introduction 133
6.2 Fundamentals of Finite-Element Method 134
6.2.1 Derivation of Semidiscrete Equations 135
6.2.2 2-D Linear Triangular Finite Element 142
6.2.3 Boundary Infinite Element 143
6.2.4 Analogy between Magnetic and Circuit Systems 146
6.3 Derivation of Elemental Field Equivalent Subcircuits 146
6.3.1 Elemental Circuit Model of Magnetic Elements 146
6.3.2 Elemental Circuit Models of Conductive and Insulating Elements 148
6.3.3 Elemental Circuit Model of 1-D Infinite Element 150
6.3.4 Interface Circuit Network 151
6.3.5 Modification of the Elemental Circuit Models in Implementation 152
6.3.6 Inclusion of Hysteresis Models in the Magnetic Subcircuit 152
6.4 Field-Based Circuit Modeling Methodology 154
6.5 Verification 157
6.6 Summary 161
7 FINITE-ELEMENT CIRCUIT MODELS FOR MAGNETO-THERMAL SIMULATION OF MAGNETIC DEVICES 162
7.1 Introduction 162
7.2 Coupled Magneto-Thermal Equations 163

7.3 Finite-Element Magneto-Thermal Circuit Models 167
7.3.1 2-D Magneto-Thermal Subcircuits 167
7.3.2 1-D Axisymmetric Magneto-Thermal Subcircuits 169
7.4 Evaluation of Internal Heat Generation 176
7.4.1 Core Loss Density Averaged Over One Cycle 176
7.4.2 Instantaneous Internal Heat Generation 177
7.5 Simulation and Verification 178
7.6 Summary 182
8 CONCLUSION AND FUTURE WORK 183
8.1 Conclusion 183
8.2 Future Work 185
APPENDIX: LEAST-SQUARES METHODS 186
REFERENCES 190
BIOGRAPHICAL SKETCH 203

Abstract of Dissertation Presented to the Graduate School
of the University of Florida in Partial Fulfillment of the
Requirements for the Degree of Doctor of Philosophy

CAD MODELS AND FORMULATIONS FOR ELECTRO-/MAGNETO-THERMAL SIMULATION OF POWER SEMICONDUCTOR AND MAGNETIC DEVICES

By Jia-Tzer Hsu

December 1995

Chairman: Khai D. T. Ngo
Major Department: Electrical and Computer Engineering

As the sizes of the power semiconductor and magnetic devices are getting smaller with advanced technology, thermal effects in these devices are becoming significant. It is important to incorporate thermal effects into the computer simulation of these devices. This dissertation presents several new CAD models and formulations for electro-/magneto-thermal simulation of power semiconductor and magnetic devices using existing circuit simulators.

The finite element method is applied to derive thermal circuit networks equivalent to a discretization of the heat equation. Elemental thermal circuit networks which correspond to the linear and cubic Hermite elements in the 1-D case, to the triangular and rectangular elements in the 2-D case, and to the tetrahedral and cube elements in the 3-D case are developed. To increase the efficiency of the electro-thermal simulation of power electronic circuits and devices, model reduction techniques are further applied to develop reduced thermal circuit models of semiconductor chips, thermal packages, and heat sinks. To obtain efficient power semiconductor models, the Hammerstein model configuration, which includes a nonlinear static block followed by a linear dynamic block, is applied to

model the characteristics of the Insulated Gate Bipolar Transistors (IGBT).

In order to simulate the dynamic magneto-thermal system, a rate-dependent and temperature-dependent hysteresis model is constructed. A finite-element formulation is presented for the development of field-based, geometry-dependent circuit models which enable coupled field/circuit simulation of circuits containing magnetic components with hysteresis. The developed magnetic and thermal circuit models are combined to build 2-D finite-element magneto-thermal circuit models. Axisymmetric formulations are also applied to develop 1-D axisymmetric finite-element magneto-thermal circuit models for efficient magneto-thermal simulation.

CHAPTER 1
INTRODUCTION

Since the electrical and magnetic characteristics of power electronic systems are greatly influenced by the temperature distributions inside the power semiconductor and magnetic devices, it is important to include temperature effects in the computer simulation of power electronic circuits and devices. The relations among the electrical, magnetic, and thermal systems are shown in Fig. 1.1, from which we can see that each individual system has interactions with the other two systems. The coupling is based on the electrical power loss and temperature for the coupled electrical and thermal systems, on the magnetic power loss and temperature for the coupled magnetic and thermal systems, and on the electrical current and voltage waveforms and magnetic inductances for the coupled electrical and magnetic systems.

This thesis presents several new CAD models and formulations for electro-/magneto-thermal simulation of power semiconductor and magnetic devices using existing circuit simulators. These CAD models can give accurate predictions of the performances of power electronic systems. The designed power electronic system can be synthesized

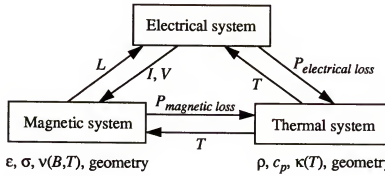

Figure 1.1 The relations among the electrical, magnetic, and thermal systems.

with adequate degree of accuracy before manufacturing; thus, the time and cost in the design and manufacturing can be potentially reduced.

1.1 New Contributions of the Present Work

As corroborated by most of the IEEE Transaction/Conference reviewers of publications of the present work, the new contributions of the present work are listed as follows:

(1) Development of a new technique for formulating finite-element-based thermal circuit models which enable finite-element solutions of the thermal system to be solved by circuit simulators and to be coupled with the electrical network. This new technique and the resulting finite-element-based thermal circuit models are very useful for the users of circuit simulators. The contribution of this work is not only in the developed circuit models, but also in the illustration of the fundamental relations between the finite element method and the circuit theory.

(2) Development of reduced thermal circuit models based on some established methods and a new alternative method. A comment on this work from a reviewer (IEEE Transactions on Circuits and Systems) is as follows: "This work appears to make a significant contribution to the methods of reducing the algorithms associated with the electro-thermal simulation of power devices."

(3) Development of a new methodology for modeling power semiconductor devices for efficient circuit simulation. This work introduces the concept of system identification into the semiconductor area for efficient modeling of power semiconductor devices. As commented by Dr. Hefner in 1995 Power Electronics Specialists Conference, the significant contribution of this work is building a bridge between the semiconductor area and the control area for modeling power semiconductor devices.

(4) Development of a rate-dependent and temperature-dependent hysteresis model for dynamic magneto-thermal simulation. The significant contribution of this work is adding the reversible magnetization, the rate-dependent effects, and the temperature-

dependent effects of the hysteresis phenomena into the classical Preisach model.

(5) Development of field-based finite-element circuit models for magnetic components with hysteresis. These circuit models, which take into account the hysteresis (including minor loops), geometry, frequency, large-signal, and waveshape effects, allow the users of circuit simulators to perform finite-element simulation of magnetic devices coupled with a wide range of circuit topologies in the circuit simulators; thus, they are very useful compared to any existing commercial finite-element software in the magnetic area.

(6) Development of finite-element magneto-thermal circuit models for simulating the dynamically coupled magnetic and thermal systems. The inclusion of thermal effects makes the field-based finite-element circuit models more complete and more useful. Axisymmetric formulations are also applied to develop 1-D axisymmetric finite-element magneto-thermal circuit models for efficient magneto-thermal simulation.

1.2 Circuit Models for Electro-Thermal Simulation

As the size of the semiconductor devices is getting smaller with advanced technology, thermal effects in power semiconductor devices are becoming important. An electro-thermal simulation of complete power electronic systems that include semiconductor chips, thermal packages, and heat sinks is essential for an accurate analysis of the behavior of these systems.

Chapter 2 presents a rational approach to construct thermal circuit networks equivalent to a discretization of the heat equation by the finite element method. Elemental thermal circuit networks are developed, which correspond to the linear and cubic Hermite elements in the 1-D case, to the triangular and rectangular elements in the 2-D case, and to the tetrahedral and cube elements in the 3-D case. These thermal circuit networks are to be connected to the electrical networks of power electronic systems to provide complete electro-thermal models that can be conveniently used in any circuit simulator package.

Verification examples are presented to demonstrate the accuracy of the proposed formulation.

To increase the efficiency of the electro-thermal simulation of power electronic circuits and devices, model reduction techniques are applied in Chapter 3 to develop reduced thermal circuit models of semiconductor chips, thermal packages, and heat sinks. Both the Modal Superposition method and a Component Mode Synthesis method are presented together with a model error estimation and a Ritz vector method. An alternative method based on the Modal Superposition method for substructuring and a boundary element method are also included. The reduced thermal circuit models are verified and implemented in the SABER [Sab92] circuit simulator. The electro-thermal model of a full-bridge converter is simulated employing the proposed approach, and the results discussed.

Although the reduced thermal circuit models did significantly increase the simulation speed of thermal systems, it was found that an electro-thermal simulation still takes a long time and use a huge amount of disk space. This is because the Insulated Gate Bipolar Transistor model developed by Hefner and Blackburn [Hef93] and used for is highly nonlinear and requires several iterations to converge at each time step, and because the time constant of the thermal system is much larger than that of the electrical system.

To obtain efficient power semiconductor device models, Chapter 4 presents methodologies to build behavioral models of power semiconductor devices for efficient circuit simulation. The Hammerstein model configuration, which includes a nonlinear static block followed by a linear dynamic block, is applied to model the static and dynamic characteristics of the Insulated Gate Bipolar Transistors (IGBT). Using least-squares methods, the parameters in the behavioral model can be extracted from the electrical measurements of physical devices or from the circuit simulations of physics-based models. Based on the physical VDMOS model [Kim90], a behavioral VDMOS model is constructed to simplify the mathematical descriptions of the device. The physical VDMOS model, which was modified [Tsa93] and implemented in SABER, is used to extract the model parameters and for comparison. Since the physical VDMOS model

derived by Kim and Fossum [Kim90] is based on the quasi-static approximations, the Hammerstein model configuration, which has been applied to model the dynamics of the IGBT, is not applied to model the VDMOS device. The Hammerstein-based behavioral IGBT model and the physics-based behavioral VDMOS model give satisfactory simulation results for various test circuits in terms of efficiency and accuracy.

1.3 Circuit Models for Magneto-Thermal Simulation

With the development of high-frequency switching mode power supplies, the size of the magnetic devices is shrinking and thermal effects in magnetic devices are becoming important factors in magnetic designs. High-frequency magnetic designs are limited by thermal considerations [Nel92], although conventional low-frequency magnetic designs are only limited by magnetic considerations. To reduce the time and cost in high-frequency magnetic designs, it is desired to have CAD models which could simulate the dynamically coupled magnetic and thermal systems and which could take into account the hysteresis, geometry, frequency, large-signal, and waveshape effects.

In order to simulate the dynamic magneto-thermal system, Chapter 5 presents a rate-dependent and temperature-dependent hysteresis model, which is built by a structure similar to the Hammerstein model. The nonlinear block in the proposed model structure is realized by a modified Preisach model, and the linear dynamic block by a low-pass filter. To modify the classical Preisach model [Pre35], two approaches are applied in this work to allow for magnetization to be both reversible and irreversible. The rate-dependent effects are accounted for by the dynamic block, and the temperature-dependent effects are included in the model by using temperature-dependent model parameters. The model parameters in the proposed model structure are extracted from experimental data using a standard nonlinear least-squares method, i.e., the Levenberg-Marquardt method [Pre92], and a linear least-squares method. It was found that the rate-dependent physical model discussed in Jiles [Jil93] is simply a special case of the present model using a second-order approximation in the dynamic block.

Chapter 6 presents a finite-element formulation for the development of field-based, geometry-dependent circuit models which enable coupled field/circuit simulation of circuits containing magnetic components with hysteresis. SABER templates are developed for the 2-D field equivalent subcircuits representing the dynamic electromagnetic fields in the magnetic (ferrite), conductive (copper), and insulating elements, as well as for an interface network. SABER templates of equivalent subcircuits for the boundary infinite elements [Zie83, Coo89] are also developed to account for the boundary condition at infinity. The inclusion of hysteresis in the finite-element analysis was discussed by Vecchio [Vec82] and Delince et al. [Del94]. This thesis will present an alternative finite-element formulation for hysteresis (including minor loops) which is easier to couple with circuit equations than the formulation in Vecchio [Vec82], and is based on the conventional constitutive law, instead of the new constitutive law in Delince et al. [Del94] which could complicate the calculation.

Chapter 7 presents finite-element magneto-thermal circuit models for accurate predictions of the coupled magnetic and thermal systems. The 2-D triangular thermal circuit models developed in Chapter 2, the rate-dependent and temperature-dependent hysteresis model developed in Chapter 5, and the field-based finite-element magnetic circuit models developed in Chapter 6, are combined to build 2-D finite-element magneto-thermal circuit models. To increase the efficiency of magneto-thermal simulation, axisymmetric formulations are also applied to develop 1-D axisymmetric finite-element magneto-thermal circuit models for magnetic devices made of toroids. The core losses evaluated from the experimentally verified hysteresis model include the hysteresis, eddy-current, and anomalous losses. Using the developed finite-element magneto-thermal circuit models, both the magnetic and the thermal transient phenomena in the magnetic devices can be simulated. To efficiently obtain the steady-state solutions of the coupled magnetic and thermal systems, an iterative process is also applied. Conclusion and future work are discussed in Chapter 8.

CHAPTER 2
FORMULATION OF FINITE-ELEMENT CIRCUIT MODELS FOR THERMAL SYSTEMS

2.1 Introduction

Since the size of the semiconductor devices is becoming smaller with advanced technology, and since the electrical characteristics of power electronic circuits and devices are greatly influenced by the temperature distribution inside the semiconductor devices (self-heating effects), it is important to simulate the coupled electrical and thermal systems simultaneously. Because most of the nonlinear semiconductor device models are implemented in the circuit simulators such as SPICE [Tui88] and SABER [Sab92], it is advantageous to perform electro-thermal simulations inside circuit simulators. In order to put the thermal effects into the circuit simulators, thermal circuit networks are needed. In Fukahori and Gray [Fuk76] and Hefner and Blackburn [Hef93], a finite difference method (FDM) was used to develop thermal models for electro-thermal simulations. In this thesis, we present a rational approach to construct thermal circuit networks equivalent to a discretization of the heat equation by the finite element method (FEM).

It is remarked in Barnes and Lomax [Bar77] and Dautray and Lions [Dau90] that the main advantages of the FEM are that conservation laws are exactly satisfied even by coarse approximations, it is easy to treat irregular geometries, the computational mesh can be graded to be fine in regions of rapid change, local mesh refinement is easier to implement than in the FDM, and higher-order approximations are more readily constructed. Another major difference is that FDM is restricted to the so-called structured meshes, while FEM is suitable for unstructured meshes. It is well known that structured meshes require far more degrees of freedom for a given level of accuracy than unstructured meshes. One disadvantage of using FEM is the greater degree of

programming complexity, which can be avoided by using these FEM-based circuit networks since analytical expressions of the circuit components are used. Using 1-D linear finite elements and lumped masses, it is found that thermal networks based on the FDM are simply special cases of the FEM-based thermal networks. FEM-based thermal networks can produce more accurate results based on the same number of mesh nodes, especially in the 2-D and 3-D problems. Moreover, higher-order finite element approximations can be applied for higher accuracy.

FDM, FEM, FVM (Finite Volume Method), and BEM (Boundary Element Method) are popularly employed to solve partial differential equations (PDEs). Actually, these methods can be viewed as particular cases of the Galerkin projection. FEM is not only used to solve PDEs, but also provides a natural way to solve circuit networks; in fact, circuit elements have been recognized as 0-D (or scalar) finite elements [Bra91]. The ordinary differential equations (ODEs) by finite element (FE) formulation for circuit networks are the same as the nodal equations formulated in traditional circuit simulators. FE formulation can be modified so that results similar to the modified nodal equations [Ho75] or the reduced modified nodal equations [Lee85] can be obtained. Circuit techniques for solving PDEs have been widely discussed in the literature. Circuit technique for semiconductor analysis was proposed to solve semiconductor equations [Sah70, Lin88]. Retarded partial element equivalent circuit was used to solve transmission line problems [Hee92]. Here, we derive the thermal networks based on a FE formulation for electro-thermal simulations. Recently, FEM-based circuit models have been proposed for solving field-circuit problems [Tsu93, Dem92]; however, these models rely on the so-called mutual capacitors, mutual inductors, and mutual resistors. The present thesis proposes a rational approach to construct thermal networks that do not use mutual capacitors/inductors/resistors.

The present FEM-based thermal networks are written as element templates in the SABER circuit simulator. It is convenient to represent a FE discretization in circuit simulators by treating one FE as one lumped circuit component. Accordingly, different types of finite elements are modeled as different types of lumped thermal circuit

components. The contribution of this work is the development of a new technique for formulating FEM-based thermal circuit models which enable finite-element solutions of the thermal system to be solved by circuit simulators and to be coupled with electrical networks. Model reduction techniques to increase the simulation efficiency will be discussed in Chapter 3.

2.2 Coupled Electro-Thermal Equations

As shown in Fig. 2.1, self-heating effects of the semiconductor devices play important roles in the electro-thermal simulation. Moreover, thermal packages, heat sinks, and other electrical components are also important for an accurate electro-thermal

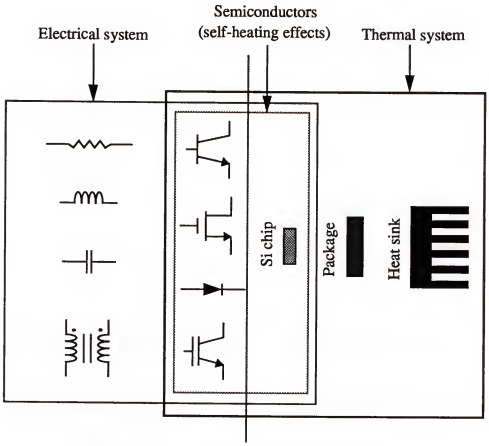

Figure 2.1 Coupled electro-thermal system.

simulation of power electronic circuits and devices. The nonlinear electrical system can be generally expressed as

$$\dot{\boldsymbol{u}} = \boldsymbol{f}(\boldsymbol{u}, \boldsymbol{e}, T)$$
$$\boldsymbol{P} = \boldsymbol{P}(\boldsymbol{u}) \tag{2.1}$$

where $\boldsymbol{u}$ is the vector containing nodal voltages or currents, $\boldsymbol{e}$ the electrical input (e.g., driving voltages for switches), T the temperature, and $\boldsymbol{P}$ the electrical power loss. The nonlinear electrical system is governed by the semiconductor equations (PDEs) and circuit equations (ODEs). The electrical power losses are originated from the heat generation inside the semiconductor devices. Since the semiconductor *pn* junction region, which results in most of the heat generation, is small compared to the whole device region, and is close to the top surface of the Si chip, the electrical power loss can be assumed to be imported from the top boundary of the Si chip, i.e., the electrical power loss is treated as a boundary condition in the thermal problem.

The thermal system is governed by the partial differential equation

$$\mathrm{div}(\kappa\ \mathrm{grad}T) + g = \rho c_p \frac{\partial T}{\partial t} \quad \text{in } \Omega \tag{2.2}$$

with boundary conditions

$$\kappa \mathrm{grad}T \bullet n = \kappa \frac{\partial T}{\partial n} = \frac{P}{A} \text{ on } \Gamma_1 \tag{2.3}$$

$$\kappa \mathrm{grad}T \bullet n = \kappa \frac{\partial T}{\partial n} = h(T_a - T) \text{ on } \Gamma_2 \tag{2.4}$$

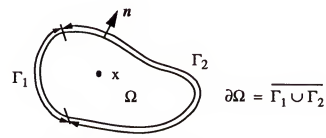

Figure 2.2 Mathematical domain of the thermal problem.

and initial condition

$$T(x, 0) = T_a = 300K \tag{2.5}$$

where $T: \Omega \times \Re_+ \to \Re$ is the temperature (a function of space and time), $g: \Omega \times \Re_+ \to \Re$ the generating heat, $\kappa: \Omega \to \Re$ the thermal conductivity, $\rho: \Omega \to \Re$ the mass density, $c_p: \Omega \to \Re$ the specific heat, $P: \Gamma_1 \times \Re_+ \to \Re$ the input power from boundary Γ_1, A the input power cross section area, h the convection coefficient, n the outward normal vector to the boundary, and T_a the ambient temperature. $\Re$ is the set of real numbers, $\Re_+ := \{t \in \Re \mid t \geq 0\}$, $\Omega \in \Re^s$, where s is the number of space dimension, s=1, 2, 3, and $\partial\Omega = \overline{\Gamma_1 \cup \Gamma_2}$ the closure of the union Γ_1 and Γ_2 (see, e.g. [Hug87]). The boundary condition on Γ_1 is derived from the first law of the thermodynamics, and the convective boundary condition on Γ_2 is derived from the Newton's law of cooling.

The semidiscrete equation of (2.2) - (2.5), derived from a Galerkin finite element projection [Hug87], is

$$\boldsymbol{M}\dot{\boldsymbol{d}} + \boldsymbol{K}\boldsymbol{d} = \boldsymbol{F} \tag{2.6}$$

where $T(x,t) = \sum_{i=1}^{n} d_i(t) N_i(x)$ with $d_i(t)$ being the temperature at node i and $N_i(x)$ being the associated FE basis function. $\boldsymbol{d}(t)$ is the vector containing all nodal temperatures d_i's, and $\dot{\boldsymbol{d}}(t)$ is the time derivative of $\boldsymbol{d}(t)$. The mass matrix $\boldsymbol{M}$ can be realized by capacitor elements, the stiffness matrix $\boldsymbol{K}$ by resistor elements, and the force vector $\boldsymbol{F}$ by current sources, so that thermal effects can be incorporated into circuit simulators. The global matrices $\boldsymbol{M}$, $\boldsymbol{K}$, and $\boldsymbol{F}$ are assembled from the elemental matrices $\boldsymbol{m}_e$, $\boldsymbol{k}_e$, and $\boldsymbol{f}_e$,

$$\boldsymbol{M} = \bigoplus_{e=1}^{nel} \boldsymbol{m}_e \ , \quad \boldsymbol{K} = \bigoplus_{e=1}^{nel} \boldsymbol{k}_e \ , \quad \boldsymbol{F} = \bigoplus_{e=1}^{nel} \boldsymbol{f}_e \tag{2.7}$$

$$\boldsymbol{m}_e = [(m_e)_{ij}], \quad \boldsymbol{k}_e = [(k_e)_{ij}], \quad \boldsymbol{f}_e = [(f_e)_i] \tag{2.8}$$

where $\bigoplus$ denotes the operator of finite-element assemblage, and *nel* is the number of finite elements being assembled. Expressions for the elements of the matrices $\boldsymbol{m}_e$, $\boldsymbol{k}_e$, and $\boldsymbol{f}_e$ are given below:

$$(m_e)_{ij} = \rho c_p A \int_{\Omega_e} N_i N_j d\Omega_e \tag{2.9}$$

$$(k_e)_{ij} = \kappa A \int_{\Omega_e} \text{grad}\, N_i \bullet \text{grad}\, N_j \, d\Omega_e + hA \int_{\Gamma_2} N_i N_j d\Gamma_2 \tag{2.10}$$

$$(f_e)_i = P \int_{\Gamma_1} N_i d\Gamma_1 + hAT_a \int_{\Gamma_2} N_i d\Gamma_2 + A \int_{\Omega_e} g N_i d\Omega_e \tag{2.11}$$

Equation (2.9) and the first term of (2.10) are the conductive terms. The second terms of (2.10) and (2.11) are the convective terms. The first and third terms of (2.11) are the input power and the heat generation terms, respectively.

The thermal network based on FEM is an equivalent circuit network that yields the same semidiscrete system of (nonlinear) ODE's resulting from a Galerkin projection using, e.g., FE basis functions. Similar to FE global matrices, the global thermal network is assembled from elemental networks equivalent to the elemental matrices $\boldsymbol{m}_e$, $\boldsymbol{k}_e$, and $\boldsymbol{f}_e$. Thus only elemental networks need to be considered.

In the circuit simulators, the linearized circuit equations of (2.1) are usually expressed as nodal equations

$$\boldsymbol{Y}(\boldsymbol{d})\boldsymbol{V} = \boldsymbol{I} \tag{2.12}$$

or modified nodal equations [Mcc88], where $\boldsymbol{V}$ is the vector of nodal voltages, $\boldsymbol{I}$ the vector of currents, and the admittance matrix $\boldsymbol{Y}$ is a function of temperatures $\boldsymbol{d}$. The coupled electro-thermal system is shown in Fig. 2.3, from which it can be seen that the coupling between these two systems is based on the power losses $\boldsymbol{P}$ and the nodal temperatures $\boldsymbol{d}$. Note that d_i's in $\boldsymbol{d}$ are treated as system variables in the SABER circuit simulator, and the coupled electrical and thermal systems are solved simultaneously.

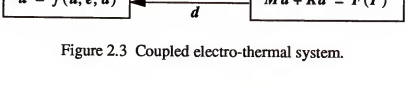

Figure 2.3 Coupled electro-thermal system.

2.3 Background

2.3.1 Finite Element Formulation for Circuit Elements

Figure 2.4(a) shows two separated resistors which can be described by the following two equations:

$$\begin{bmatrix} I_1 \\ I_2 \end{bmatrix} = \frac{1}{R_1}\begin{bmatrix} 1 & -1 \\ -1 & 1 \end{bmatrix}\begin{bmatrix} V_1 \\ V_2 \end{bmatrix} \tag{2.13}$$

$$\begin{bmatrix} I_3 \\ I_4 \end{bmatrix} = \frac{1}{R_2}\begin{bmatrix} 1 & -1 \\ -1 & 1 \end{bmatrix}\begin{bmatrix} V_2 \\ V_3 \end{bmatrix} \tag{2.14}$$

These two resistors and one external current source are assembled in Fig. 2.4(b), and the assembled system is described by

$$\begin{bmatrix} I_1 \\ I_{ext} \\ I_4 \end{bmatrix} = \begin{bmatrix} \frac{1}{R_1} & \frac{-1}{R_1} & 0 \\ \frac{-1}{R_1} & \frac{1}{R_1}+\frac{1}{R_2} & \frac{-1}{R_2} \\ 0 & \frac{-1}{R_2} & \frac{1}{R_2} \end{bmatrix}\begin{bmatrix} V_1 \\ V_2 \\ V_3 \end{bmatrix} \tag{2.15}$$

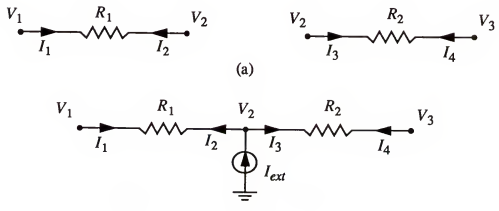

Figure 2.4 (a) Two resistors before assemblage; (b) the assembled system of two resistors and one external current source.

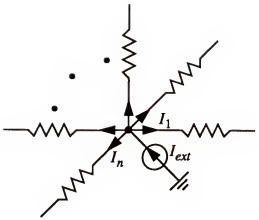

Figure 2.5 A general example of circuit connection, using resistor as an example.

from which it can be seen that the basic rule of the FE assemblage for the circuit elements is the same as the Kirchhoff law, i.e., all currents flowing into the same node sum up to zero. Figure 2.5 shows a general case (using resistors as an example), where the assemblage of the circuit elements is based on

$$\sum_{i=1}^{n} I_i = I_{ext} \tag{2.16}$$

In the FE formulation, every circuit element such as a resistor, a capacitor, an inductor, and a current source is treated as one elemental matrix, and the connection of these circuit elements is described by the assemblage of these elemental matrices. The matrix equations derived from the FE formulation for the circuit networks have the following form [Bra91, Hei91]:

$$\boldsymbol{M}\ddot{\boldsymbol{w}} + \boldsymbol{B}\dot{\boldsymbol{w}} + \boldsymbol{K}\boldsymbol{w} = \boldsymbol{F} \tag{2.17}$$

where $\dot{\boldsymbol{w}} = \boldsymbol{V}$ is the vector of the nodal voltages, $\ddot{\boldsymbol{w}} = \dot{\boldsymbol{V}} = d\boldsymbol{V}/dt$, and $\boldsymbol{w} = \int \boldsymbol{V} dt$. The global matrices $\boldsymbol{M}$, $\boldsymbol{B}$, and $\boldsymbol{K}$ are assembled from the local elemental matrices $\boldsymbol{m}_e$, $\boldsymbol{b}_e$, and $\boldsymbol{k}_e$, and the global vector $\boldsymbol{F}$ from the local elemental vector $\boldsymbol{f}_e$. If one of the element nodes is grounded, then the corresponding row and column in the global matrices will be eliminated. A capacitor element with a value C contributes to a local elemental

matrix $\boldsymbol{m}_e$,

$$\boldsymbol{m}_e = \begin{bmatrix} 1 & -1 \\ -1 & 1 \end{bmatrix} C \tag{2.18}$$

a resistor element with a value R to a local elemental matrix $\boldsymbol{b}_e$,

$$\boldsymbol{b}_e = \begin{bmatrix} 1 & -1 \\ -1 & 1 \end{bmatrix} \left(\frac{1}{R}\right) \tag{2.19}$$

an inductor element with a value L to a local elemental matrix $\boldsymbol{k}_e$,

$$\boldsymbol{k}_e = \begin{bmatrix} 1 & -1 \\ -1 & 1 \end{bmatrix} \left(\frac{1}{L}\right) \tag{2.20}$$

and a current source element with a value I to a local elemental vector $\boldsymbol{f}_e$,

$$\boldsymbol{f}_e = \begin{bmatrix} I \\ -I \end{bmatrix} \tag{2.21}$$

For a linearized h-parameter BJT (bipolar junction transistor) shown in Fig. 2.6, it will

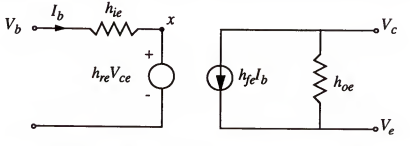

Figure 2.6 *h-parameter* model of the bipolar junction transistor.

contribute to a local elemental matrix $\boldsymbol{b}_e$,

$$\boldsymbol{b}_e = \begin{bmatrix} \dfrac{h_{fe}}{h_{ie}} & h_{oe} - \dfrac{h_{fe}h_{re}}{h_{ie}} & -h_{oe} - \dfrac{h_{fe}(1-h_{re})}{h_{ie}} \\ \dfrac{1}{h_{ie}} & \dfrac{-h_{fe}}{h_{ie}} & \dfrac{-(1-h_{re})}{h_{ie}} \\ \dfrac{-h_{fe}}{h_{ie}} & -h_{oe} + \dfrac{h_{fe}h_{re}}{h_{ie}} & h_{oe} + \dfrac{h_{fe}(1-h_{re})}{h_{ie}} \end{bmatrix} \tag{2.22}$$

where the nodal sequence in $\boldsymbol{b}_e$ is collector, base, and emitter. The internal node x in the h-parameter BJT is eliminated by rudimentary manipulations. It is shown in Brauer et al. [Bra91] that this h-parameter BJT is handled by adding a one-ohm resistor into the model, so that FE formulation can be applied directly. Although it introduces a negligible error by adding this resistor, it is seen that $\boldsymbol{b}_e$ becomes a 5-by-5 matrix since the internal node is not eliminated and one more dimension is introduced by the added resistor. Since nodal equations are obtained through the FE formulation, a voltage source is not a natural element to be formulated into (2.17). Norton theorem is used in Brauer et al. [Bra91] to handle the voltage source with one grounded node. If the voltage source is connected to a circuit component other than the RLC lumped components, then a very small resistor need to be added to the network in order to apply the Norton theorem. This is similar to using a large penalty number in the FEM [Zie89, Hug87]. The corresponding terms of the voltage source in (2.17) can be moved to the right-hand side and incorporated into the $\boldsymbol{F}$ vector. Accordingly, the nodes of the voltage sources are eliminated and extra current sources are added.

2.3.2 Analogy between Thermal and Circuit Systems

Figure 2.7 shows a parallel RC circuit, which can be described by

$$C\begin{bmatrix} 1 & -1 \\ -1 & 1 \end{bmatrix}\begin{bmatrix} \dot{V}_1 \\ \dot{V}_2 \end{bmatrix} + \frac{1}{R}\begin{bmatrix} 1 & -1 \\ -1 & 1 \end{bmatrix}\begin{bmatrix} V_1 \\ V_2 \end{bmatrix} = \begin{bmatrix} I_1 \\ I_2 \end{bmatrix} \tag{2.23}$$

Comparing with the semidiscrete heat equation,

$$\boldsymbol{M}\dot{\boldsymbol{d}} + \boldsymbol{K}\boldsymbol{d} = \boldsymbol{F} \tag{2.24}$$

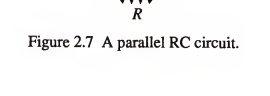

Figure 2.7 A parallel RC circuit.

it is easily seen that the mass matrix $\boldsymbol{M}$ can be realized by capacitor elements, the stiffness matrix $\boldsymbol{K}$ by resistor elements, and the force vector $\boldsymbol{F}$ by current sources. Some simple rules of obtaining the circuit networks from both the symmetric mass matrix and the symmetric stiffness matrix are discussed next.

2.3.3 Circuit Networks from Symmetric Matrices

Based on the above observation, a symmetric global matrix can be decomposed into several elemental matrices, and each elemental matrix can be replaced by a circuit component. Some simple rules to obtain an equivalent circuit network from a symmetric matrix are summarized as follows. A symmetric mass matrix, $\boldsymbol{M} = [m_{ij}]$, can be realized by a capacitor network shown in Fig. 2.8, where

(1) between node i and ground,

$$C_i = \sum_{j=1}^{n} m_{ij} \tag{2.25}$$

(2) between node i and node j,

$$C_{ij} = -m_{ij} \tag{2.26}$$

A symmetric stiffness matrix, $\boldsymbol{K} = [k_{ij}]$, can be realized by a resistor network shown in

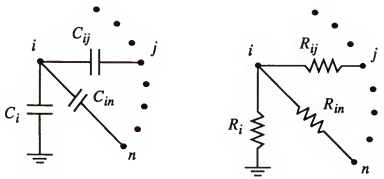

Figure 2.8 A capacitor network from the symmetric mass matrix and a resistor network from the symmetric stiffness matrix.

Fig. 2.8, where

(1) between node i and ground,

$$R_i = 1/\left(\sum_{j=1}^{n} k_{ij}\right) \tag{2.27}$$

(2) between node i and node j,

$$R_{ij} = -1/k_{ij} \tag{2.28}$$

Thermal circuit networks by the finite element method and model reduction techniques are derived from the above simple rules.

2.4 Thermal Networks of 1-D Finite Elements

The length coordinate shown in Fig. 2.9 is used for the derivation of 1-D equivalent thermal networks. The length coordinates are written as

$$L_1 = \frac{\text{length } (px_2^e)}{\text{length } (x_1^e x_2^e)} = \frac{x_2^e - x}{\delta_x}, \quad L_2 = \frac{\text{length } (px_1^e)}{\text{length } (x_1^e x_2^e)} = \frac{x - x_1^e}{\delta_x} \tag{2.29}$$

$(L_1, L_2) = (1, 0)$ at $x = x_1^e$, $(L_1, L_2) = (0, 1)$ at $x = x_2^e$, and $\delta_x = x_2^e - x_1^e$. Equations (2.9) - (2.11) in the 1-D problems can be calculated from the following formula [Zie89]:

$$\int_{\Omega_e} L_1^a L_2^b d\Omega_e = \frac{a!b!}{(a+b+1)!}\delta_x \tag{2.30}$$

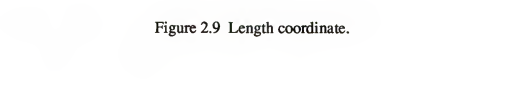

Figure 2.9 Length coordinate.

2.4.1 Thermal Network of 1-D Linear Element

For a 1-D linear element shown in Fig. 7.4, basis functions and their derivatives in the length coordinate are

$$N_1(x) = L_1,\ N_2(x) = L_2,\ N_{1,x}(x) = \frac{-1}{\delta_x},\ N_{2,x}(x) = \frac{1}{\delta_x} \tag{2.31}$$

The conductive terms for the 1-D linear element are calculated to be

$$\boldsymbol{m}_e^d = \rho c_p A \delta_x \begin{bmatrix} \frac{1}{3} & \frac{1}{6} \\ \frac{1}{6} & \frac{1}{3} \end{bmatrix},\quad \boldsymbol{k}_e^d = \frac{\kappa A}{\delta_x} \begin{bmatrix} 1 & -1 \\ -1 & 1 \end{bmatrix} \tag{2.32}$$

where the superscript d represents the conductive terms. From the simple rules discussed in Section 2.3.3, the elemental matrix $\boldsymbol{m}_e^d$ is realized by three capacitors

$$C_1^d = (\boldsymbol{m}_e^d)_{11} + (\boldsymbol{m}_e^d)_{12} = \frac{\rho c_p A \delta_x}{2}$$

$$C_2^d = -(\boldsymbol{m}_e^d)_{12} = \frac{-\rho c_p A \delta_x}{6}$$

$$C_3^d = (\boldsymbol{m}_e^d)_{21} + (\boldsymbol{m}_e^d)_{22} = \frac{\rho c_p A \delta_x}{2} \tag{2.33}$$

and the elemental matrix $\boldsymbol{k}_e^d$ by a resistor

$$R^d = -1/(\boldsymbol{k}_e^d)_{12} = \frac{\delta_x}{\kappa A} \tag{2.34}$$

Since $1/[(\boldsymbol{k}_e^d)_{11} + (\boldsymbol{k}_e^d)_{12}] = 1/[(\boldsymbol{k}_e^d)_{21} + (\boldsymbol{k}_e^d)_{22}]$ = infinite, there is no resistor between the two element nodes and ground. The equivalent conductive circuit network is shown in Fig. 2.10(a).

For the element with the convective boundary (last element for the 1-D case), we can write

$$\boldsymbol{m}_e = \boldsymbol{m}_e^d \bigoplus \boldsymbol{m}_e^v,\quad \boldsymbol{k}_e = \boldsymbol{k}_e^d \bigoplus \boldsymbol{k}_e^v,\quad f_e = f_e^g \bigoplus f_e^v$$

$$\boldsymbol{m}_e^v = 0,\quad \boldsymbol{k}_e^v = hA,\quad f_e^v = hAT_a$$

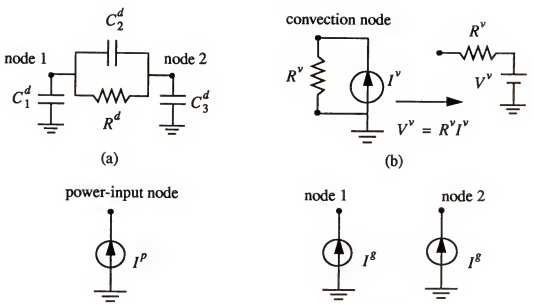

Figure 2.10 *1-D linear element*; (a) Conductive; (b) Convective; (c) Input power; and (d) Heat generation thermal networks.

$$C^v = 0, \quad R^v = 1/hA, \quad I^v = hAT_a \tag{2.35}$$

where the superscript v represents the convective terms, and the superscript g represents the heat generation terms. The convective terms only exist at the end node ($x = L$). The second term in (2.10) is modeled by a resistor $R^v = 1/hA$, and the second term in (2.11) by a current source $I^v = hAT_a$. The equivalent convective thermal network is shown in Fig. 2.10(b), where the Thevenin theorem is applied to obtain an equivalent circuit. For the element with the power input boundary (first element for the 1-D case), we can write

$$f_e = f_e^p \bigoplus f_e^g$$

$$f_e^p = P \tag{2.36}$$

where the superscript p represents the power input terms. The input power only exists at the starting node ($x = 0$), and is modeled by a current source $I^p = P$. Internal heat generation exists at every element, and

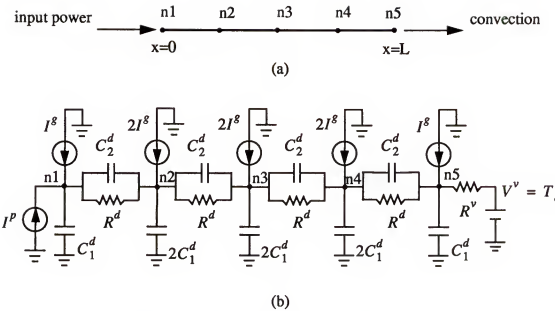

Figure 2.11 (a) 1-D thermal problem and FE discretization; (b) Equivalent thermal network.

$$f_e^g = \frac{gA\delta_x}{2}\begin{bmatrix}1\\1\end{bmatrix} \tag{2.37}$$

The uniform heat generation is modeled by two current sources $I^g = gA\delta_x/2$. The circuit networks for the input power and the uniform heat generation are shown in Fig. 2.10(c) and Fig. 2.10(d), respectively. Figure 2.11 illustrates the assemblage of elemental thermal networks into a global one for a 1-D thermal problem. Capacitors C_2^d can be avoided if lumped mass is used instead of consistent mass [Hug87].

2.4.2 Thermal Network of 1-D Cubic Hermite Element

The basis functions for a 1-D cubic Hermite element in the length coordinate are

$$N_1(x) = L_1^2(1+2L_2), \quad N_2(x) = L_1^2L_2\delta_x$$
$$N_3(x) = (1+2L_1)L_2^2, \quad N_4(x) = -L_1L_2^2\delta_x \tag{2.38}$$

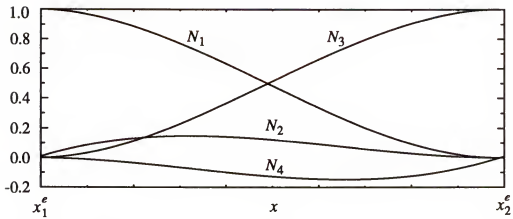

The basis functions satisfy the following conditions:

(1) at node 1 ($x = x_1^e$)

$$N_1 = \frac{dN_2}{dx} = 1, \quad \frac{dN_1}{dx} = N_2 = N_3 = \frac{dN_3}{dx} = N_4 = \frac{dN_4}{dx} = 0 \tag{2.39}$$

(2) at node 2 ($x = x_2^e$)

$$N_3 = \frac{dN_4}{dx} = 1, \quad N_1 = \frac{dN_1}{dx} = N_2 = \frac{dN_2}{dx} = \frac{dN_3}{dx} = N_4 = 0 \tag{2.40}$$

(3) $$N_1 + N_3 = 1 \tag{2.41}$$

(4) $$N_1 x_1^e + N_2 + N_3 x_2^e + N_4 = x \tag{2.42}$$

The conductive terms are calculated to be

$$\boldsymbol{m}_e^d = \rho c_p A \begin{bmatrix} \frac{13}{35}\delta_x & \frac{11}{210}\delta_x^2 & \frac{9}{70}\delta_x & \frac{-13}{420}\delta_x^2 \\ \frac{11}{210}\delta_x^2 & \frac{1}{105}\delta_x^3 & \frac{13}{420}\delta_x^2 & \frac{-1}{140}\delta_x^3 \\ \frac{9}{70}\delta_x & \frac{13}{420}\delta_x^2 & \frac{13}{35}\delta_x & \frac{-11}{210}\delta_x^2 \\ \frac{-13}{420}\delta_x^2 & \frac{-1}{140}\delta_x^3 & \frac{-11}{210}\delta_x^2 & \frac{1}{105}\delta_x^3 \end{bmatrix} \tag{2.43}$$

$$\boldsymbol{k}_e^d = \kappa A \begin{bmatrix} \frac{6}{5\delta_x} & \frac{1}{10} & \frac{-6}{5\delta_x} & \frac{1}{10} \\ \frac{1}{10} & \frac{2\delta_x}{15} & \frac{-1}{10} & \frac{-\delta_x}{30} \\ \frac{-6}{5\delta_x} & \frac{-1}{10} & \frac{6}{5\delta_x} & \frac{-1}{10} \\ \frac{1}{10} & \frac{-\delta_x}{30} & \frac{-1}{10} & \frac{2\delta_x}{15} \end{bmatrix} \tag{2.44}$$

The elemental conductive thermal network for the cubic Hermite element is shown in Fig. 2.12, where

$$R_1^d = \frac{5}{\kappa A},\ R_2^d = \frac{10}{\kappa A \delta_x},\ R_3^d = \frac{-5}{\kappa A},\ R_4^d = \frac{10}{\kappa A \delta_x},\ R_{12}^d = \frac{-10}{\kappa A}$$

$$R_{13}^d = \frac{5\delta_x}{6\kappa A},\ R_{14}^d = \frac{-10}{\kappa A},\ R_{23}^d = \frac{10}{\kappa A},\ R_{24}^d = \frac{30}{\kappa A \delta_x},\ R_{34}^d = \frac{10}{\kappa A}$$

$$C_1^d = \rho c_p A\left(\frac{1}{2}\delta_x + \frac{3}{140}\delta_x^2\right),\quad C_2^d = \rho c_p A\left(\frac{1}{420}\delta_x^3 + \frac{1}{12}\delta_x^2\right)$$

$$C_3^d = \rho c_p A\left(\frac{1}{2}\delta_x - \frac{3}{140}\delta_x^2\right),\quad C_4^d = \rho c_p A\left(\frac{1}{420}\delta_x^3 - \frac{1}{12}\delta_x^2\right)$$

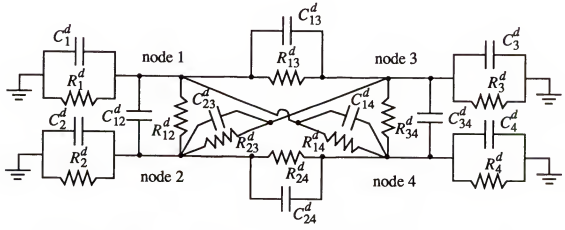

Figure 2.12 Conductive thermal network for a *1-D cubic Hermite element.*

$$C_{12}^d = \rho c_p A\left(\frac{-11}{210}\delta_x^2\right),\quad C_{13}^d = \rho c_p A\left(\frac{-9}{70}\delta_x\right),\quad C_{14}^d = \rho c_p A\left(\frac{13}{420}\delta_x^2\right)$$

$$C_{23}^d = \rho c_p A\left(\frac{-13}{420}\delta_x^2\right),\quad C_{24}^d = \rho c_p A\left(\frac{1}{140}\delta_x^3\right),\quad C_{34}^d = \rho c_p A\left(\frac{11}{210}\delta_x^2\right) \tag{2.45}$$

Nodes 1, 3 give temperatures and nodes 2, 4 give temperature gradients. The convective terms and the input power term are modeled the same as those for the 1-D linear element. The uniform heat generation is modeled by three current sources. Two current sources with value $I_1^g = gA\delta_x/2$ are flowing from ground to node 1 and node 3, and one current source with value $I_2^g = gA\delta_x/12$ is flowing from node 4 to node 2.

2.5 Thermal Networks of 2-D Finite Elements

The area coordinate shown in Fig. 2.13 is used for the derivation of 2-D equivalent thermal networks of Lagrange-type triangular elements. The area coordinates are written as

$$\lambda_i = \frac{\text{area}(pjk)}{\text{area}(123)} = \frac{\alpha_i + \beta_i x + \gamma_i y}{2A_e} \tag{2.46}$$

$$\alpha_i = x_j^e y_k^e - x_k^e y_j^e,\quad \beta_i = y_j^e - y_k^e,\quad \gamma_i = x_k^e - x_j^e \tag{2.47}$$

where i, j, k are the cyclic permutation of 1, 2, 3, and A_e is the area of the local triangular element. Equations (2.9) - (2.11) in the 2-D problems can be calculated from the following

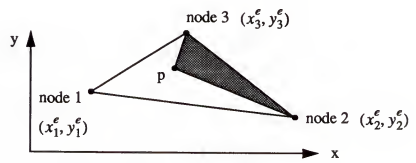

Figure 2.13 Area coordinate.

formula [Zie89]:

$$\int_{\Omega_e} \lambda_1^a \lambda_2^b \lambda_3^c d\Omega_e = \frac{a!b!c!}{(a+b+c+2)!}(2A_e) \tag{2.48}$$

The coordinate transformation shown in Fig. 2.14 is used for the derivation of 2-D equivalent thermal networks of quadrilateral elements (with the rectangular and the square element as special cases). Basis functions in the ξ - η coordinate are

$$N_i = \frac{1}{4}(1+\xi_i\xi)(1+\eta_i\eta)\,, \qquad i = 1 \text{ to } 4 \tag{2.49}$$

where ξ_i and η_i are either +1 or -1, and the following relations hold,

$$x(\xi,\eta) = \sum_{i=1}^{4} N_i(\xi,\eta)x_i^e, \quad y(\xi,\eta) = \sum_{i=1}^{4} N_i(\xi,\eta)y_i^e \tag{2.50}$$

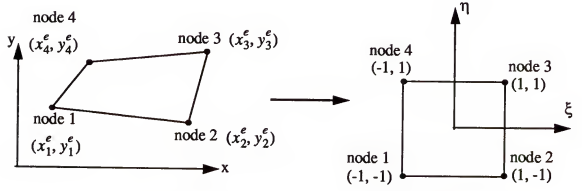

Figure 2.14 Linear mapping from x - y coordinate to ξ - η coordinate

2.5.1 Thermal Network of 2-D Triangular Element

For a linear triangular element, basis functions in the area coordinate are

$$N_i(x,y) = \lambda_i\,, \quad i = 1, 2, 3 \tag{2.51}$$

The conductive terms are calculated to be

$$\boldsymbol{m}_e^d = \frac{\rho c_p A A_e}{12}\begin{bmatrix}2&1&1\\1&2&1\\1&1&2\end{bmatrix}, \quad \boldsymbol{k}_e^d = \frac{\kappa A}{4A_e}\left[k_{ij}\right], \quad i,j = 1 \text{ to } 3 \tag{2.52}$$

where $k_{ij} = \beta_i\beta_j + \gamma_i\gamma_j$. From the simple rules discussed in Section 2.3.3, the elemental matrix $\boldsymbol{m}_e^d$ is modeled by three equal-valued capacitors $C_1^d = \rho c_p A A_e/3$, and by the other three equal-valued capacitors $C_2^d = -\rho c_p A A_e/12$. The elemental matrix $\boldsymbol{k}_e^d$ is modeled by three resistors connected among the element nodes,

$$R_{ij}^d = \frac{-4A_e}{\kappa A(\beta_i\beta_j + \gamma_i\gamma_j)}, \quad 1 \le i < j \le 3 \tag{2.53}$$

No resistor is needed to connect the element nodes to ground, because the sum of those terms in the same row or column in $\boldsymbol{k}_e^d$ is zero. The signs of these three resistors depend on the corresponding triangular angles. An obtuse angle corresponds to a negative resistor, and a right angle to an infinite resistor which represents an open circuit. Otherwise, the corresponding resistor is positive. The elemental conductive thermal network is shown in Fig. 2.15(a). The convective terms are calculated to be

$$\boldsymbol{k}_e^v = hAL_{\Gamma_2}\begin{bmatrix}\frac{1}{3}&\frac{1}{6}\\\frac{1}{6}&\frac{1}{3}\end{bmatrix}, \quad f_e^v = \frac{hAT_aL_{\Gamma_2}}{2}\begin{bmatrix}1\\1\end{bmatrix} \tag{2.54}$$

where L_{Γ_2} is the length of the Γ_2 boundary line in a local triangular element. Similar to the 1-D conduction case, the elemental matrix $\boldsymbol{k}_e^v$ is modeled by two resistors $R_1^v = 2/hAL_{\Gamma_2}$, and one resistor $R_2^v = -6/hAL_{\Gamma_2}$. The vector f_e^v is modeled by two equal-valued current sources $I^v = hAT_aL_{\Gamma_2}/2$. The equivalent convective thermal network is shown in Fig. 2.15(b). The input power is modeled by two equal-valued current sources $I^P = PL_{\Gamma_1}/2$, where L_{Γ_1} is the length of the Γ_1 boundary line in a local triangular element. The uniform heat generation is modeled by three equal-valued current sources $I^g = gAA_e/3$. The circuit networks for the input power and the heat generation

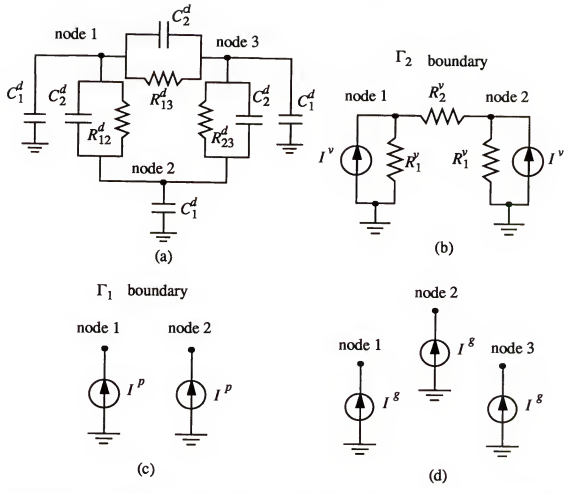

Figure 2.15 2-D triangular element; (a) Conductive; (b) Convective; (c) Input power; (d) Heat generation thermal networks.

are shown in Fig. 2.15(c) and Fig. 2.15(d), respectively.

2.5.2 Thermal Network of 2-D Rectangular Element

Basis functions for the 2-D rectangular (or square) element are shown in (2.49). The conductive terms are calculated to be

$$\boldsymbol{m}_e^d = \frac{\rho c_p A \delta_x \delta_y}{36} \begin{bmatrix} 4 & 2 & 1 & 2 \\ 2 & 4 & 2 & 1 \\ 1 & 2 & 4 & 2 \\ 2 & 1 & 2 & 4 \end{bmatrix} \tag{2.55}$$

$$k_e^d = \frac{\kappa A}{6}\begin{bmatrix} 2\left(\frac{\delta_x}{\delta_y}+\frac{\delta_y}{\delta_x}\right) & \left(\frac{\delta_x}{\delta_y}-\frac{2\delta_y}{\delta_x}\right) & \left(-\frac{\delta_x}{\delta_y}-\frac{\delta_y}{\delta_x}\right) & \left(-\frac{2\delta_x}{\delta_y}+\frac{\delta_y}{\delta_x}\right) \\ \left(\frac{\delta_x}{\delta_y}-\frac{2\delta_y}{\delta_x}\right) & 2\left(\frac{\delta_x}{\delta_y}+\frac{\delta_y}{\delta_x}\right) & \left(-\frac{2\delta_x}{\delta_y}+\frac{\delta_y}{\delta_x}\right) & \left(-\frac{\delta_x}{\delta_y}-\frac{\delta_y}{\delta_x}\right) \\ \left(-\frac{\delta_x}{\delta_y}-\frac{\delta_y}{\delta_x}\right) & \left(-\frac{2\delta_x}{\delta_y}+\frac{\delta_y}{\delta_x}\right) & 2\left(\frac{\delta_x}{\delta_y}+\frac{\delta_y}{\delta_x}\right) & \left(\frac{\delta_x}{\delta_y}-\frac{2\delta_y}{\delta_x}\right) \\ \left(-\frac{2\delta_x}{\delta_y}+\frac{\delta_y}{\delta_x}\right) & \left(-\frac{\delta_x}{\delta_y}-\frac{\delta_y}{\delta_x}\right) & \left(\frac{\delta_x}{\delta_y}-\frac{2\delta_y}{\delta_x}\right) & 2\left(\frac{\delta_x}{\delta_y}+\frac{\delta_y}{\delta_x}\right) \end{bmatrix} \tag{2.56}$$

where δ_x and δ_y are the length and the width of the rectangular element, respectively. The conductive thermal network is shown in Fig. 2.16, where

$$C_1^d = \frac{1}{4}\rho c_p A\delta_x\delta_y\,, \quad C_2^d = \frac{-1}{18}\rho c_p A\delta_x\delta_y\,, \quad C_3^d = \frac{-1}{36}\rho c_p A\delta_x\delta_y \tag{2.57}$$

$$R_1^d = \frac{6}{\kappa A\left(\frac{2\delta_x}{\delta_y}-\frac{\delta_y}{\delta_x}\right)}, \quad R_2^d = \frac{6}{\kappa A\left(\frac{-\delta_x}{\delta_y}+\frac{2\delta_y}{\delta_x}\right)}, \quad R_3^d = \frac{6}{\kappa A\left(\frac{\delta_x}{\delta_y}+\frac{\delta_y}{\delta_x}\right)} \tag{2.58}$$

For a square element, set $\delta_x = \delta_y = \delta$. The condition for R_1^d and R_2^d to be positive is

$$\frac{1}{\sqrt{2}} < \frac{\delta_x}{\delta_y} < \sqrt{2} \tag{2.59}$$

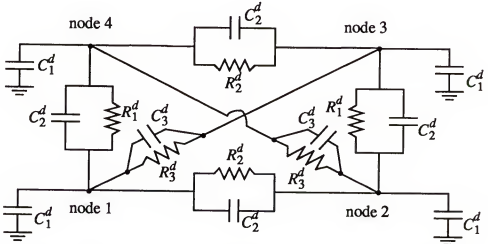

Figure 2.16 Conductive thermal network for a *2-D rectangular element.*

Circuit models for the convective terms and the input power are the same as those for the 2-D linear triangular element. The uniform heat generation is modeled by four equal-valued current sources $I^g = gA\delta_x\delta_y/4$.

2.6 Thermal Networks of 3-D Finite Elements

The volume coordinate shown in Fig. 2.17 is used for the derivation of 3-D equivalent thermal networks of Lagrange-type tetrahedral elements. The volume coordinates are written as

$$V_i = \frac{\text{volume}(pjkl)}{\text{volume}(1234)} = \frac{\alpha_i + \beta_i x + \gamma_i y + \zeta_i z}{6V_e} \tag{2.60}$$

where i, j, k, l are the cyclic permutation of 1, 2, 3, 4, V_e is the volume of the local tetrahedral element, and α_i, β_i, γ_i, ζ_i, $i = 1$ to 4, can be found in [Zie89]. Note that the ordering of the nodal numbers must follow a right-hand rule. Equations (2.9) - (2.11) in the 3-D problems can be calculated from the following formula [Zie89]:

$$\int_{\Omega_e} V_1^a V_2^b V_3^c V_4^d d\Omega_e = \frac{a!b!c!d!}{(a+b+c+d+3)!}(6V_e) \tag{2.61}$$

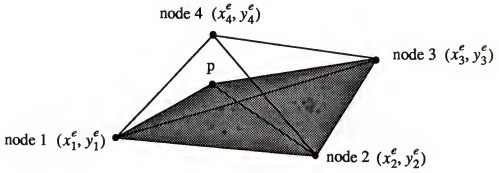

Figure 2.17 Volume coordinate.

2.6.1 Thermal Network of 3-D Tetrahedral Element

For a linear tetrahedral element, basis functions in the volume coordinate are

$$N_i(x, y, z) = V_i, \quad i = 1 \text{ to } 4 \tag{2.62}$$

The conductive terms are calculated to be

$$\boldsymbol{m}_e^d = \frac{\rho c_p A V_e}{20}\begin{bmatrix} 2 & 1 & 1 & 1 \\ 1 & 2 & 1 & 1 \\ 1 & 1 & 2 & 1 \\ 1 & 1 & 1 & 2 \end{bmatrix}, \quad \boldsymbol{k}_e^d = \frac{\kappa A}{36 V_e}\left[k_{ij}\right], \quad i, j = 1 \text{ to } 4 \tag{2.63}$$

where $k_{ij} = \beta_i\beta_j + \gamma_i\gamma_j + \zeta_i\zeta_j$. The conductive thermal network is shown in Fig. 2.18(a), where

$$C_1^d = \frac{\rho c_p A V_e}{4}, \quad C_2^d = \frac{-\rho c_p A V_e}{20} \tag{2.64}$$

$$R_{ij}^d = \frac{-36 V_e}{\kappa A(\beta_i\beta_j + \gamma_i\gamma_j + \zeta_i\zeta_j)}, \quad 1 \le i < j \le 4 \tag{2.65}$$

The convective terms are calculated to be

$$\boldsymbol{k}_e^v = \frac{hAA_{e,\Gamma_2}}{12}\begin{bmatrix} 2 & 1 & 1 \\ 1 & 2 & 1 \\ 1 & 1 & 2 \end{bmatrix}, \quad \boldsymbol{f}_e^v = \frac{hAA_{e,\Gamma_2}T_a}{3}\begin{bmatrix} 1 \\ 1 \\ 1 \end{bmatrix} \tag{2.66}$$

where A_{e,Γ_2} is the area of the Γ_2 boundary surface in a tetrahedral element. The convective thermal network is shown in Fig. 2.18(b), where

$$R_1^v = \frac{3}{hAA_{e,\Gamma_2}}, \quad R_2^v = \frac{-12}{hAA_{e,\Gamma_2}}, \quad I^v = \frac{hAA_{e,\Gamma_2}T_a}{3} \tag{2.67}$$

The input power is modeled by three equal-valued current sources $I^p = A_{e,\Gamma_1}P/3$, where A_{e,Γ_1} is the area of the Γ_1 boundary surface in a local tetrahedral element, and the

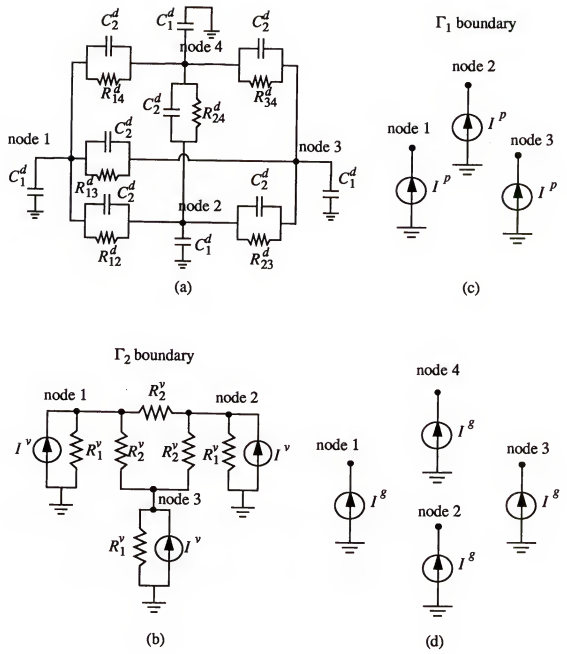

Figure 2.18 *3-D tetrahedral element;* (a) Conductive; (b) Convective; (c) Input power; (d) Heat generation thermal networks.

uniform heat generation is modeled by four equal-valued current sources $I^g = gAV_e/4$. The circuit network for the input power and heat generation are shown in Fig. 2.18(c) and Fig. 2.18(d), respectively.

2.6.2 Thermal Network of 3-D Cube Element

Since the 3-D conductive thermal network is too complicated to draw here, node 1 in Fig. 2.19(a) is used as a reference node to illustrate the connections. The conductive terms for the cube element are modeled by sixteen resistors and thirty-six capacitors. Only eight capacitors are needed if lumped mass is used instead of consistent mass. Resistors among the neighboring nodes, such as nodes 2, 4, 5 to node 1, are infinite and therefore are open. Sixteen resistors among the non-neighboring nodes, such as nodes 3, 6, 7, 8 to node 1, have the value $R^d = \kappa A\delta/12$, where δ is the length of the cube element. Eight equal-valued capacitors $C_1^d = \rho c_p A\delta^3/8$ connect the eight element nodes to ground. Twelve equal-valued negative capacitors $C_2^d = -\rho c_p A\delta^3/54$ are connected among the neighboring nodes, such as nodes 2, 4, 5 to node 1, twelve equal-valued negative capacitors $C_3^d = -\rho c_p A\delta^3/108$ are connected among the 2D-diagonal nodes, such as nodes 3, 6, 8 to node 1, and four equal-value negative capacitors $C_4^d = -\rho c_p A\delta^3/216$ are connected among the 3D-diagonal nodes, such as node 7 to node 1. The convective terms are calculated to be

$$k_e^v = \frac{hA\delta^2}{36}\begin{bmatrix} 4 & 2 & 1 & 2 \\ 2 & 4 & 2 & 1 \\ 1 & 2 & 4 & 2 \\ 2 & 1 & 2 & 4 \end{bmatrix}, \quad f_e^v = \frac{hAT_a\delta^2}{4}\begin{bmatrix} 1 \\ 1 \\ 1 \\ 1 \end{bmatrix} \tag{2.68}$$

The equivalent convective thermal network is shown in Fig. 2.19(b), where

$$R_1^v = \frac{4}{hA\delta^2}, \quad R_2^v = \frac{-18}{hA\delta^2}, \quad R_3^v = \frac{-36}{hA\delta^2}, \quad I^v = \frac{hAT_a\delta^2}{4} \tag{2.69}$$

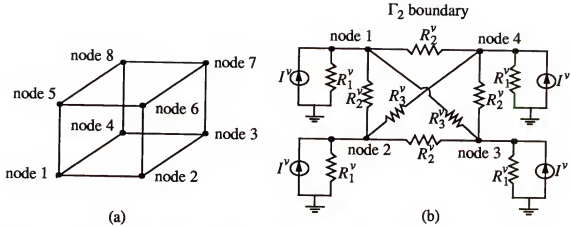

Figure 2.19 (a) A cube element; (b) Convective thermal network for a cube element.

The input power is modeled by four equal-valued current sources $I^P = P\delta^2/4$, and the uniform heat generation by eight equal-valued current sources $I^g = gA\delta^3/8$. Capacitors C_2^d, C_3^d, and C_4^d can be avoided if lumped mass is used instead of consistent mass.

2.7 Verification

FEM-based thermal networks are written as element templates in the SABER circuit simulator, and thermal package models are built by these element templates. A nonlinear resistor template is used to account for the nonlinear thermal conductivity of silicon [Hef93], i.e.,

$$\kappa(T) = 1.5486\left(\frac{300}{T}\right)^{4/3} \tag{2.70}$$

A 2-D mesh generator is used to produce a mesh of triangular elements, and programs (/thesis_programs/saber_fem.m) are written to automatically generate SABER input files. The coupled electrical and thermal systems are solved simultaneously by the built-in numerical solvers in SABER. The thermal circuit networks for the 1-D FE's are verified by analytical solutions for linear problems; the results are shown in Figs. 2.20 and

2.21. Using the method of separation of variables [Ozi80], the analytical solution for the 1-D thermal problem is derived as

$$T(x,t) = \frac{P}{\kappa A}(1-x) + \frac{P}{hA} + T_a + \sum_{n=1}^{\infty} D_n \exp\left(\frac{-\kappa\lambda_n^2 t}{\rho c_p}\right)\cos(\lambda_n x) \tag{2.71}$$

where λ_n satisfies

$$\lambda_n \tan(\lambda_n) = \frac{h}{\kappa} \tag{2.72}$$

and

$$D_n = \frac{4P\{h[\cos(\lambda_n) - 1] - \kappa\lambda_n \sin(\lambda_n)\}}{\kappa h \lambda_n A[2\lambda_n + \sin(2\lambda_n)]} \tag{2.73}$$

The tested 1-D problem is shown in Fig. 2.11(a); the parameters used are: κ = 3.846 $W/(cm-K)$, ρ = 8.857 g/cm^3, c_p = 0.386 $J/(g\text{-}K)$, P = 100 W, A = 0.6451 cm^2, L = 2.54 cm, and element number = 8. The tested 2-D problem which only consists of the Si chip and the TO247 package, taken from a reference paper [Hef93], is shown in Fig. 2.22. The properties for the Si chip are: κ = 1.5486 $W/(cm-K)$, ρ = 2.33 g/cm^3, c_p = 0.7 $J/(g-K)$, and thickness = 0.05 cm; and those for the TO247 package are: κ = 4 $W/(cm-K)$, ρ = 8.9 g/cm^3, c_p = 0.39 $J/(g-K)$, and thickness = 0.2 cm. The thermal networks for the 2-D FE's are verified by results from the ANSYS simulator; the results are shown in Fig. 2.23. Simulation results from SABER and from ANSYS are similar.

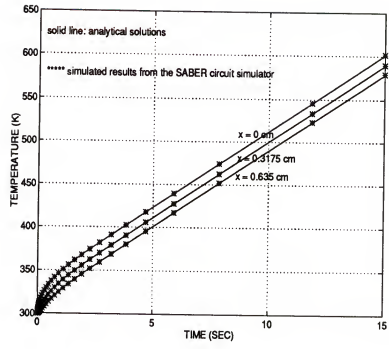

Figure 2.20 Verification of 1-D thermal circuit networks: $h = 1.55 \times 10^{-3}$ W/cm^2-K.

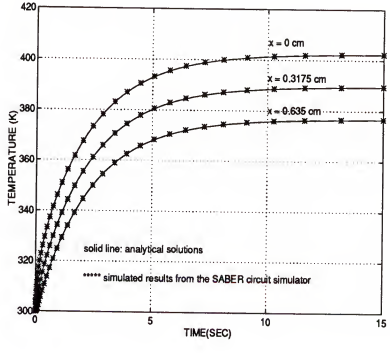

Figure 2.21 Verification of 1-D thermal circuit models: h = infinite.

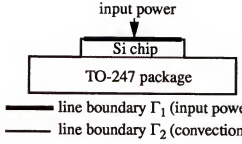

Figure 2.22 One example of 2-D thermal problems.

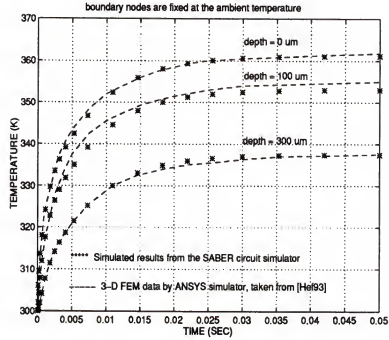

Figure 2.23 Verification of 2-D thermal circuit networks.

2.8 Summary

A rational formulation of the thermal circuit networks by the finite element method has been presented. These FEM-based thermal circuit networks are implemented in the SABER circuit simulator, and simulation results are verified with the analytical solutions for the 1-D case, and by the results from a FEM code for the 2-D case. Different types of finite elements are modeled as different types of lumped thermal circuit components, so that finite element solutions of the thermal system are ready to be coupled with the electrical system in the electro-thermal simulation.

CHAPTER 3
FORMULATION OF REDUCED THERMAL CIRCUIT MODELS FOR ELECTRO-THERMAL SIMULATION

3.1 Introduction

Using the thermal circuit networks derived using the Finite Element Method of Chapter 2, model reduction techniques are further applied to derive the reduced thermal circuit networks, which increase the simulation speed while maintaining good accuracy. Model reduction techniques have been widely employed in the areas of control and structural dynamics. A plethora of references is available, such as model reduction using singular perturbation [Kok76], balanced realizations [Moo81], cost-equivalent realization [Ske88], oblique projection [Vil87], and Schur decomposition [Saf89, Rac92]. AWE (Asymptotic Waveform Evaluation), a moment-matching technique based on the Pade approximation [Pil90], was applied for electro-thermal simulation [Ver93]. However, model reduction based on the Pade approximation may produce unstable poles. Modified approaches for stable AWE method are discussed in Chiprout and Nakhla [Chi92] and Anastasakis et al. [Ana92]. Both the Modal Superposition (MS) method and the Component Mode Synthesis (CMS) method have been developed to reduce computational models in structural dynamics. The primary advantage of these methods is the ability to choose fewer generalized coordinates, while still yielding satisfactory results. An important step in the MS method is to identify the dominant modes for retention in the reduced model. These modes can be determined a priori by a modal cost analysis [Ske80, Ske83], or a model error analysis [You93]. The idea of the CMS method is to find reduced models for various substructures independently, and to use compatibility conditions to connect these reduced substructure models. CMS methods with fixed interfaces [Hur65, Cra68] and free interfaces [Gol69, Hou69, Dow72, Mac71, Rub75, Hin75], as well as

hybrid methods [Mac71, Far92] have been developed in the last three decades. Other references on CMS methods may also be found in the literature [Ben71, Kuh74, Mei81, Kub82, Cra85, Sua88, Leu88, Mei91, Sua91, Mei92]. Domain decomposition [Ben91, Ewi93, Cha92] using parallel processors is also a good approach for efficient computation. In fact, domain decomposition techniques and substructuring techniques share similar ideas.

This thesis applies the MS and CMS method with fixed interfaces (which will be simply referred here to as the CMS method for abbreviation) for linear thermal systems. One significant advantage of the MS method is that the governing differential equations for the reduced model become decoupled, and can be solved easily. In the CMS method, silicon chips, thermal packages and heat sinks are treated as substructures and reduced substructure models are then developed. Since thermal networks are in general linear, and normally much larger than the electrical networks in terms of the number of unknowns, the efficiency of the electro-thermal simulation of power electronic circuits and devices can be considerably increased by reducing the dimension of the thermal networks. Based on the MS method, the thesis discusses an alternative method to derive the reduced substructure models for the thermal systems. A Boundary Element Method is also applied in this work for solving the steady-state solutions of the thermal system. The matrix resulting from the Boundary Element Method contains only the boundary nodes and is smaller than that using the Finite Difference Method or the Finite Element Method.

To apply the MS and CMS methods, an eigenvalue problem of each substructure must be solved. Such computation is in general intensive. Wilson et al. [Wil82, Wil86] presented an efficient algorithm of generating important (substructure) modes by using a set of special Ritz vectors for the MS (CMS) method. These special Ritz vectors, which are load-dependent, will assure that the important modes are not neglected. Wilson's work demonstrated improved accuracy with fewer Ritz vectors as compared to the use of eigenvectors. A proof of the convergence of the basic Ritz procedures was presented in Arnold and Citerley [Arn85]. Craig et al. [Cra88, Su89, Su91] presented another special Ritz vectors, called Block-Krylov vectors, for the CMS method in the structural model

reduction. It is shown in Su and Craig [Su89] that the method of using Krylov vectors preserves the moment-matching property. A stable moment-matching procedure based on the second-order formulation is also discussed there.

The contribution of the present work is to provide an efficient methodology for design engineers to analyze circuit systems that are coupled with thermal components using circuit analysis programs, such as SABER.

3.2 Reduced Thermal Models by Model Reduction and Substructuring

Since the mass matrix $\boldsymbol{M}$ and the stiffness matrix $\boldsymbol{K}$ by the FE formulation are symmetric and (semi-)positive-definite, it is advantageous to apply the MS and CMS methods for model reduction. Based on the simple rules discussed in Section 2.3.3, reduced thermal networks can be obtained from the derived reduced matrices.

3.2.1 Modal Superposition Method

The corresponding eigenvalue problem of the semi-discrete heat equation,

$$\boldsymbol{M}\dot{\boldsymbol{d}} + \boldsymbol{K}\boldsymbol{d} = \boldsymbol{F} \tag{3.1}$$

is

$$(\boldsymbol{K} - \lambda_l \boldsymbol{M})\phi_l = 0 \tag{3.2}$$

where $\{\lambda_l\}$'s are the eigenvalues or poles, and $\{\phi_l\}$'s are the corresponding eigenvectors. $l \in \{1, 2, \ldots, n\}$. Assume that $0 \le \lambda_1 \le \lambda_2 \le \ldots \le \lambda_n$. From the orthogonality of the eigenvectors of the associated eigenvalue problem, we have

$$\phi_i^T \boldsymbol{M} \phi_j = \delta_{ij} \quad \text{and} \quad \phi_i^T \boldsymbol{K} \phi_j = \lambda_i \delta_{ij} \tag{3.3}$$

where $\delta_{ij} = 1$ for $i = j$ and $\delta_{ij} = 0$ for $i \neq j$. We have $\boldsymbol{d} = \Phi_n \boldsymbol{p}$, where $\Phi_n = [\phi_1 \ \phi_2 \ \ldots \ \phi_n]$ is an n-by-n matrix, and $\boldsymbol{p}$ an n-by-1 vector. Retaining m dominant poles with $m < n$, i.e., let $\boldsymbol{d} \approx \Phi_m \tilde{\boldsymbol{p}}$ where $\Phi_m = [\phi_1 \ \phi_2 \ \ldots \ \phi_m]$ is an n-by-m

matrix, the n governing equations are reduced to m equations given by

$$\boldsymbol{I}_m \ddot{\tilde{\boldsymbol{p}}} + \Lambda_m \tilde{\boldsymbol{p}} = \boldsymbol{\Phi}_m^T \boldsymbol{F} \tag{3.4}$$

where $\boldsymbol{I}_m$ is an m-by-m identity matrix, $\Lambda_m = \text{diag}[\lambda_1 \ \lambda_2 \ \ldots \ \lambda_m]$, and $\tilde{\boldsymbol{p}}$ an m-by-1 vector. The vector $\tilde{\boldsymbol{p}}$ contains new generalized coordinates with initial values $\tilde{\boldsymbol{p}}(0) = \boldsymbol{\Phi}_m^T \boldsymbol{M} \boldsymbol{d}(0)$. The configuration of the equivalent circuit network for the reduced model is shown in Fig. 3.1. The passive network in the new coordinate is simply m uncoupled parallel-RC circuits connecting m nodes to ground. The values of the capacitor and the resistor in node i are 1 and $1/\lambda_i$, respectively. The MS method is applied to the thermal system as a whole. In the CMS method, reduced models for substructures with fixed interfaces are first developed, then several reduced substructure models are combined (synthesized) into the final reduced model.

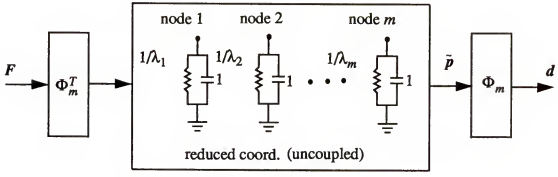

Figure 3.1 Configuration of the circuit network by the MS method.

3.2.2 Component Mode Synthesis

The semidiscrete heat equation for a substructure is rewritten in partition form as

$$\begin{bmatrix} \boldsymbol{m}^{bb} & \boldsymbol{m}^{bi} \\ \boldsymbol{m}^{ib} & \boldsymbol{m}^{ii} \end{bmatrix} \begin{bmatrix} \dot{\boldsymbol{d}}^{bd} \\ \dot{\boldsymbol{d}}^{int} \end{bmatrix} + \begin{bmatrix} \boldsymbol{k}^{bb} & \boldsymbol{k}^{bi} \\ \boldsymbol{k}^{ib} & \boldsymbol{k}^{ii} \end{bmatrix} \begin{bmatrix} \boldsymbol{d}^{bd} \\ \boldsymbol{d}^{int} \end{bmatrix} = \begin{bmatrix} \boldsymbol{F}^{bd} \\ \boldsymbol{F}^{int} \end{bmatrix} \tag{3.5}$$

where the superscript *bd* corresponds to the nodes at the interface boundary, and the superscript *int* to the nodes in the interior. Consider the eigenvalue problem

$$(\boldsymbol{k}^{ii} - \lambda_l \boldsymbol{m}^{ii})\phi_l = 0 \tag{3.6}$$

corresponding to the substructure with fixed interfaces (i.e., $\boldsymbol{d}^{bd} = 0$). The interior unknown $\boldsymbol{d}^{int}$ is approximated by a linear combination of the m dominant modes $\Phi = [\phi_1 \ \phi_2 \ \cdots \ \phi_m]$ as in the MS method and the constraint modes obtained from a static condensation as follows. Let $\boldsymbol{F}^{int} = 0$ for the moment; by statically condensing the interior unknown $\boldsymbol{d}^{int}$, we have $\boldsymbol{d}^{int} = -(\boldsymbol{k}^{ii})^{-1}\boldsymbol{k}^{ib}\boldsymbol{d}^{bd} \equiv \varphi \boldsymbol{d}^{bd}$, where φ is called the matrix of constraint modes. Let $\boldsymbol{p}^{bd}$ and $\boldsymbol{p}^{int}$ denote the new generalized coordinates (with reduced dimension), we can approximate $\boldsymbol{d}^{bd}$ and $\boldsymbol{d}^{int}$ by

$$\begin{bmatrix} \boldsymbol{d}^{bd} \\ \boldsymbol{d}^{int} \end{bmatrix} = \begin{bmatrix} \boldsymbol{I} & \boldsymbol{0} \\ \varphi & \Phi \end{bmatrix} \begin{bmatrix} \boldsymbol{p}^{bd} \\ \boldsymbol{p}^{int} \end{bmatrix} \equiv \Psi \begin{bmatrix} \boldsymbol{p}^{bd} \\ \boldsymbol{p}^{int} \end{bmatrix} \tag{3.7}$$

from which it can be seen that the interface coordinates $\boldsymbol{d}^{bd}$ remain unchanged ($\boldsymbol{d}^{bd} = \boldsymbol{p}^{bd}$), while the interior coordinates are significantly reduced (the size of $\boldsymbol{p}^{int}$ is small compared to that of $\boldsymbol{d}^{int}$). Applying the transformation matrix Ψ to the semidiscrete equation of the substructure, the reduced substructure model can be derived as

$$(\Psi^T \boldsymbol{M} \Psi)\dot{\boldsymbol{p}} + (\Psi^T \boldsymbol{K} \Psi)\boldsymbol{p} = \Psi^T \boldsymbol{F} \tag{3.8}$$

The reduced substructure thermal networks are obtained from the above equation and the simple rules discussed in Section 2.3.3. Note that the initial conditions in the new coordinate can be obtained from $\boldsymbol{p}^{bd}(0) = \boldsymbol{d}^{bd}(0)$ and $\boldsymbol{p}^{int}(0) = \Phi^{-1}[\boldsymbol{d}^{int}(0) - \varphi \boldsymbol{d}^{bd}(0)]$. For simplicity but without loss of generality, only two substructures (sub. a and sub. b) shown in Fig. 3.2 are considered. The coordinate transformation for the whole system (sub. a + sub. b) can be written as follows:

$$\begin{bmatrix} \boldsymbol{d}_a^{int} \\ \boldsymbol{d}^{bd} \\ \boldsymbol{d}_b^{int} \end{bmatrix} = \begin{bmatrix} \Phi_a & \varphi_a & \boldsymbol{0} \\ \boldsymbol{0} & \boldsymbol{I} & \boldsymbol{0} \\ \boldsymbol{0} & \varphi_b & \Phi_b \end{bmatrix} \begin{bmatrix} \boldsymbol{p}_a^{int} \\ \boldsymbol{p}^{bd} \\ \boldsymbol{p}_b^{int} \end{bmatrix} \equiv \Psi_{ab} \begin{bmatrix} \boldsymbol{p}_a^{int} \\ \boldsymbol{p}^{bd} \\ \boldsymbol{p}_b^{int} \end{bmatrix} \tag{3.9}$$

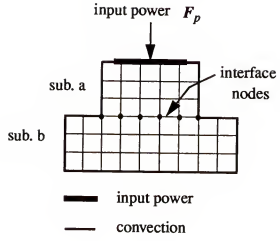

Figure 3.2 A thermal system divided into two substructures.

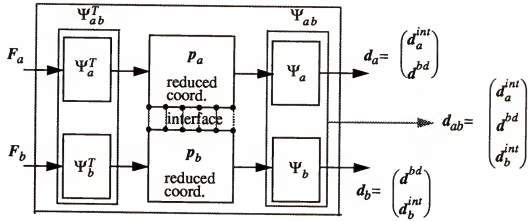

Figure 3.3 Configuration of the circuit network by the CMS method.

The circuit configuration implemented in SABER for these two substructures is shown in Fig. 3.3. Since the coordinates at the interface boundary nodes are kept unchanged, these two substructures can be connected directly at these nodes. The same methodology can be applied for a system with three or more substructures.

3.2.3 Model Error Estimation

When applying the MS and CMS methods, the lowest eigenvalues (poles) are usually chosen as the dominant eigenvalues (poles). However, this is not true in general since high-frequency eigenvalues may be important sometimes. A systematic way to determine dominant eigenvalues is presented in Yousuff and Breida [You93] for second-order systems. We apply the same methodology for the first-order thermal problems. The semi-discrete heat equation can be written as

$$\begin{aligned} \boldsymbol{M}\dot{\boldsymbol{d}} + \boldsymbol{K}\boldsymbol{d} &= \boldsymbol{F} = \boldsymbol{P}\boldsymbol{u} \\ \boldsymbol{y} &= \boldsymbol{Q}\boldsymbol{d} \end{aligned} \tag{3.10}$$

where the matrix $\boldsymbol{P}$ represents the distribution of input forces $\boldsymbol{u}$, and $\boldsymbol{Q}$ the outputs which are concerned. By the MS or CMS methods, (3.10) can be transformed into the state-space form:

$$\begin{aligned} \dot{\boldsymbol{x}} &= \boldsymbol{A}\boldsymbol{x} + \boldsymbol{B}\boldsymbol{u} \\ \boldsymbol{y} &= \boldsymbol{C}\boldsymbol{x} = \sum_{i \in N_n} c_i x_i \end{aligned} \tag{3.11}$$

where the dimension of $\boldsymbol{x}$ is still n-by-1, that is, all eigenvalues are retained and $N_n = \{1, 2, \ldots, n\} = N_{ret} \cup N_{tru}$. By retaining m eigenvalues $\in N_{ret}$, the reduced system can be written as

$$\begin{aligned} \dot{\boldsymbol{x}}_r &= \boldsymbol{A}_r \boldsymbol{x}_r + \boldsymbol{B}_r \boldsymbol{u} \\ \boldsymbol{y}_r &= \boldsymbol{C}_r \boldsymbol{x}_r = \sum_{i \in N_{ret}} c_i x_i \end{aligned} \tag{3.12}$$

The error (vector) between the full model and the reduced model can be defined as

$$\boldsymbol{e} = \boldsymbol{y} - \boldsymbol{y}_r = \sum_{i \in N_{tru}} c_i x_i \equiv \sum_{i \in N_{tru}} \Psi_i \tag{3.13}$$

i.e., the error is defined as the contribution due to the truncated modes. The model error is

defined as

$$\delta V = \lim_{t\to\infty} \varepsilon\left[\frac{1}{t}\int_0^t \boldsymbol{e}^T(\sigma)\boldsymbol{e}(\sigma)d\sigma\right] = \sum_{i\in N_{tru}}\sum_{j\in N_{tru}} \Psi_{ij} \tag{3.14}$$

where

$$\Psi_{ij} = \lim_{t\to\infty} \varepsilon\left[\frac{1}{t}\int_0^t \psi_i^T(\sigma)\psi_j(\sigma)d\sigma\right] = \lim_{t\to\infty} \varepsilon\left[\frac{1}{t}\int_0^t x_i^T(\sigma)c_i^T c_j x_j(\sigma)d\sigma\right]$$
$$= \mathrm{tr}(c_i^T c_j X_{ji}) = c_i^T c_j X_{ji} \tag{3.15}$$

where

$$X_{ij} = \lim_{t\to\infty} \varepsilon\left[\frac{1}{t}\int_0^t x_i(\sigma)x_j^T(\sigma)d\sigma\right] \tag{3.16}$$

and $\boldsymbol{X}$ satisfies the Lyapunov equation [Ske88]:

$$\boldsymbol{X}\boldsymbol{A}^T + \boldsymbol{A}\boldsymbol{X} + \boldsymbol{B}\boldsymbol{B}^T = 0 \tag{3.17}$$

For the MS method, $\boldsymbol{A} = -\Lambda_n = \mathrm{diag}[-\lambda_1\ -\lambda_2\ \cdots\ -\lambda_n]$, and we can obtain (refer (5.144) in [Ske88])

$$X_{ij} = \frac{b_i^T b_j}{\lambda_i + \lambda_j} \tag{3.18}$$

There are $n!/[m!(n-m)!]$ possible combinations of reduction sets, of which one will produce the smallest model error, (3.14). Since the computation is intensive, model error estimation is applied only when it is really necessary. Most of the time, it is good enough to choose the lowest eigenvalues as the dominant eigenvalues.

3.2.4 Ritz Vector Approach

Since the solutions of eigenvalue problems are computationally intensive, an efficient algorithm of generating the transformation matrix by Ritz vector approach is discussed here. Ritz vectors, derived from the spatial distribution of dynamic load, will

assure that important response modes are not neglected. It is shown in Wilson and Yuan [Wil82] that the superposition of Ritz vectors yields improved accuracy with fewer vectors as compared to the use of eigenvectors. By the Ritz vector approach, the CPU time is reduced and the number of Ritz vectors, needed for a given accuracy, can be determined a priori by an error estimation. Craig et al. [Cra88, Su89, Su91] presented another special set of Ritz vectors, called Block-Krylov vectors, for generating the transformation matrix. It is shown that the moment-matching property is implied in the Krylov vector approach. The main difference between the Ritz vector approach and the Krylov vector approach lies in the applied methods for orthogonalization. Gram-Schmidt procedure is used in the Ritz vector approach, while Lanczos algorithm is applied in the Krylov vector approach.

The procedures of generating orthogonal Ritz vectors and Krylov vectors for the system $\boldsymbol{M}\dot{\boldsymbol{d}} + \boldsymbol{K}\boldsymbol{d} = \boldsymbol{F}(t)$ $(= \boldsymbol{f}(s)\boldsymbol{r}(t) = \boldsymbol{P}(s)\boldsymbol{u}(t))$ are summarized below, where $\boldsymbol{f}(s)$ is an n-by-1 vector [Wil82] and $\boldsymbol{P}(s)$ is an n-by-m matrix [Su91], which account for the spatial load distributions, and are used for generating the Ritz vectors and the Block-Krylov vectors, respectively.

Algorithm for generating orthogonal Ritz vectors [Wil82]

1. Given mass, stiffness matrices $\boldsymbol{M}$, $\boldsymbol{K}$, and load vector $\boldsymbol{f}$

2. Triangularize stiffness matrix $\boldsymbol{K} = \boldsymbol{L}^T\boldsymbol{D}\boldsymbol{L}$

3. Solve for first vector, ϕ_1

$\boldsymbol{K}\phi_1^* = \boldsymbol{f}$ (Solve for ϕ_1^*)

$\phi_1^T\boldsymbol{M}\phi_1 = 1$ (Normalized and find ϕ_1)

4. Solve for additional vectors $i = 2, \ldots, l$

$\boldsymbol{K}\phi_i^* = \boldsymbol{M}\phi_{i-1}$ (Solve for ϕ_i^*)

$c_j = \phi_j^T\boldsymbol{M}\phi_i^*$ (Compute for $j = 1, \ldots, i-1$)

$$\phi_i^{**} = \phi_i^* - \sum_{j=1}^{i-1} c_j\phi_j \quad \text{(M-orthogonalized)}$$

$\phi_i^T M \phi_i = 1$ (M-normalized and find ϕ_i)

5. Orthogonalized Ritz vector with respect to stiffness matrix (optional)

Krylov/Lanczos algorithm [Su91]

1. Starting vectors

(a) $Q_0 = 0$

(b) $R_0 = K^{-1}P$

(c) $R_0^T K R_0 = U_0 \Sigma_0 U_0^T$ (singular-value decomposition)

(d) $Q_1 = R_0 U_0 \Sigma_0^{-1/2}$ (normalization)

2. For $j = 1, 2, \ldots, k-1$, repeat

(e) $\tilde{R}_j = K^{-1} M Q_j$

(f) $R_j = \tilde{R}_j - Q_j A_j - Q_{j-1} B_j$ (orthogonalization)

where $A_j = Q_j^T K \tilde{R}_j$ and $B_j = U_{j-1} \Sigma_{j-1}^{1/2}$

(g) $R_j^T K R_j = U_j \Sigma_j U_j^T$ (singular-value decomposition)

(h) $Q_{j+1} = R_j U_j \Sigma_j^{-1/2}$ (normalization)

3. Form the k-block projection matrix $\Phi = [Q_1 \; Q_2 \; \cdots \; Q_k]$

The derived reduced system is written as

$$(\Phi^T M \Phi)\dot{p} + (\Phi^T K \Phi) p = \Phi^T F \tag{3.19}$$

where $d = \Phi p$ and Φ is derived from the Ritz vector approach or the Krylov vector approach. The reduced thermal networks can be derived from (3.19) and the simple rules discussed in Section 2.3.3.

In thermal problems, we choose the load vector $f(s)$ as an n-by-1 vector, whose components are either 1 or 0 --- with 1 to account for the location of the input forces. This is similar to the assumption that all input forces have the same time-dependent function. Note that the goal of the Ritz vector approach is to generate a set of orthogonal basis vectors which are not orthogonal to the load vector, so that important modes are not neglected. Basically an arbitrary starting vector can be used so long as the generated basis vectors are not orthogonal to the load vector.

The number of Ritz vectors needed for a certain accuracy is determined by an error estimation [Wil82]. The vector $\boldsymbol{f}$ can be expressed by a finite series

$$\boldsymbol{f} = \sum_j q_j \boldsymbol{M}\phi_j \tag{3.20}$$

Multiplying ϕ_i^T on both sides of the equation, and applying the property of orthogonality, $\phi_i^T \boldsymbol{M}\phi_j = \delta_{ij}$, it can be shown that $q_i = \phi_i^T \boldsymbol{f}$. The error in the representation of the vector $\boldsymbol{f}$ by a finite number of vectors is given by

$$\boldsymbol{e} = \boldsymbol{f} - \sum_j q_j \boldsymbol{M}\phi_j \tag{3.21}$$

The error norm is defined as

$$e = \frac{\boldsymbol{f}^T \boldsymbol{e}}{\boldsymbol{f}^T \boldsymbol{f}} \tag{3.22}$$

which varies from $e = 1$, if no vectors are used, to $e = 0$, if all vectors are used. For a specified e, the number of Ritz vectors needed can be determined a priori, and the ratio $h_j = \boldsymbol{f}^T q_j \boldsymbol{M}\phi_j / \boldsymbol{f}^T \boldsymbol{f}$ indicates the contribution of each Ritz vector to the load expansion.

3.2.5 Implementation of the CMS Models

In the electro-thermal simulation [Hef93], the input power to the thermal system is supplied from one output node of the electro-thermal semiconductor model, and is

connected to one node of the thermal system only. By defining that nodal temperature as a system variable, the calculated nodal temperature is dynamically coupled to the semiconductor model. This kind of one-node connection is good for the 1-D case, however, for the 2-D or 3-D finite element approximations, the input power to the thermal system is imported from a line boundary or a surface boundary which include several nodes. In order to use the electro-thermal semiconductor model which has only one output power node, CCCSs (Current Controlled Current Sources) and a VCVS (Voltage Controlled Voltage Source), written in the equation section of the SABER template, are included in the reduced model of the Si chip. The configuration of the Si chip and package thermal models implemented in SABER are shown in Fig. 3.4, and the template structure of the Si chip is shown as follows:

```
#########################################################
element template si_chip tj b1 b2 ... bn
thermal_k tj, b1, b2, ..., bn
{
thermal_k tj1, tj2, a1, a2, ..., am
number p1 = x1, h1 = y1,
    p2 = x2, h2 = y2,
    ...
var i ip, ipp
equation{
p(tj -> tj1) += ip
ip: tk(tj) = tk(tj1)
p(tj1) += ipp
ipp: tk(tj1) = tk(tj2)  #(similar to VCVS)
p(tj2) -= p1*ip + h1  #(to model Ij, similar to CCCS)
p(a1) -= p2*ip + h2  #(to model Ia1, similar to CCCS)
...
    }
Netlist which describe the passive RC network derived
from the reduced mass and stiffness matrices
}
#########################################################
```

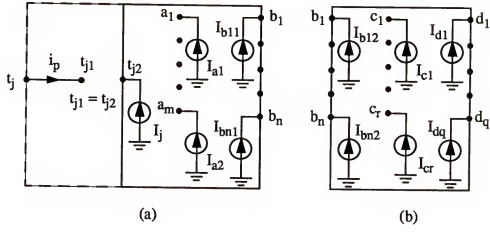

Figure 3.4 Configuration of the CMS models implemented in SABER for (a) Si chip; (b) thermal package.

In Figure 3.4, t_{j2} (= t_{j1} = t_j), b_i's, d_i's are the fixed interface nodes, and a_i's, c_i's are the nodes in the new coordinates. In the template structure, p_i's are the input power terms, h_i's are the convection terms, and x_i's, y_i's are constants calculated from the transformation matrix and the force vector. Note that only one node, t_{j2}, in the power input boundary is chosen as a fixed interface node in Fig. 3.4, and that nodal temperature is coupled back to the electrical system. In fact, more than one node in the power input boundary can be chosen as fixed interface nodes, and the average nodal temperature or a certain specified nodal temperature can be feedback to the electrical system. A similar approach is used for the implementation of the MS models.

3.3 Different Approaches

3.3.1 An Alternative Method

Based on the MS method, an alternative method for substructuring is discussed here. The original system shown in Fig. 3.2 is separated into two substructures as shown in Fig. 3.5(a), where $\boldsymbol{F}_B$ is an artificial force vector to account for the position of the

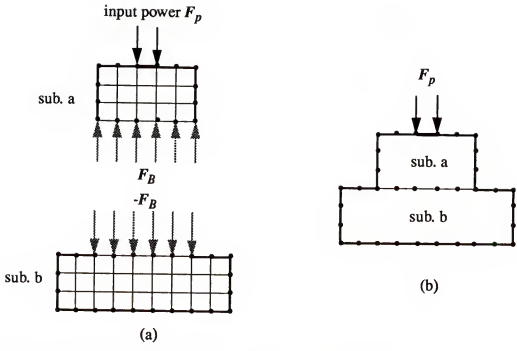

Figure 3.5 (a) An alternative method; (b) Assemblage of the reduced models of sub. a and sub. b.

interface nodes. There are two other types of input forces; one is due to the input power (F_p), and the other is due to the convection (F_v). The goal of this method is to retain all the boundary nodes in the original coordinate so that all the input power and convection can be applied directly to the reduced model without any transformation. From (3.4), a matrix W can be derived as follows:

$$\Phi_m^T F = \Phi_m^T (F_p^T \;\; F_v^T \;\; F_B^T \;\; 0^T)^T = W^T (F_p^T \;\; F_v^T \;\; F_B^T)^T \tag{3.23}$$

From $d \approx \Phi_m \tilde{p}$, we can also obtain $d_r \approx W \tilde{p}$, where d_r only retains the peripheral nodes. The reduced system for a substructure can be derived as follows:

$$[(W^T)^{-1} W^{-1}] \dot{d}_r + [(W^T)^{-1} \Lambda_m W^{-1}] d_r = (F_p^T \;\; F_v^T \;\; F_B^T)^T \tag{3.24}$$

The assemblage of the reduced substructure models is shown in Fig. 3.5(b). Note that some interior nodes can also be retained in the reduced substructure model. If the number of the peripheral nodes are very large, some convection nodes can be integrated into one common node A as shown in Fig. 3.6, where one dummy capacitor is added so that node A

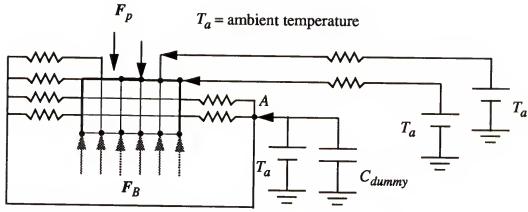

Figure 3.6 Integrating some convection nodes into a common node A (dotted nodes are retained).

will contribute to a state variable that prevents the singularity of the mass matrix $\boldsymbol{M}$. This dummy capacitor should be small enough so that only a pole at very high frequency is introduced and will be discarded in the model reduction process. It is flexible to have several common nodes and retain some interior nodes at the same time. The advantage of this method is that it works in the original coordinates and no transformation matrices for the inputs and outputs are needed. The disadvantage of this method is that the $\boldsymbol{W}$ matrix may be ill-conditioned. However, by carefully choosing the retained nodes and the common nodes, this problem may be avoided.

3.3.2 Boundary Element Method

The idea behind the FEM is to discretize the interior of the computational domain, while forcing the trial function to satisfy the boundary conditions a priori. The idea behind the BEM is to discretize the boundary, while forcing the trial function to satisfy the interior problem through the use of fundamental solutions. BEM is investigated because the dimension of the formulated matrices is smaller than that of the formulated matrices by FEM or FDM for the same accuracy, however, the formulated matrices by BEM are normally full and nonsymmetric. BEM is currently used for solving steady state solutions of the thermal system in this work.

Let us consider the Laplace's equation $\nabla^2 u = 0$ on a domain Ω, subject to the boundary conditions of the thermal problems (i.e., convection and input power). Multiplying the equation by a weighting function G and integrating over the domain Ω, then applying the divergence theorem, we can obtain Green's second identity,

$$\int_{\Omega} G\nabla^2 u d\Omega = \int_{\Omega} u\nabla^2 G d\Omega + \oint_{\Gamma}\left(G\frac{\partial u}{\partial n} - u\frac{\partial G}{\partial n}\right)d\Gamma = 0 \tag{3.25}$$

where $\Gamma = \partial\Omega$. By choosing G such that

$$\nabla^2 G + \Delta_i = 0 \tag{3.26}$$

where Δ_i is the Dirac delta function, we can obtain

$$-u_i + \oint_{\Gamma}\left(G\frac{\partial u}{\partial n} - u\frac{\partial G}{\partial n}\right)d\Gamma = 0 \tag{3.27}$$

Approximating the boundary Γ by the discretized boundary elements yields

$$u_i + \sum_{j=1}^{n} u_j \int_{\Gamma_j} \frac{\partial G_i}{\partial n} d\Gamma_j = \sum_{j=1}^{n} \frac{\partial u_j}{\partial n} \int_{\Gamma_j} G_i d\Gamma_j \tag{3.28}$$

Replacing $\frac{\partial u_j}{\partial n}$ by q_j, and $\frac{\partial G_i}{\partial n}$ by q_i^* yields

$$u_i + \sum_{j=1}^{n} u_j \int_{\Gamma_j} q_i^* d\Gamma_j = \sum_{j=1}^{n} q_j \int_{\Gamma_j} G_i d\Gamma_j \tag{3.29}$$

Equation (3.29) can be rewritten as

$$\sum_{j=1}^{n} H_{ij} u_j = \sum_{j=1}^{n} J_{ij} q_j, \; i = 1, \ldots, n \tag{3.30}$$

or in a matrix form

$$\boldsymbol{Hu} = \boldsymbol{Jq} \tag{3.31}$$

where

$$H_{ij} = \int_{\Gamma_j} q_i^* d\Gamma_j \text{ when } i \neq j, \tag{3.32}$$

$$H_{ii} = 1 + \int_{\Gamma_i} q_i^* d\Gamma_i \text{ when } i = j \tag{3.33}$$

$$J_{ij} = \int_{\Gamma_j} G_i d\Gamma_j \tag{3.34}$$

Replacing q_j by the boundary condition in the thermal problem, i.e., $q_j = \frac{P}{\kappa A}$ for the boundary of input power, and $q_j = \frac{h}{\kappa}(T_a - u_j)$ for the boundary of convection, we can obtain a simple matrix equation

$$\boldsymbol{Ku} = \boldsymbol{F} \tag{3.35}$$

where $\boldsymbol{K}$ and $\boldsymbol{F}$ are obtained from $\boldsymbol{H}$, $\boldsymbol{J}$, and $\boldsymbol{q}$.

As mentioned earlier, G is the solution of (3.26). For the two-dimensional problems, the potential G is a function of radius and (3.26) reduces to

$$\frac{1}{r}\frac{d}{dr}\left(r\frac{dG}{dr}\right) + \frac{se^{-sr^2}}{\pi} = 0 \tag{3.36}$$

where the Dirac delta function Δ_i has been expressed as a delta sequence. Equation (3.36) can be integrated twice to yield

$$G = \frac{1}{2\pi}\ln\left(\frac{1}{r}\right) \tag{3.37}$$

since s approaches infinity. For the three-dimensional problems, the potential G can be derived as

$$G = \frac{1}{4\pi r} \tag{3.38}$$

It is stated [Kuw87] that the numerical integration in the BEM not only expends much CPU-time but also produces a large error because the weighting function (G) has a singularity. Therefore, it is desirable that we use the analytical integration as much as possible. The analytical integration formulas for constant boundary elements and linear boundary elements [Huy83] are used in this work. The analytical integration formulas for higher-order boundary elements can be found in Kuwahara and Takeda [Kuw87].

For a constant boundary element, the function u and $\frac{\partial u}{\partial n}$ are assumed to be constant on each element and equal to the value at the midside node of the element. Figure 3.7 shows a local coordinate ($l-n$) system for a constant boundary element j. The analytical integration formulas are listed below [Huy83]:

$$H_{ij} = \beta_{ij} \text{ for } i \neq j \tag{3.39}$$

$$H_{ii} = -\pi \text{ for } i = j \tag{3.40}$$

$$J_{ij} = [-l_2 \ln(r_{i2}) + l_1 \ln(r_{i1}) + L_j - p_j \beta_{ij}] \text{ for } i \neq j \tag{3.41}$$

$$J_{ii} = L_i \left[\ln\left(\frac{2}{L_i}\right) + 1 \right] \text{ for } i = j \tag{3.42}$$

The integration formula for a linear boundary element can be found in Huyakorn and

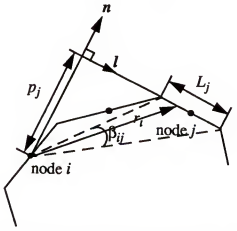

Figure 3.7 Local coordinate system for the constant boundary element j.

Pinder [Huy83], and the solutions of the interior nodes are calculated as follows:

$$u_i = \frac{1}{2}\left[\sum_{j=1}^{n} J_{ij} q_j - \sum_{j=1}^{n} H_{ij} u_j\right] \tag{3.43}$$

Thus, when u and $\frac{\partial u}{\partial n}$ at the boundary nodes are evaluated, the solution at any interior node can be calculated from (3.43).

In order to build the BEM-based equivalent thermal network for the steady-state thermal problems, the nonsymmetric stiffness matrix $\boldsymbol{K}$ in (3.35) is decomposed into a symmetric matrix, which is realized by a resistor network, and a nonsymmetric matrix, which is realized by some VCCSs (Voltage Controlled Current Sources). The steady-state solution of the thermal system by BEM has been obtained and verified by the FEM steady-state solution, and an excellent agreement of both solutions is observed. Note that a combination of Kirchhoff transformation and BEM may be a good approach for solving nonlinear steady-state thermal problems. BEM for a nonlinear transient thermal problem is discussed in Kikuta et al. [Kik87], however, it is not easy to build a transient thermal circuit model based on BEM since time integrations appear in the elements of the formulated matrices and some time-derivative terms exist inside the time integrations.

3.4 Verification and Application

3.4.1 Verification of Reduced Thermal Models

A FEM code is written in Matlab to test the model reduction techniques, and programs (/thesis_programs/saber_si.m, saber_package.m, saber_sink.m) are written to automatically generate the SABER templates for the Si chips, packages, and heat sinks. The thermal system shown in Fig. 3.2 with 439 mesh nodes is used as an example to demonstrate the MS and CMS methods discussed previously. The properties for sub. a are: thermal conductivity κ_a = 1.5486W/(cm-K), mass density ρ_a = 2.33 g/cm^3, specific heat c_{pa} = 0.7 J/g-K, thickness = 0.03cm, and width = 0.5cm; and those for sub. b are: κ_b = 4 W/cm-K, ρ_b = 8.9 g/cm^3, c_{pb} = 0.39 J/g-K, thickness = 0.03cm, and width =

0.9cm. Convection coefficient h = 0.01 W/cm$^2 - K$, power input cross-section area A = 0.1 cm^2, power input P = 150W, and ambient temperature T_a = 300 K (initial condition). The external boundary conditions include both the power input boundary and the convection boundary, while the conduction boundary condition at the interface is implicitly satisfied in formulating the system equations. Figure 3.8 shows the results by the MS method with Ritz vector approach. It is surprising that only three Ritz vectors give very accurate result compared to the full system response with 439 poles. To simulate 0.05 second in Matlab with a fixed time-step (0.0001 second), it takes 3.666139x10^6 flops for the system equations with 3 poles (MS method), and 5.55940943x10^8 flops for the system equations with 439 poles (full system response); thus, the simulation speed is about 150 times faster under the same simulation conditions. Figure 3.9 shows the results by the CMS method with eigenvector approach. Figure 3.10 shows the results by the CMS methods with Ritz vector approach. In Figs. 3.9 and 3.10, the number of constraint modes denotes the number of boundary nodes in the interface of sub. a and sub. b, and the numbers of normal modes in sub. a and sub. b denote the numbers of dominant eigenvalues retained in the normal matrices Φ_a and Φ_b. Results by the alternative method with eigenvector approach is shown in Fig. 3.11. The number of retained modes are indicated in the figures. The automatically generated substructure templates for Si chip and TO247 are tested for the 2-D problem shown in Fig. 2.22, and the simulation result is shown in Fig. 3.12. Based on the simulation results, Ritz vector approach is good for the MS method, however, it seems that the CMS method with Ritz vector approach gives less accurate results compared to the CMS method with eigenvector approach for the same number of retained nodes.

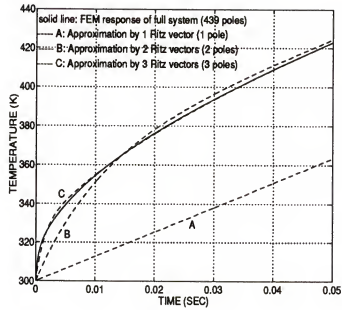

Figure 3.8 Results by the MS method with Ritz vector approach.

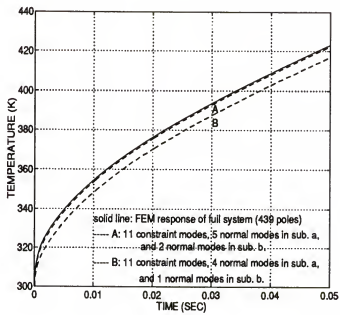

Figure 3.9 Results by the CMS method with eigenvector approach.

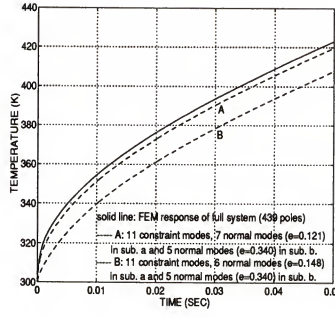

Figure 3.10 Results by the CMS method with Ritz vector approach.

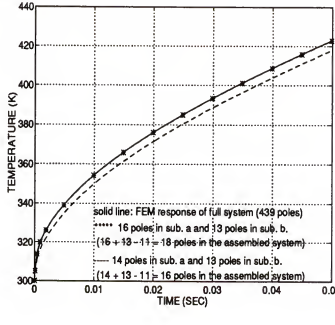

Figure 3.11 Results by the alternative method with eigenvector approach.

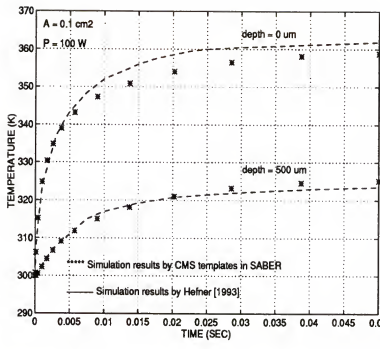

Figure 3.12 Verification of the CMS templates in SABER.

3.4.2 Electro-Thermal Simulation

The generated SABER templates of the Si chips, packages, and heat sinks are applied for the electro-thermal simulation of power electronic circuits and devices. When performing electro-thermal simulations in the SABER circuit simulator, the Si-junction temperatures, T_j's, are treated as system variables so that the electrical system and the thermal system are dynamically coupled.

A particular electro-thermal system, a full-bridge converter with four IGBT devices, shown in Fig. 3.13, is simulated in SABER; the parameters used are: V_{in} = 100 V_{DC}, primary to secondary turn ratio $n_1/n_2 = 2$, gate resistances R_{gi} = 100Ω, inductance L = 300 μH, capacitance $C_{in} = C_o$ = 100 μF, and output resistance R_o = 5Ω. These values are chosen so that thermal run-away occurs; thermal run-away can not be predicted from a conventional circuit simulation with a fixed temperature. The electro-thermal IGBT model presented in [Hef93] is used in the

simulation, and the parameters in the IGBT model are *taul* = 7.1u, *tauhltexp* = 1.5, *wb* = 10m, *nb* = 2.0e14, *a* = 0.1, *agd* = 0.05, *isne* = 10f, *isnetexp* = 0.5, *vt* = 5.0, *vttco* = -0.009, *rs* = 0.01, *theta* = 0.01, *thetatexp* = 0, *kf* = 2.0, *kftexp* = 0, *kp* = 0.25, *kptexp* = 1.5, *cgs* = 1n, *coxd* = 2n, *vtd* = 0, *vtdtco* = 0, *bvf* = 1.0, *bvftexp* = 0.35, *bvn* = 4.0, *bvntexp* = 0, *tnom* = 27, *alpha* = 2.54, and *gmin* = 1p. The short-circuit-test simulation result of the IGBT model with the above parameters is similar to that published in Hefner and Blackburn [Hef93]. The waveform of the driving voltages, with T_{on} = 15us, Δ = 10us, and T_s = 50us, are shown in Fig. 3.14, where Δ denotes the dead-time period when all switches are off. Simulation results of V_o, I_o, and the Si-junction temperature T_{j1} at V_{gk} = 20V and 7V for the first 10ms are compared in Fig. 3.15 and Fig. 3.16, respectively. Simulated output voltage without thermal effects at V_{gk} = 20V is also shown in Fig. 3.15 for comparison. Theoretically, the steady-state output voltage is given by

$$V_o = 2\left(\frac{n_2}{n_1}\right)DV_{in} \text{ with } D = \frac{T_{on}}{T_s} \tag{3.44}$$

which is verified in the case of V_{gk} = 20V. For the driving circuit with V_{gk} = 7V, it is insufficient to drive the IGBT devices, and the output voltage and current are below the designed values. The IGBT on-voltage V_{ak} at V_{gk} = 7V is higher than that at V_{gk} = 20V, but the on-current I_{ak} at V_{gk} = 7V is smaller than that at V_{gk} = 20V; thus, it is possible that the power loss at V_{gk} = 7V is smaller than that at V_{gk} = 20V, as found in the present simulation results using the IGBT model [Hef93]. The smaller power loss results in a smaller temperature rise.

Since the IGBT model [Hef93] is very nonlinear and requires several iterations to converge at each time step, and since the time constant of the thermal system is larger than that of the electrical system, the computation takes long simulation time and huge disk space for the temperature to go steady. Note that the reduced thermal models only take short simulation time and small disk space for the temperatures to converge to steady states. To avoid the difficulty found in the long-time electro-thermal simulation, two

iterative processes are applied to obtain the steady-state temperatures and the average power losses of the IGBT devices. The first iterative process is summarized as follows: (1) an electrical simulation of the full-bridge converter with fixed Si-junction temperatures (300K for the first iteration) is performed over a certain time (5ms in this example), and the average power loss of each device is determined during a chosen time interval (3ms to 5ms in this example) where the electrical power losses are steady; (2) a DC simulation of each thermal system with the determined average power loss is performed to estimate the steady-state temperatures; (3) the steady-state Si-junction temperatures are used for another electrical simulation to determine the average power loss of each device. The process is repeated until the temperatures and the average power losses converge to steady states. Note that WaveCalc^{TM} waveform calculator inside the SABER circuit simulator is used to calculate the average power losses by integrating the simulated power losses of different IGBT devices over the simulation time. The first iterative process converges after seven iterations. The integrated power losses of IGBT1 for the seven iterations are shown in Fig. 3.17. The converged average power losses are about 67W for the IGBT devices, and the converged steady-state Si-junction temperatures are about 476K. However, if only the electrical simulation at 300K is performed, the estimated average power losses are only 30.5W for IGBT1 and IGBT4, and 29W for IGBT2 and IGBT3.

The second iterative process discussed in Mantooth and Hefner [Man93] is also used to estimate the steady-state temperatures and the average power losses of the IGBT devices. The second iterative process is summarized as follows: (1) a full electro-thermal simulation (instead of the electrical simulation itself in the previous method) is performed over a certain time (5ms), and the average power loss of each device is determined during a chosen time interval (3ms to 5ms); (2) a DC simulation of each thermal system with the determined average power loss is then performed to estimate the steady-state temperatures; (3) the steady-state temperatures are used as initial conditions for another full electro-thermal simulation to determine the average power loss of each device. The process is again repeated until the temperatures and the average power losses converge to

steady states. The second iterative process converges after four iterations. The integrated power losses of IGBT1 for the four iterations are shown in Fig. 3.18. The converged average power losses after the fourth iteration are 64.5W for IGBT1 and IGBT4, and 57.5W for IGBT2 and IGBT3; the converged steady-state Si-junction temperatures are 471K for IGBT1 and IGBT4, and 455K for IGBT2 and IGBT3. Note that the average power losses after the first iteration are only 34.5W for IGBT1 and IGBT4, and 28W for IGBT2 and IGBT3.

The above example clearly shows that an electro-thermal simulation is essential for an accurate simulation of a power electronic system. Due to the self-heating effects, the steady-state average power losses of the IGBT devices are almost twice of those at the beginning of the transient. Moreover, thermal systems including Si chips, packages, and heat sinks determine the steady-state Si-junction temperatures of the IGBT devices, and thus determine the level of the average power losses.

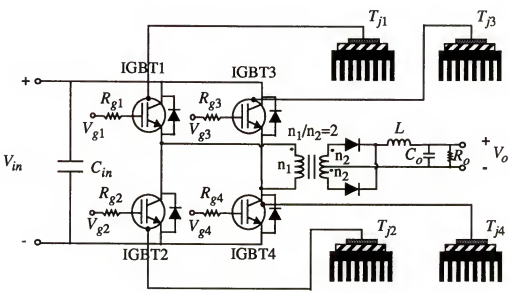

Figure 3.13 A particular electro-thermal system: a full-bridge converter with four IGBT's as switching devices.

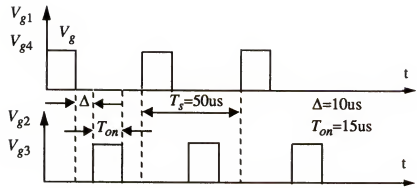

Figure 3.14 Waveforms of the driving voltages for the full-bridge converter.

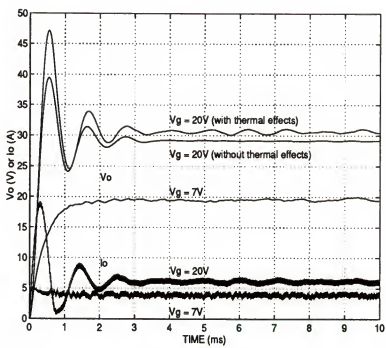

Figure 3.15 Comparison of output voltages and currents at different driving voltages.

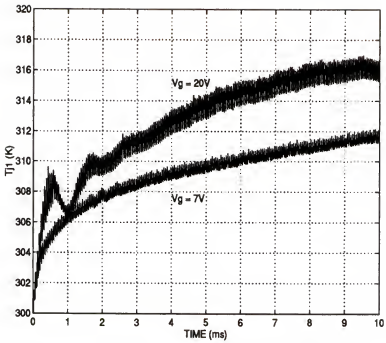

Figure 3.16 Comparison of Si-junction temperatures of IGBT1 at different driving voltages.

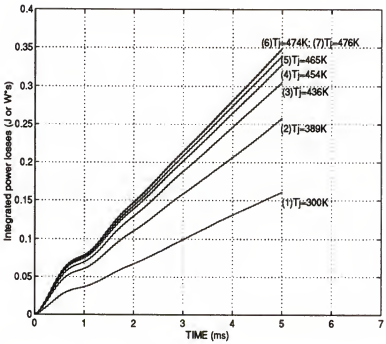

Figure 3.17 The integrated power losses versus time at different iterations for the first iterative process.

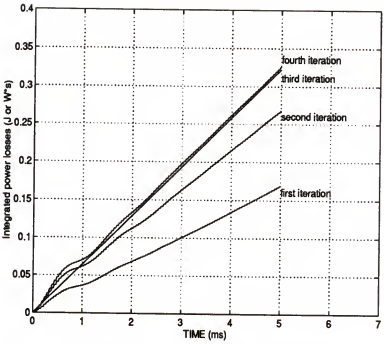

Figure 3.18 The integrated power losses versus time at different iterations for the second iterative process.

3.5 Summary

We have discussed model reduction techniques to obtain reduced thermal models of Si chips, packages, and heat sinks for an efficient electro-thermal simulation of power electronic circuits and devices. A future direction for modeling thermal systems for electro-thermal simulations is to develop reduced nonlinear models for nonlinear thermal systems, i.e., model reduction for nonlinear systems.

CHAPTER 4
BEHAVIORAL MODELING OF POWER SEMICONDUCTOR DEVICES FOR EFFICIENT CIRCUIT SIMULATION

4.1 Insulated Gate Bipolar Transistor (IGBT)

4.1.1 Introduction

Both physics-based and behavioral models [Hef91, Fos88, Kuo86, Fat93, She93, Kim93, Mih92, Tzo93] have been developed in recent years for the IGBT. Behavioral models are preferred when simulation speed and the flexibility of model synthesis are of concern [She93], but are less accurate than physics-based models over wide ranges of operating/application conditions.

This chapter presents a behavioral IGBT model which is constructed using the configuration of the Hammerstein model [Nar66, Bil79, Gre89, Fal91, Bil80, Gal75, Esk91, Krz93], and which captures several unique IGBT characteristics [Hef91]. Although it is doubtful that a behavioral model could replace a physics-based model, the behavioral model presented herein agrees well with the physics-based model [Hef91] in a variety of known operating/application conditions.

As shown in Fig. 4.1, a Hammerstein model consists of a nonlinear static block followed by a linear dynamic block. The Hammerstein model represents a realization of the Hammerstein operator,

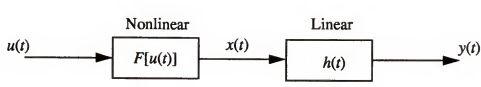

Figure 4.1 Configuration of the Hammerstein model.

$$H[u(t)] = \int_0^t h(t, \tau)F[\tau, u(\tau)]d\tau \tag{4.1}$$

which in the time-invariant case (abusing notation slightly) is simplified [Nar66] to

$$H[u(t)] = \int_0^t h(t-\tau)F[u(\tau)]d\tau \tag{4.2}$$

Normally, the intermediate signal $x(t)$ is unknown in the system identification process. However, it is recognized in this work that the nonlinear static block can be simply realized by the static (DC) model for a semiconductor device. This recognition tremendously simplifies the task of parameter extractions, for the static model can be directly obtained from the static current/voltage (I-V) characteristics using least-squares methods. Thus, conventional system identification procedures based on the random-signal tests for the SISO (Single-Input Single-Output) Hammerstein models [Nar66, Bil79, Gre89, Fal91, Bil80, Gal75, Esk91] or MISO (Multi-Input Single-Output) Hammerstein models [Esk91, Krz93] are not used in this work, although they may be applied for parameter extractions.

Unlike the linear dynamic block in a true Hammerstein model, the dynamic block employed herein is piecewise linear, and is realized by an RC low-pass filter which has different time constants which are related to the transients. In fact, the piecewise model structure of the behavioral model is equivalent to several parallel Hammerstein branches [Fal91]. In the literature, this kind of model is also called the Uryson model [Bil80, Gal75].

Initially, the behavioral model was built mathematically to capture the unique characteristics of the IGBT. After determining the model structure, it was found that the behavioral model actually captured some physical meanings, e.g., the non-quasi-static effect of the IGBT [Hef91]. The non-quasi-static effect is effectively accounted for by a Hammerstein-like model or by a series RC component [Wu93] in an alternative behavioral model.

The behavioral model of the IGBT will be described in Section 4.1.2. Extractions of the behavioral model parameters are discussed in Section 4.1.3. The accuracy and efficiency of the complete behavioral model are evaluated in Section 4.1.4.

4.1.2 Model Description

The IGBT device is treated as a "black box" with three external nodes, and a model structure is assumed to model the IGBT device. Fig. 4.2(a) shows the cross section of a vertical IGBT structure. The main model structure of the proposed behavioral model is shown in Fig. 4.2(b). Fig. 4.2(c) shows the model of the anode current I_a, which consists of two voltage-controlled current sources which are Hammerstein-like. An alternative behavioral model of the IGBT is also shown in Fig. 4.3. It is possible that more accurate results can be achieved by using a more sophisticated model structure.

4.1.2.1 DC (Static) model

It has been found that the dc anode current, $I_{dc} = f(V_{ak}, V_{gk})$, of the IGBT [Hef91] may be modeled behaviorally by the following piecewise functions:

$$
\begin{aligned}
I_{dc} &= 0 \quad \text{for } V_{gk} \le V_t \text{ or } V_{ak} < V_d \\
I_{dc} &= A_1(V_{gk}) \cdot \tanh\{A_2(V_{gk}) \cdot [V_{ak} - V_d]\} \\
&\qquad \text{for } V_d \le V_{ak} < V_b \text{ and } V_{gk} > V_t \\
I_{dc} &= I_b + A_3(V_{gk}) \cdot [V_{ak} - V_b] \\
&\qquad \text{for } V_{ak} \ge V_b \text{ and } V_{gk} > V_t
\end{aligned}
\tag{4.3}
$$

where

$$A_1(V_{gk}) = B_1 V_{gk} + B_2 V_{gk}^2 + B_3 V_{gk}^3 \tag{4.4}$$

$$A_2(V_{gk}) = \frac{B_4}{[1 + B_5(V_{gk} - V_t)]} \tag{4.5}$$

$$A_3(V_{gk}) = B_6 + B_7 V_{gk} \tag{4.6}$$

$$V_b \approx V_{gk} - V_t + V_d \tag{4.7}$$

$$I_b = A_1(V_{gk}) \cdot \tanh\{A_2(V_{gk}) \cdot [V_b - V_d]\} \tag{4.8}$$

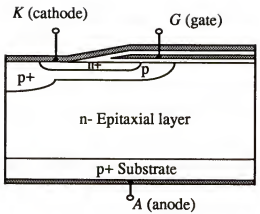

(a)

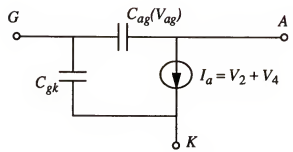

(b)

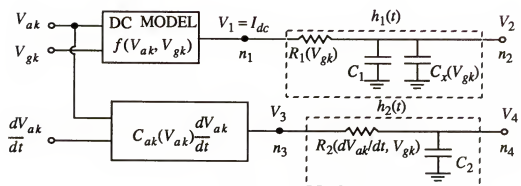

(c)

Figure 4.2 Cross section of a vertical IGBT (a); main structure of the behavioral model (b); and Hammerstein-like structures for I_a (c).

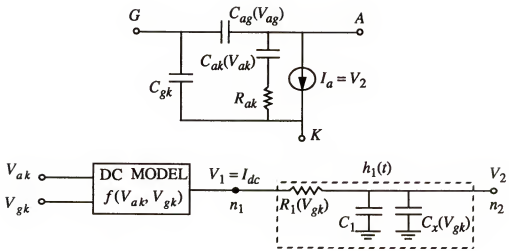

Figure 4.3 An alternative behavioral model of the IGBT.

V_t is the MOSFET channel threshold voltage; V_d the approximated turn-on voltage of the p^+(substrate)/n^-(epilayer) junction; V_b the approximated threshold voltage between the triode region and the saturation region; and the parameters not defined above are to be extracted by a procedure described later.

4.1.2.2 Dynamic model

In order to model the strong nonlinearities found in the IGBT transient waveforms, nonlinear elements are used in the dynamic blocks in Fig. 4.2. This is a significant departure from the standard Hammerstein model, which uses only linear elements in the dynamic blocks.

The capacitance between nodes A and G is modeled by a voltage-dependent capacitor C_{ag},

$$C_{ag} = \begin{cases} C_{ag0} & \text{for } V_{ag} \le V_{de} \\ \dfrac{C_{ag0} \cdot C_{agj}}{C_{ag0} + C_{agj}} & \text{for } V_{ag} > V_{de} \end{cases} \tag{4.9}$$

where

$$C_{agj} \approx s_1 \cdot A_{gd} \sqrt{\frac{\varepsilon_{si} q N_b}{2|V_{ag}|}} = \frac{s_{ag}}{\sqrt{|V_{ag}|}} \tag{4.10}$$

V_{de} is assumed constant for simplicity to account for the voltage drops at the p^+/n^- junction and in the n^- epilayer. C_{ag0} is a constant, and is slightly larger than the gate-drain overlap oxide capacitance C_{ox} [Hef91]. The model of C_{agj} in (4.10) is suggested from the analytical equation of the gate-drain depletion capacitance [Hef91], and s_{ag} is a scaling parameter to be extracted.

In this work, a constant C_{gk} is used to be consistent with the model in Hefner and Diebolt [Hef91] which is used for comparison. The accuracy may be improved, especially for $V_{gk} < 0$, if both C_{gk} and C_{ag} are approximated by piecewise linear capacitances as in Shen and Chow [She93], or by the more accurate models [Ong91, Sco90].

The h_1 block in Fig. 4.2(c) is used to model the dynamics of the anode current when $dV_{ak}/dt = 0$, e.g., during the constant anode voltage switching transient [Hef88]. For a constant C_1, R_1 and C_x are modeled as follows to capture the rapid decay of the anode current at the beginning of the turn-off transients in the constant anode voltage switching test:

$$R_1 = \begin{cases} R_{1on} & \text{for } V_{gk} > V_t \\ R_{1off} & \text{for } V_{gk} \le V_t \end{cases} \tag{4.11}$$

$$C_x = \begin{cases} 0 & \text{for } V_{gk} > V_t \\ \left(\dfrac{1-\alpha}{\alpha}\right) C_1 & \text{for } V_{gk} \le V_t \end{cases} \tag{4.12}$$

where α accounts for the ratio of the anode currents after and before the rapid decay. Note that the rapid fall time is assumed zero in the model. In order to model a finite fall time, a small resistor can be placed between C_1 and C_x. The effect of C_x on the turn-on transient is negligible since the anode current before turn-on is almost zero.

The nonlinear, capacitive dynamics between nodes A and K are modeled by V_4, which is a function of dV_{ak}/dt (and V_{ak}). In particular,

$$C_{ak} = \begin{cases} C_{akon} = s_{akon}/\sqrt{V_{ak}} & \text{for the turn-on transient} \\ C_{akoff} = s_{akoff}/\sqrt{V_{ak}} & \text{for the turn-off transient} \end{cases} \tag{4.13}$$

where C_{akon} is much less than C_{akoff} since the excess carrier charge is zero in the off-state before the initiation of the turn-on [Hef91]. Both C_{akon} and C_{akoff} can be modeled by functions of V_{ak}, or can be modeled as constants for simplicity. Note that the second Hammerstein-like model of I_a, i.e., the V_4 block, effectively accounts for the redistribution current resulting from the non-quasi-static behavior [Hef88]. The excess carrier charge is a function of time, and so is the redistribution current. The first-order RC filter in the h_2 block is used to model the time-dependent effects. For a constant C_2, R_2 is modeled as

$$R_2 = \begin{cases} R_{2on} & \text{for the turn-on transient} \\ R_{2off} & \text{for the turn-off transient} \end{cases} \tag{4.14}$$

Referring to (25)-(31) in Hefner and Blackburn [Hef88], the dependence of C_{ak} (the denominator of (31) [Hef88]) on V_{ak} is mostly due to the base-collector junction depletion width W_{bcj}, and can be simply approximated by (4.13). In this work, the turn-off transient is modeled as ($dV_{ak}/dt > 0$) or ($dV_{ak}/dt < 0$ and $V_{gk} \le V_t$), and the turn-on transient is modeled as $dV_{ak}/dt < 0$ and $V_{gk} > V_t$.

In the alternative behavioral model, a series R_{ak}-C_{ak} component is used to replace the V_4 block to account for the non-quasi-static time delay [Wu93]. The assumption of the quasi-static approximation is that carriers injected across a junction proceed with infinite velocity during transient so that there is no time delay in the anode current waveform. To correct this inaccuracy, a resistor R_{ak} is added in series with C_{ak} to represent the non-quasi-static time delay.

4.1.3 Parameter Extractions

The DC model parameters, B_i's, are directly extracted from the static I-V curves by least-squares methods. A two-step procedure is used. At each V_{gk}, three constants, A_1, A_2, and A_3, are extracted from the corresponding static I-V curve (I_a versus V_{ak}) using least-squares methods and (4.3), then B_i's are extracted by fitting $A_1(V_{gk})$, $A_2(V_{gk})$, and $A_3(V_{gk})$ according to (4.4) - (4.6). Note that $A_3(V_{gk})$ can be fit more accurately by a piecewise linear function. A linear least-squares method for polynomial fitting and the Levenberg-Marquardt method [Pre92] for nonlinear functional fitting are discussed in Appendix. Transient model parameters are extracted from the electrical measurements of physical devices (some test circuits and measurement data for the capacitance parameters can be obtained from the data books), or from the circuit simulations of physics-based models. If a physics-based model is used for parameter extractions, ramp functions can be effectively applied to extract the capacitance parameters. However, this approach is not suitable for direct electrical measurements of physical devices since the output signals may be too small to be accurately measured.

4.1.3.1 Extraction of R_1 and C_x in the h_1 block

In the behavioral model, the h_1 block is used to model the dynamics of the anode current when $dV_{ak}/dt = 0$. The parameters R_{1on}, R_{1off}, and α in (4.11) and (4.12) are extracted from the test circuit shown in Fig. 4.4(a), where the anode voltage is constant. The transient waveform of the anode current is shown in Fig. 4.4(b), where the rising and falling curves are fit by the following functions:

$$f_1(t) = I_0(1 - e^{-t/T_{on}}) \tag{4.15}$$

$$f_2(t) = I_1 e^{-t/T_{off}} \tag{4.16}$$

where $T_{on} = R_{1on}C_1$, $T_{off} = R_{1off}(C_1+C_x) = R_{1off}C_1/\alpha$, and $\alpha = I_1/I_0$. The parameters I_1 and I_0 can be obtained from the measured or simulated anode current waveform as shown in Fig. 4.4(b), and T_{on} and T_{off} can be determined by the Levenberg-Marquardt method.

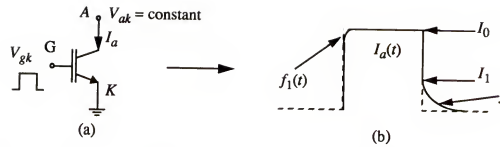

Figure 4.4 A test circuit for extracting R_1 and C_x in the $h_1(t)$ block (a); and the transient anode current waveform when anode voltage is constant (b).

Choosing C_1 = constant, R_{1on}, R_{1off}, and α can be easily determined, and C_x effectively accounts for the rapid decay of the anode current at the beginning of the turn-off transients.

4.1.3.2 Extraction of C_{gk}, C_{ag}, and parameters in the V_4 block

From the data books, three capacitance curves can be obtained:

$$C_{ies} = C_{gk} + C_{ag},\ C_{res} = C_{ag},\ C_{oes} = C_{ak} + C_{ag} \tag{4.17}$$

where C_{ies} is the input capacitance, C_{res} the reverse transfer capacitance, and C_{oes} the output capacitance. C_{ak} in (4.17) is equal to C_{akon} in (4.13). The measurement data of C_{gk}, C_{ag}, and C_{akon} can be directly fit by polynomial functions or by some assumed nonlinear functions, e.g., (4.9) and (4.10).

It is shown here that in the case of using a physics-based model for parameter extractions, ramp functions (which are simulated using part of triangular waveforms in circuit simulators) can be effectively applied to extract C_{gk} and C_{ag}. In the normal mode of operation, C_{gk} can be treated as a constant [Hef91], and this constant capacitance can be extracted from the simulated circuit shown in Fig. 4.5. From the simulated I_{g1} waveform, which is almost constant, $C_{gk} \approx I_{g1}/(dV_{gk}/dt)$ can be extracted.

After extracting C_{gk}, C_{ag0} in the C_{ag} model can be extracted from the simulated circuit shown in Fig. 4.6. From the simulated I_{g2} waveform, $C_{gk} + C_{ag0}$ can be extracted, which gives C_{ag0}. The scaling parameter s_{ag} in the C_{ag} model can also be extracted from

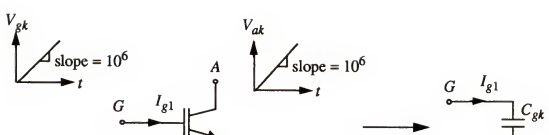

Figure 4.5 A simulated circuit for extracting C_{gk} from a physics-based model.

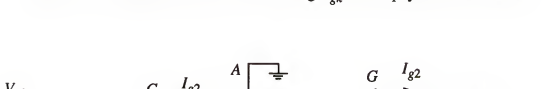

Figure 4.6 A simulated circuit for extracting C_{ag0} from a physics-based model.

Fig. 4.6, but with a constant positive anode voltage (e.g., V_{ak} = 300V) so that C_{ag} consists of both C_{ag0} and C_{agj} components. From (4.9), (4.10), and

$$I_{ga} = \frac{d}{dt}(C_{ag}V_{ga}) \tag{4.18}$$

an equation to estimate s_{ag} can be derived as

$$\left(I_{ga} - C_{ag0}\frac{dV_{ga}}{dt}\right)|V_{ga}|^{-1}s_{ag}^{\ 2} + \left(2I_{ga} - \frac{1}{2}C_{ag0}\frac{dV_{ga}}{dt}\right)C_{ag0}|V_{ga}|^{-1/2}s_{ag} + I_{ga}C_{ag0}^2 = 0 \tag{4.19}$$

s_{ag} is estimated from I_{ga} and V_{ga} using (4.19).

A test circuit for extracting C_{ak} and R_2 is shown in Fig. 4.7, where a resistor load is used so that dV_{ak}/dt is not zero during the turn-on and turn-off transients. The anode current I_a and the anode voltage V_{ak} can be obtained from the electrical measurements of

physical devices or from the circuit simulations of physic-based models. A behavioral model without the V_4 block is then applied in the simulation, which gives an anode current I_{a1}. The current

$$I_{a2} = I_a - I_{a1} \equiv V_4 \tag{4.20}$$

shown in Fig. 4.8 is used to extract C_{ak} and R_2.

The following approach allows C_{ak} and R_2 to be extracted from a linear matrix equation, although C_{ak} and R_2 are highly nonlinear. From the measured or simulated V_{ak}

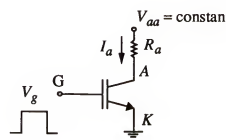

Figure 4.7 A test circuit for extracting C_{ak} and R_2 in the V_4 block.

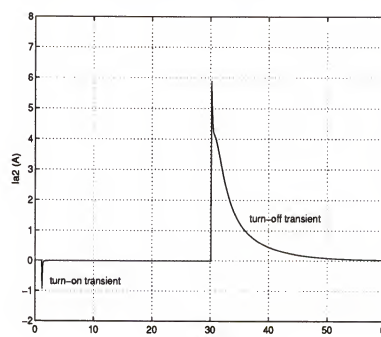

Figure 4.8 The waveform of I_{a2} (= V_4) used for extracting C_{ak} and R_2.

waveform, dV_{ak}/dt can be computed. Let $y(t) = I_{a2}(t) = V_4(t)$ and $u(t) = (dV_{ak}(t)/dt)/\sqrt{V_{ak}(t)} = V_3(t) / s_{ak}$, where $s_{ak} = s_{akon}$ for the turn-on transient, and $s_{ak} = s_{akoff}$ for the turn-off transient. Then in the s-domain:

$$\frac{Y(s)}{U(s)} = \frac{s_{ak}/(R_2C_2)}{s + 1/(R_2C_2)} \equiv \frac{\omega_2}{s + \omega_1} \tag{4.21}$$

Using a bilinear transformation,

$$s = \frac{2}{T}\left(\frac{1 - z^{-1}}{1 + z^{-1}}\right) \tag{4.22}$$

(4.21) is transformed from the s-domain to the z-domain. T in (4.22) is the sampling time. The sampling of the simulated waveforms is controlled by zsmp.sin and a2z.sin templates in the SABER circuit simulator [Sab92]. From $Y(z) \rightarrow y(n)$ and $z^{-1}Y(z) \rightarrow y(n-1)$, a difference equation is derived as

$$\frac{2}{T}[y(n) - y(n-1)] = -[y(n) + y(n-1)]\omega_1 + [u(n) + u(n-1)]\omega_2 \tag{4.23}$$

For N data points in the turn-on transient or in the turn-off transient, (4.23) can be written in a matrix form as

$$V = W\Omega \tag{4.24}$$

where $V = (2/T)[y(2)\text{-}y(1) \;\; y(3)\text{-}y(2) \ldots \; y(N)\text{-}y(N\text{-}1)]^T$, $\Omega = [\omega_1 \;\; \omega_2]^T$, and

$$W = \begin{bmatrix} -y(2) - y(1) & u(2) + u(1) \\ -y(3) - y(2) & u(3) + u(2) \\ \vdots & \vdots \\ -y(N) - y(N-1) & u(N) + u(N-1) \end{bmatrix} \tag{4.25}$$

The coefficient vector Ω can be readily computed as

$$\Omega = (W^T W)^{-1} W^T V \tag{4.26}$$

Thus, choosing C_2 = constant, $s_{ak} = s_{akoff}$ and $R_2 = R_{2off}$ can be extracted from the turn-off transient, and $s_{ak} = s_{akon}$ and $R_2 = R_{2on}$ from the turn-on transient. From the simulation results of various test circuits, it is noted that choosing C_{ak} as piecewise constants, i.e., C_{ak} = C_{akon} = constant for the turn-on transient and $C_{ak} = C_{akoff}$ = constant for the turn-off transient, is a good approximation as is evident from Figs. 4.12 and 4.13. To identify the constant parameters, $u(t) = (dV_{ak}(t)/dt)/\sqrt{V_{ak}}$ is replaced by $u(t) = dV_{ak}(t)/dt$, and the same identification procedure discussed above can be used.

The parameter R_{ak} in the alternative behavioral model is obtained from the assumption:

$$R_{ak} C_{ak} \approx R_2 C_2 \tag{4.27}$$

which gives $R_{ak} \approx R_{2off} C_2 / C_{akoff}$ for the turn-off transient, and $R_{ak} \approx R_{2on} C_2 / C_{akon}$ for the turn-on transient.

4.1.4 Model Evaluation and Validation

The behavioral model described above has been implemented in the SABER circuit simulator [Sab92]. The physics-based model described in Hefner and Diebolt [Hef91], which had been verified experimentally, was used to generate "measurement" data from which the parameters of the behavioral model are extracted. The extracted model parameters are listed in Table I. Figure 4.9 compares the static I-V characteristics offered by the behavioral model and by the physics-based model [Hef91]. Figure 4.10 shows the tailing of the anode currents simulated by the behavioral model and by the physics-based model [Hef91] at a constant anode voltage switching test. Figure 4.11(a) shows one of the transient test circuits. A soft clamp protection circuit is shown in Fig. 4.11(b), and a polarized active snubber protection circuit is shown in Fig. 4.11(c). The corresponding transient waveforms offered by the behavioral model are compared with

TABLE I. EXTRACTED MODEL PARAMETERS

Parameters	Values	Parameters	Values
C_1, C_2	1 nF	V_d	0.5 V
R_{1on}	250 Ω	V_{de}	0.7 V
R_{1off}	300 Ω	B_1	-1.210429
α	0.25	B_2	0.251083
R_{2on}	350 Ω	B_3	-1.736663e-3
R_{2off}	3500 Ω	B_4	1.384205e+4
C_{akon}	0.815 nF	B_5	6.76095e+3
C_{akoff}	60 nF	B_6 (V_{gk}<12V)	-1.749513e-2
C_{gk}	0.62 nF	B_7 (V_{gk}<12V)	3.702014e-2
C_{ag0}	1.86 nF	B_6 (V_{gk}>19V)	-0.222245
s_{ag}	0.45 n	B_7 (V_{gk}>19V)	1.336645e-2
V_t	4.7 V	B_6 (else)	0.0325 ($B_7 = 0$)

those generated by the physics-based model [Hef91] in Figs. 4.12 and 4.13. To obtain the simulation results shown in Fig. 4.12, the CPU times on a SPARCStation were 0.93 second for the circuit using the behavioral model, and 6.15 seconds for the circuit using the physics-based model.

A full-bridge converter shown in Fig. 4.14 was simulated using the behavioral IGBT model and the physics-based model [Hef91]. The simulated output voltage and current waveforms are shown in Fig. 4.15. The CPU times on a SPARCStation were 196 seconds for the circuit using the behavioral model, and 1290 seconds for the circuit using the physics-based model.

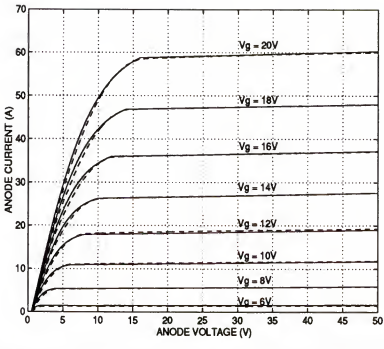

Figure 4.9 Simulated static I-V characteristics; solid line: behavioral model; dashed line: physics-based model [Hef91].

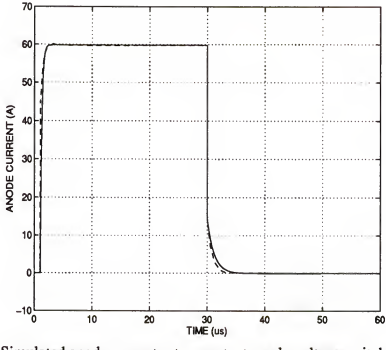

Figure 4.10 Simulated anode currents at a constant anode voltage switching test (V_{ak} = 40V, V_{gk} = 0V - 20V - 0V); solid line: behavioral model; dashed line: physics-based model [Hef91].

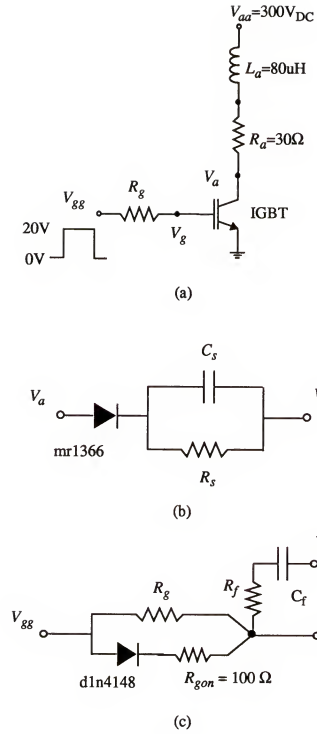

Figure 4.11 A test circuit with resistor and inductor load (a); a soft clamp protection circuit (b); and a polarized active snubber protection circuit (c).

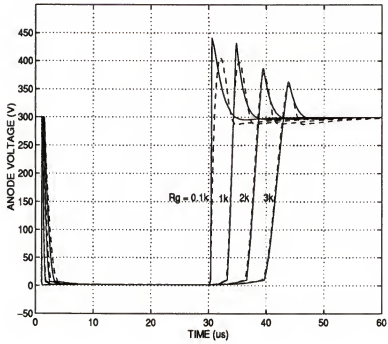

(a)

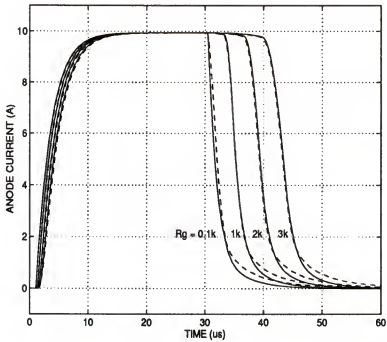

(b)

Figure 4.12 Simulated anode voltage (a); anode current (b); gate voltage (c); gate current (d) from the test circuit shown in Fig. 4.11(a); solid line: behavioral model; dashed line: physics-based model [Hef91].

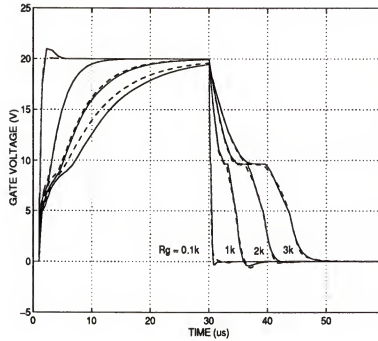

(c)

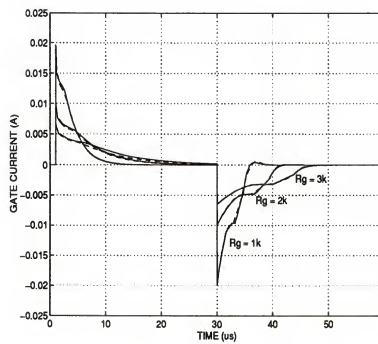

(d)

Figure 4.12 (continued)

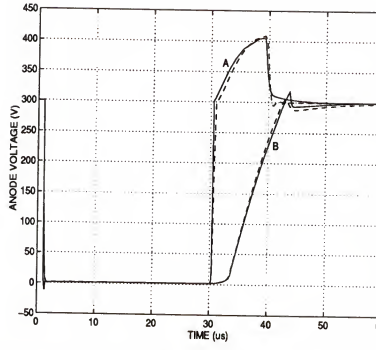

Figure 4.13 Simulated anode voltage waveforms with protection circuits; curve A: soft clamp with $R_g = 100\Omega$, $R_s = 1k\Omega$, $C_s = 200nF$, and $L_a = 200uH$; curve B: active snubber with $R_g = 1k\Omega$, $R_f = 1k\Omega$, $C_f = 0.2nF$, and $L_a = 80uH$; solid lines: behavioral model; dashed lines: physics-based model [Hef91].

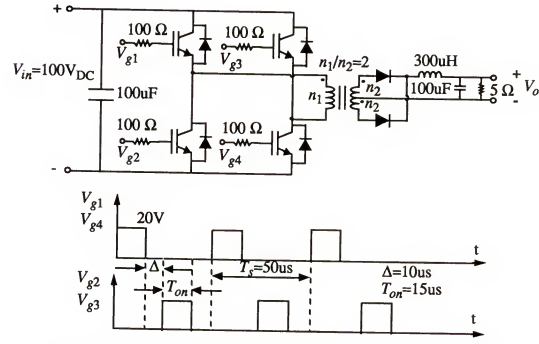

Figure 4.14 A full-bridge converter and the driving voltage waveforms

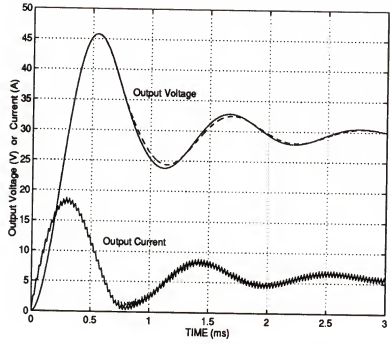

Figure 4.15 Simulated output voltage and current of the full-bridge converter shown in Fig. 4.14; solid line: behavioral model; dashed line: physics-based model [Hef91].

4.2 Vertical Double-Diffused MOSFET (VDMOS)

4.2.1 Introduction

Several Physics-based and behavioral models [She91, Kim90, Tsa93, Sco90, Yee88, Xu88] have been developed in recent years for the VDMOS. Although physics-based models give physical insights of the device, and are useful for device designers, those models are usually too complex for application engineers from the viewpoint of circuit simulation [She93, Lau90]. The most desirable feature of a circuit simulator model is its simplicity and ease with which the model parameters can be extracted [She91].

Based on the physical VDMOS model [Kim90], a behavioral model is constructed in this work to simplify the mathematical descriptions of the device for efficient circuit simulation. A standard nonlinear least-squares method, i.e., the Levenberg-Marquardt

method [Pre92], is used for parameter extractions. The physical VDMOS model [Kim90], which was modified [Tsa93] and implemented in the SABER circuit simulator, is used to generate the "experimental" data for extracting the model parameters and for comparison. Most of the model parameters in the physics-based behavioral model can be calculated from the physical parameters if they are available. Thus, the model parameters of the behavioral VDMOS model are either extracted from the same methods discussed for the IGBT device, or calculated from the physical parameters. The behavioral VDMOS model gives satisfactory simulation results for various test circuits in terms of efficiency and accuracy.

Since the physical model [Kim90] is based on the quasi-static approximations, the Hammerstein model configuration, which has been applied to model the dynamics of the IGBT, is not applied in this work. However, the Hammerstein model configuration may be applied to simplify the mathematics of some non-quasi-static MOSFET models [Par92, Pau83, Tur86, Man87], which are important for high frequency analog circuit simulation.

The model structure of the behavioral model will be described in Section 4.2.2. The accuracy and efficiency of the behavioral model are evaluated in Section 4.2.3.

4.2.2 Model Description

Figure 4.16(a) shows the cross section of a VDMOS structure. The main model structure of the proposed behavioral model is shown in Fig. 4.16(b). Figure 4.16(c) shows the model of the drain current I_d, which consists of five components. The first three components are used to model the drain current in the normal-mode operation ($V_{ds} > 0$), and the fourth and fifth components are used to model the drain current in the reverse-mode operation ($V_{ds} < 0$).

The first component of I_d is the dc drain current, $I_1 = I_{dc} = f(V_{gs}, V_{ds})$, which is modeled as follows:

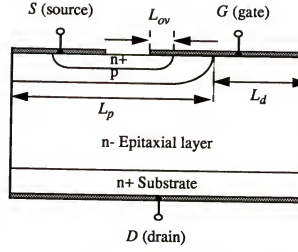

(a)

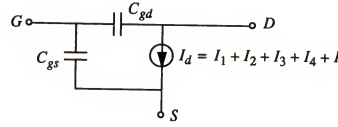

(b)

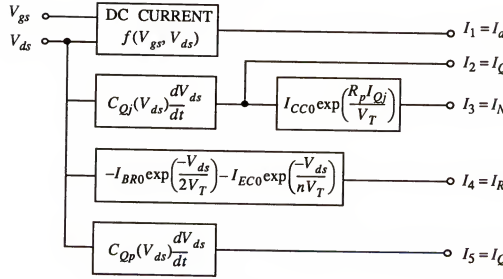

(c)

Figure 4.16 Cross section of a VDMOS structure (a); main structure of the behavioral model (b); and model structure for I_d (c).

$$I_{dc} = \begin{cases} 0 & \text{for } V_{gs} \le V_{th} \\ I_{sat} & \text{for } I_{lin} \ge I_{sat} \text{ and } V_{gs} > V_{th} \\ I_{lin} & \text{for } I_{lin} < I_{sat} \text{ and } V_{gs} > V_{th} \end{cases} \tag{4.28}$$

where

$$I_{sat} = W v_{sat} C_{ox} (V_{gs} - V_{th}) \equiv G_{sat} (V_{gs} - V_{th}) \tag{4.29}$$

$$I_{lin} = \frac{A_1 V_{ds} + A_2 V_{ds}^2}{1 + A_3 V_{ds}} \tag{4.30}$$

The current I_{sat} is the DC drain current (= DC channel current) in the saturation region, and can be obtained from the physical model [Kim90] as shown in (4.29), where W is the device width, v_{sat} the saturation drift velocity, C_{ox} the oxide capacitance per unit area, and V_{th} the MOSFET threshold voltage. The parameters G_{sat} and V_{th} can be extracted from the static I-V curves by applying two sets of (V_{gs}, I_{sat}) data points in (4.29). The current I_{lin} is used to fit the DC drain current in the linear and quasi-saturation regions. For the device studied in Kim and Fossum [Kim90], A_1, A_2, and A_3 can be modeled as constants since the static I-V curves in the linear and quasi-saturation regions are almost independent of V_{gs}. However, for the device studied in Shenai [She91], A_1, A_2, and A_3 need to be modeled as functions of V_{gs}.

The second and third components of I_d are the junction depletion current and the parasitic BJT current in the normal mode, respectively. From (14) in Kim and Fossum [Kim90], the parasitic BJT current is modeled as

$$I_{ct} = I_{CC0} \exp\left(\frac{V_{BEn}}{V_T}\right) - I_{EC0} \exp\left(\frac{V_{BCn}}{V_T}\right) \tag{4.31}$$

where I_{CC0} is the parasitic BJT collector saturation current, I_{EC0} the parasitic BJT emitter saturation current, and V_T the thermal voltage. The BJT current in the normal mode is controlled by $V_{BEn} = V_{Rp} = R_p I_{Qj}$, and the BJT current in the reverse mode is controlled by $V_{BCn} = -V_{ds} / n$, where n is a scaling parameter in the behavioral model to account for the

voltage drop in the drift region. From (4.31), the normal-mode BJT current is written as

$$I_N = I_{CC0}\exp\left(\frac{R_p I_{Qj}}{V_T}\right) \tag{4.32}$$

The voltage drop V_{Rp} in the p-body resistance R_p is due to the body-drift junction depletion charge Q_J, and is calculated from

$$\begin{aligned} V_{Rp} &= R_p I_{Qj} = R_p \frac{dQ_J}{dt} = R_p q W L_p N_D \frac{dW_d}{dt} \\ &\approx R_p \left(W L_p \sqrt{\frac{\varepsilon_s q N_D}{2 V_{ds}}} \right) \frac{dV_{ds}}{dt} \equiv R_p C_{Qj}(V_{ds}) \frac{dV_{ds}}{dt} \end{aligned} \tag{4.33}$$

where L_p is the lateral distance from channel edge to middle of the source contact, ε_s the silicon permittivity, N_D the drain donor concentration, and q the electron charge. The capacitance C_{Qj} can be expressed as

$$C_{Qj}(V_{ds}) \approx \frac{s_{Qj}}{\sqrt{V_{ds}}} \tag{4.34}$$

where

$$s_{Qj} = W L_p \sqrt{\frac{\varepsilon_s q N_D}{2}} \tag{4.35}$$

is the parameter in the behavioral model.

The static drain current in the behavioral model is equal to the static channel current in the physical model [Kim90]. When the parasitic BJT current starts to conduct in the normal-mode operation, the channel voltage will reduce because of larger voltage drop in the drift region, which will result in a smaller channel current in the linear region. This effect is not modeled in (4.30), however, it can be approximately included by extracting a slightly smaller I_{CC0}.

The fourth component of I_d is the static reverse-mode current I_R. The reverse-mode base current I_{BR} is modeled as

$$I_{BR} = -I_{BR0}\exp\left(\frac{-V_{ds}}{2V_T}\right) \tag{4.36}$$

where I_{BR0} is a constant. The second term in (4.31) can be combined with (4.36) to represent the static reverse-mode current,

$$I_R = -I_{BR0}\exp\left(\frac{-V_{ds}}{2V_T}\right) - I_{EC0}\exp\left(\frac{-V_{ds}}{nV_T}\right) \tag{4.37}$$

The fifth component of I_d is the dynamic reverse-mode current $I_{Qp} = dQ_p/dt$, where Q_p is the hole charge stored in the drift region. From the relation $Q_p = \tau_H I_{BR}$, where τ_H is the high-injection carrier lifetime, we can derive

$$\begin{aligned} I_{Qp} &= \frac{dQ_p}{dt} = \tau_H \frac{dI_{BR}}{dt} = \tau_H\left(\frac{dI_{BR}}{dV_{ds}}\right)\frac{dV_{ds}}{dt}\right) \\ &= \left[\frac{\tau_H I_{BR0}}{2V_T}\exp\left(\frac{-V_{ds}}{2V_T}\right)\right]\frac{dV_{ds}}{dt} \equiv C_{Qp}(V_{ds})\frac{dV_{ds}}{dt} \end{aligned} \tag{4.38}$$

The capacitance C_{Qp} can be expressed as

$$C_{Qp}(V_{ds}) = s_{Qp}\exp\left(\frac{-V_{ds}}{2V_T}\right) \tag{4.39}$$

where

$$s_{Qp} = \frac{\tau_H I_{BR0}}{2V_T} \tag{4.40}$$

is the parameter in the behavioral model. Note that the channel current also contributes to the drain current in the reverse-mode operation, but it is much smaller than I_R in (4.37), and can be neglected.

Both the capacitances C_{gs} and C_{gd} can be modeled as functions of V_{gs} and V_{ds} for a better performance [Bud94]. The drain-source capacitance C_{ds} is included in the model by the junction depletion charge Q_J. The capacitance C_{gs} affects both the gate current and the gate voltage waveforms, the capacitance C_{gd} dominates the drain switching waveforms in a PWM circuit through the "Miller" effect, and the capacitance C_{ds} is important in zero-voltage switching circuits and in damping the overshoot of the drain source voltage V_{ds} in unclamped inductor-load circuits [Bud94]. In the normal-mode operation, C_{gs} can be simply modeled as a constant, and C_{gd} can be modeled as a function of V_{gd}. The constant capacitance C_{gs} can be extracted from electrical measurements or can be calculated from

$$C_{gs} = L_{ov} W C_{ox} \tag{4.41}$$

where L_{ov} is the length of the gate/source overlap. In the behavioral model, C_{gd} is modeled as

$$C_{gd} = \begin{cases} C_{gd0} & \text{for } V_{gd} \geq 0 \\ \dfrac{C_{gd0} \cdot C_{gdj}}{C_{gd0} + C_{gdj}} & \text{for } V_{gd} < 0 \end{cases} \tag{4.42}$$

where C_{gd0} is the gate/drain oxide capacitance, and C_{gdj} the gate/drain junction depletion capacitance. The oxide capacitance C_{gd0} can be calculated from

$$C_{gd0} \approx L_d W C_{ox} \tag{4.43}$$

where L_d is the lateral distance from channel edge to gate midpoint. The depletion capacitance C_{gdj} can be approximated as

$$C_{gdj} \approx s_1 L_d W \sqrt{\frac{\varepsilon_s q N_D}{2|V_{gd}|}} \approx \frac{s_{gd}}{\sqrt{|V_{gd}|}} \tag{4.44}$$

where s_1 is a scaling factor to account for the voltage drop in the drift region, and s_{gd} is the parameter in the behavioral model.

4.2.3 Model Evaluation and Validation

The behavioral model of the VDMOS described above has been implemented in the SABER circuit simulator [Sab92]. The physical model described in [Kim90, Tsa93] was used to extract the model parameters. Figure 4.17 compares the static I-V characteristics offered by the behavioral model and by the physical model. Figure 4.18 shows one of the transient test circuits. The corresponding transient waveforms offered by the behavioral model are compared with those generated by the physical model in Fig. 4.19 for different L_d values, and in Fig. 4.20 for different R_g values.

A PS-ZVS-PWM (Phase-Shifted Zero-Voltage-Switching Pulse-Width-Modulation) converter [Vla92] is simulated using the behavioral model and the physical model. The simulated output voltages and currents are shown in Fig. 4.21. The CPU times on a SPARCStation were 198 seconds for the circuit using the behavioral model and 702 seconds for the circuit using the physical model.

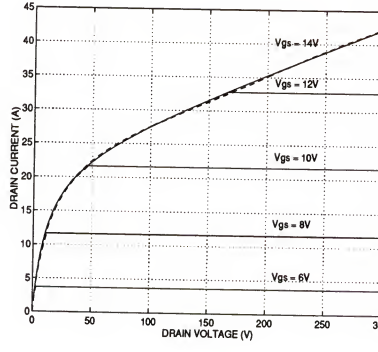

Figure 4.17 Simulated static I-V characteristics; Solid line: behavioral model; dashed line: physical model [Tsa93].

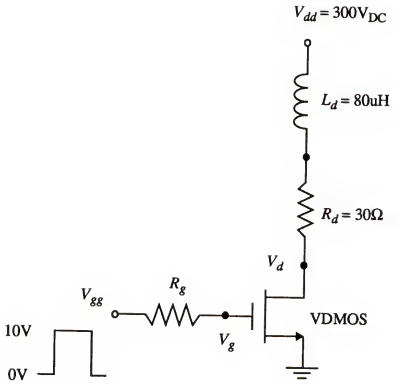

Figure 4.18 A test circuit with resistor and inductor load.

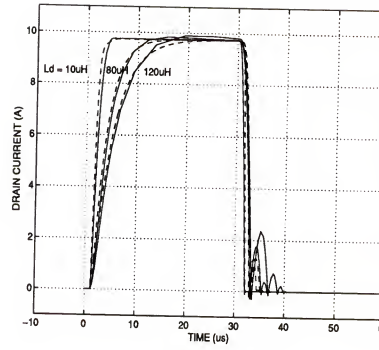

(a)

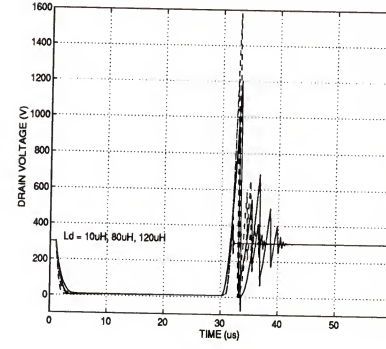

(b)

Figure 4.19 Simulated drain currents (a); drain voltages (b) at different L_d (with R_d=30Ω, R_g=1kΩ) from the test circuit shown in Fig. 4.18; solid line: behavioral model; dashed line: physical model [Tsa93].

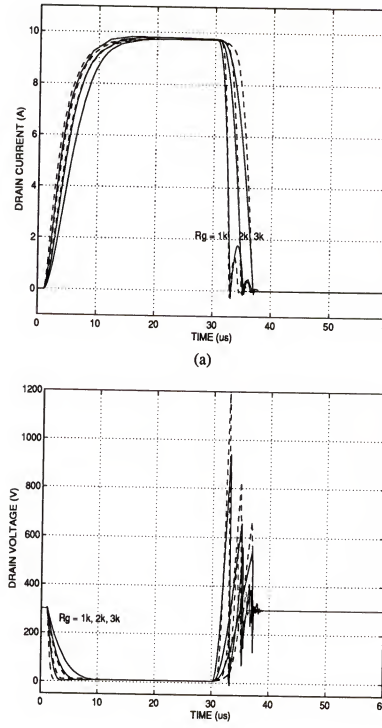

Figure 4.20 Simulated drain currents (a); drain voltages (b) at different R_g (with R_d = 30Ω, L_d = 80uH) from the test circuit shown in Fig. 4.18; solid line: behavioral model; dashed line: physical model [Tsa93].

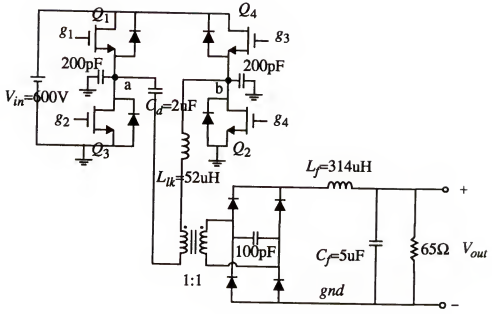

(a)

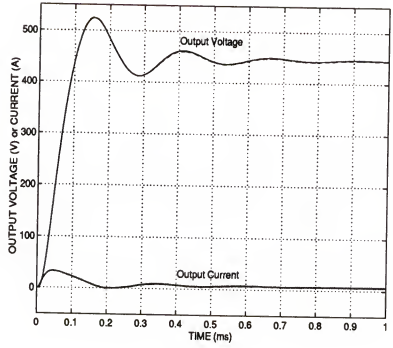

(b)

Figure 4.21 A Phase-Shifted Zero-Voltage-Switching PWM converter (a); and the simulated output voltages and currents (b); solid line: behavioral model; dashed line: physical model [Tsa93]. Note that the solid lines and the dashed lines are almost identical.

4.3 Summary

The configuration of the Hammerstein model, which includes a nonlinear static block followed by a linear dynamic block, has been applied to model the dynamics of the IGBT. Unlike the linear dynamic block in a true Hammerstein model, the dynamic block employed in the behavioral model is piecewise linear. For simplicity, only first-order approximations are used in the dynamic blocks, which give satisfactory simulation results for various test circuits in terms of efficiency and accuracy. For higher accuracy, higher-order approximations may be applied.

Using least-squares methods, the model parameters can be extracted from the electrical measurements of physical devices, or from the circuit simulations of physics-based models. Several other linear and nonlinear system identification theories, which are not used in this work, can also be applied for parameter extractions. Although the behavioral IGBT model presented herein is derived without solving any semiconductor equations, it is believed that nonlinear system identification theories can be applied to simplify the solutions from the semiconductor equations so that efficient physics-based models of the semiconductor devices can be obtained.

A physics-based behavioral model of the VDMOS has been presented and implemented in the SABER circuit simulator. This behavioral VDMOS model gives satisfactory simulation results for various test circuits in terms of efficiency and accuracy, but is less accurate than the physical model over wide ranges of operating/application conditions. The main reason of the slight inaccuracy is that the voltage drop in the drift regions is only approximately accounted for by some scaling parameters. Another behavioral model is constructed using the subcircuit topology and equations discussed in [Kim90], but using a voltage-dependent drift resistor to model the drift region; this model also increases the simulation speed while maintaining good accuracy.

To incorporate thermal effects into the behavioral models, different sets of model parameters can be extracted from the measured or simulated current and voltage waveforms at different temperatures; then these model parameters can be modeled as piecewise linear functions of temperature using the built-in function *pwl1* in SABER.

CHAPTER 5
A RATE-DEPENDENT AND TEMPERATURE-DEPENDENT HYSTERESIS MODEL

5.1 Introduction

Since magnetic devices have become almost indispensable parts in power electronic systems, an accurate modeling of magnetic devices is important for an accurate prediction of the performance of power electronic systems. Magnetic hysteresis plays an important role in the nonlinear behavior of magnetic devices, and the hysteresis loops are useful in the core-loss evaluation. To achieve the goal of accurate modeling of magnetic devices, an accurate hysteresis model is needed. In the literature, several hysteresis models [Pre35, Eve55, Jil86, Ath87, May88, Tor88, Ber92] are available. A recent survey on the magnetic hysteresis models was discussed in Takach and Lauritzen [Tak95].

Motivated by the goal of simulating the dynamically coupled magnetic and thermal systems, this chapter presents a rate-dependent and temperature-dependent hysteresis model, which is built by a structure similar to the Hammerstein model [Nar66, Bil80, Esk91]. However, the model used here differs from the Hammerstein model in that the static block in the present model is not only static but also history-dependent due to the wiping-out property of the hysteresis phenomena. The Preisach model [Pre35] was first proposed in 1935, but the classical (scalar) Preisach model does not describe the reversible magnetization and is rate-independent. Modifications of the classical Preisach model are needed. The static block in the proposed model structure is realized by a modified Preisach model, and the dynamic block by a low-pass filter. To modify the classical Preisach model, we modify the equations derived in Naidu [Nai90] to account for both the irreversible and the reversible components of magnetization. The rate-dependent effects are accounted for by the dynamic block, and the temperature-dependent effects are

included in the proposed model by using temperature-dependent model parameters extracted from experimental data at different temperatures. It was found that the rate-dependent physical model discussed in Jiles [Jil93] is simply a special case of the present model using a second-order approximation in the dynamic block.

Physical background of the magnetic dipole moment (which is the basic physics in Preisach's theory) and the hysteresis phenomena due to the domain wall motion are reviewed in Section 5.2. The proposed model structure is described in Section 5.3. Parameter extraction and implementation are discussed in Section 5.4, and the accuracy of the proposed model is verified in Section 5.5.

5.2 Physical Background

5.2.1 Magnetic Dipole Moment

An atomic magnetic dipole with its associated magnetic moment is the result of three sources of moments on the atomic scale: the orbital electron, the electron spin, and the nuclear spin [Ski82]. In general, the nuclear spin magnetic moment has minimal effect on magnetic properties since its moment is smaller by a factor of 10^{-3} than that due to an orbital electron or electron spin. The net effect of these sources of magnetic moment on the atomic or microscopic base can be represented by magnetic current loops. The current loop is known as the magnetic dipole for historical reasons, since the field produced by such a current loop is identical in form to the field produced by two hypothetical magnetic poles [Jil91].

Figure 5.1 shows a schematic representation of a number of atomic current loops, each of area A. The magnetization $\boldsymbol{M}$ can be written as

$$\boldsymbol{M} = n\boldsymbol{u}_m = \frac{Ni}{l} \tag{5.1}$$

where N/l is the number of atomic current loops per unit length, i the circulating current, $\boldsymbol{u}_m$ the magnetic moment, and $n = N/(Al)$ the number of atomic current loops per unit

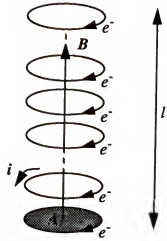

Figure 5.1 A schematic representation of a number of atomic loops [Oha94].

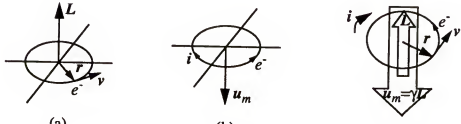

Figure 5.2 Angular momentum of a circulating electron (a); magnetic moment of a circulating electron (b); and a schematic representation (c).

volume. From (5.1), the magnetic dipole moment can be derived as

$$u_m = iA \tag{5.2}$$

For a hydrogen atom on the Bohr model, $u_m \approx 9.27 \times 10^{-24} \mathrm{Am}^2$. Some molecules such as those in a permanent magnet possess permanent magnetic dipole moment. For a ferromagnetic material, an applied magnetic field can induce a magnetic moment, and the magnetization is the magnetic dipole moment per unit volume.

A further illustration of the magnetic dipole moment is shown in Fig. 5.2. An electron with orbital angular momentum is in effect a circulating current, and so there is also a magnetic moment arising from the orbital momentum. The angular momentum is expressed as

$$\boldsymbol{L} = m(\boldsymbol{r} \times \boldsymbol{v}) \tag{5.3}$$

where m is the rest mass of the electron, $\boldsymbol{r}$ the vector of the radius, and $\boldsymbol{v}$ the vector of the circular drift velocity. From $u_m = iA \approx e(\omega/2\pi)\pi r^2$, $\omega = v/r$, and $L = mrv$ (the magnitude of $\boldsymbol{L}$), we can derive

$$u_m = (e/2m)L \equiv \Upsilon L \tag{5.4}$$

where Υ is called the gyromagnetic ratio. Note that $\boldsymbol{L}$ and $\boldsymbol{u_m}$ are in opposite direction since e (the electron charge) is a negative number.

The magnetic dipole moment possessed by one electron spin is one Bohr magneton, the same as orbital motion. But the angular momentum of spin is only half as much, corresponding to the quantum number for spin of $m_s = 1/2$. Thus, the electron spin and electron orbital motion differ by a factor of 2 in the gyromagnetic ratio. In general, the gyromagnetic ratio Υ can be expressed as

$$\Upsilon = g(e/2m) \tag{5.5}$$

where $g = 2$ for a system of pure spin, and $g = 1$ for purely orbital. The g factor can be determined experimentally. For the three common ferromagnetic elements (iron, cobalt, and nickel), the g factor is close to 2 since the magnetic moments are caused by spins with most of the orbital contribution described as "quenched" [Wat85].

5.2.2 Hysteresis

Figure 5.3(a) shows a hysteresis B (magnetic flux density) - H (magnetic field) loop. Initially, the magnetic material is in the demagnetized state (B=0), and the corresponding domain wall is shown in Fig. 5.3(b). When the applied magnetic field H is increased, the domain wall starts to move to the right as shown in Fig. 5.3(c), and the total flux density B (or magnetization M) is increased until B_{sat} (or M_{sat}) is reached. After reaching B_{sat} (or M_{sat}), the applied magnetic field H is then reduced, and the domain wall starts to move back to the left as shown in Fig. 5.3(d). However, when the applied

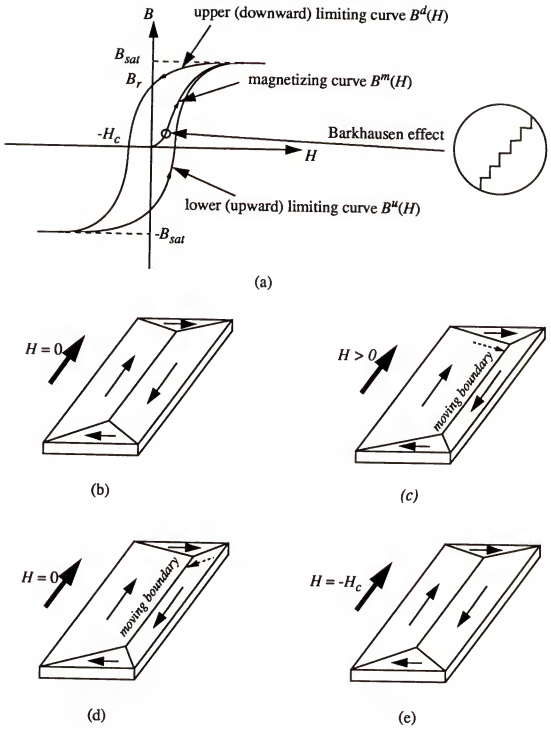

Figure 5.3 A hysteresis (*B-H*) loop (a); the approximated domain structure for the demagnetized state (b); for approach to saturation (c); for approach to the demagnetized state (d); and for the demagnetized state (e).

magnetic field H is reduced to zero, the magnetic flux density B is not zero since the domain wall motion is not reversible, which is due to the energy loss in the domain wall motion. The magnetic flux density B (or magnetization M) remained in the material when the applied magnetic field H is zero is called the residual induction B_r (or remanence M_r). To restore the magnetic flux density B to zero as shown in Fig. 5.3(e), a reverse magnetic field is needed, and this reverse magnetic field is called the coercivity or coercive field H_c.

Because energy is lost when a domain wall jumps abruptly from one local energy minimum to the next (Barkhausen jumps), the domain wall motion is an irreversible, lossy process. When lossy processes are involved, the B-H loop opens up, i.e., it shows hysteresis. Note that the Barkhausen effect is the phenomenon of discontinuous changes in the magnetic flux density B within a ferromagnet as the magnetic field H is changed continuously [Jil91].

5.3 Model Description

The model structure of the proposed rate-dependent and temperature-dependent hysteresis model is shown in Fig. 5.4, which is similar to a Hammerstein model except that the static block is not only static but also history-dependent. The static (DC) block is realized by a modified Preisach model, and the dynamic block by a low-pass filter with first-order, second-order, or third-order approximations. The temperature effects are included in the model by fitting the model parameters as functions of temperature.

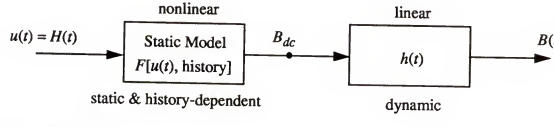

Figure 5.4 Model structure of the rate-dependent and temperature-dependent hysteresis model.

5.3.1 Static (DC) Model

For the completeness and clarity of the presentation, the classical Preisach model is reviewed in this section, and the main equations [Nai90] for the implementation of the Preisach model are re-derived. Two approaches applied in this work to include the reversible magnetization are also discussed.

In Preisach's theory, the physical concept of magnetic dipoles is used to describe the hysteresis phenomena. The theory assumes that the ferromagnetic material is made up of elemental magnetic dipoles, which have rectangular hysteresis loops as shown in Fig. 5.5, where h_c is the coercivity of a dipole, h_m is a field due to neighboring dipoles, and $\alpha = h_m + h_c$, $\beta = h_m - h_c$. The existence of coercivity can be explained by the lossy domain wall motion which is caused by the presence of pinning sites in the material such as non-magnetic inclusions, voids, or regions of inhomogeneous stress [Jil86]. These pinning sites are statistically distributed inside the material. It was stated [May91] that the asymmetrical rectangular loops ($\alpha \neq -\beta$) in the Preisach model are not physical for single magnetic dipoles. The use of asymmetrical loops is commonly justified by the fact that asymmetry is caused by the interaction between the magnetic dipoles. More precisely, this means that each magnetic dipole "feels" not only the applied magnetic field $H(t)$, but also the interaction magnetic field which is due to the magnetization of adjacent dipoles. The interaction magnetic field may, of course, vary from one dipole to another. Thus, the parameters h_c and h_m are statistically distributed, and so are the parameters α and β. The

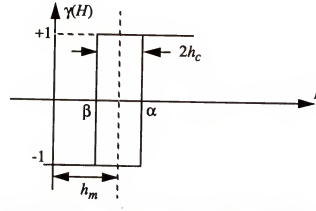

Figure 5.5 Rectangular hysteresis loop of a magnetic dipole.

Preisach diagram used to describe the hysteresis phenomenon can be drawn in the h_c-h_m coordinates or in the α-β coordinates.

The relation of the magnetic flux density B and the magnetic field H in the h_c-h_m coordinates is expressed as

$$B(H) = \int_S u(h_c, h_m)\gamma(H)dh_c dh_m$$

$$= \int_{S+} u(h_c, h_m)dh_c dh_m - \int_{S-} u(h_c, h_m)dh_c dh_m \tag{5.6}$$

where S is the area of the triangular mathematical domain in the Preisach diagram (which will be determined later), $S+$ the area of positive magnetization, $S-$ the area of negative magnetization, and $u(h_c, h_m)$ the statistical distribution function which has the following properties:

$$u(h_c, h_m) = 0 \quad \text{for } h_c < 0$$
$$u(h_c, h_m) = u(h_c, -h_m) \tag{5.7}$$

The function $\gamma(H)$ is defined as: $\gamma(H) = +1$ on the area $S+$, and $\gamma(H) = -1$ on the area $S-$. A different definition is $\gamma(H) = +B_{sat}$ on the area $S+$, and $\gamma(H) = -B_{sat}$ on the area $S-$. However, the B_{sat} term can be always incorporated into the expression of $u(h_c, h_m)$. Note that some authors described the Preisach model using $M(H)$ vs. H. Since $B(H) = \mu_0(M(H) + H) \approx \mu_0 M(H)$, we can always describe the Preisach model using $B(H)$ vs. H as in (5.6). Moreover, the neglected term $\mu_0 H$ can be always added back to (5.6), so that the slope of the saturation curve in the B-H loop is μ_0 instead of zero.

The h_c-h_m coordinates can be transformed to the α-β coordinates, and the relation between B and H in the α-β coordinates is expressed as

$$B(H) = \int_S u(\alpha, \beta)\gamma(H)d\alpha d\beta = \int_{S+} u(\alpha, \beta)d\alpha d\beta - \int_{S-} u(\alpha, \beta)d\alpha d\beta \tag{5.8}$$

where $u(\alpha, \beta)$ satisfies

$$u(\alpha, \beta) = 0 \quad \text{for } \alpha - \beta < 0$$
$$u(\alpha, \beta) = u(-\beta, -\alpha) \tag{5.9}$$

which can be derived from (5.7). The triangular mathematical domain of the Preisach diagram, i.e., the closed area where $u(h_c, h_m) \neq 0$ (or $u(\alpha, \beta) \neq 0$), is determined from

$$h_c \geq 0,\ h_m + h_c \leq H_{sat},\ \text{and}\ h_m - h_c \geq -H_{sat} \tag{5.10}$$

in the h_c-h_m coordinates, or from

$$\alpha - \beta \geq 0,\ \alpha \leq H_{sat},\ \text{and}\ \beta \geq -H_{sat} \tag{5.11}$$

in the α-β coordinates.

Initially, the demagnetized state ($B = 0$) is described by the Preisach diagram shown in Fig. 5.6(a) (in the h_c-h_m coordinates) and in Fig. 5.6(b) (in the α-β coordinates). The positive magnetization (regions I and III) is due to those dipoles having $h_m < H = 0$ (or $\alpha + \beta < H = 0$), and the negative magnetization (regions II and IV) is due to those dipoles having $h_m > H = 0$ (or $\alpha + \beta > H = 0$). The magnetization process will be explained in the α-β coordinates for the major loop and for the minor loops.

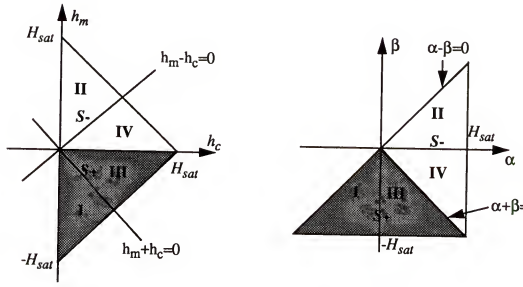

Figure 5.6 Preisach diagrams for the demagnetized state in the h_c-h_m coordinates (a); and in the α-β coordinates (b).

5.3.1.1 Major loop

The generation of the major loop for a ferromagnetic material will be explained using the Preisach diagrams shown in Fig. 5.7. When H is increased from the initial demagnetized state, those dipoles having $\alpha < H$ will flip from negative magnetization to positive magnetization as shown in Fig. 5.7(b). The initial magnetization process (p_1-p_2) continues until H (or B) reaches H_{sat} (or B_{sat}), i.e., the S+ area covers all the triangular domain in the Preisach diagram. When H is decreased from H_{sat}, those dipoles having $\beta > H$ will flip from positive magnetization to negative magnetization as shown in Fig. 5.7(c). The descending curve (p_2-p_3-p_4) continues until H (or B) reaches $-H_{sat}$ (or $-B_{sat}$), i.e., the S- area covers all the triangular domain in the Preisach diagram. When H is

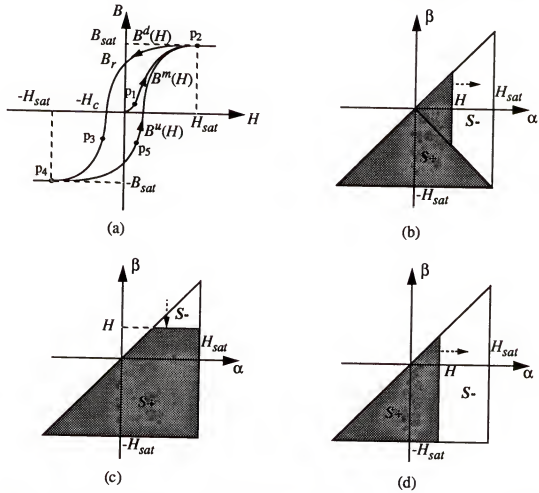

Figure 5.7 A hysteresis loop (a); Preisach diagram for the initial magnetization curve (b); for the downward limiting curve (c); and for the upward limiting curve (d).

increased from $-H_{sat}$, those dipoles having $\alpha < H$ will again flip from negative magnetization to positive magnetization as shown in Fig. 5.7(d). The magnetization process (p_4-p_5-p_2) continues until H (or B) reaches H_{sat} (or B_{sat}), and a hysteresis loop, i.e., the major loop, is thus completed.

Based on the method of separation of variables, we can assume

$$u(\alpha, \beta) = u_x(\alpha)u_y(\beta) \tag{5.12}$$

From the symmetry condition defined in (5.9), we can write

$$u_x(\alpha)u_y(\beta) = u_x(-\beta)u_y(-\alpha) \tag{5.13}$$

which gives

$$u_x(\alpha) = u_y(-\alpha) \text{ and } u_y(\beta) = u_x(-\beta) \tag{5.14}$$

Thus, $u(\alpha, \beta)$ can be expressed as

$$u(\alpha, \beta) = u_x(\alpha)u_x(-\beta) \tag{5.15}$$

The downward limiting curve $B^d(H)$ for $H \geq 0$ is obtained by integrating $u(\alpha, \beta)$ inside Area(abdef) as shown in Fig. 5.8(a), for the integrations inside Area(abg) and Area(deh) sum to zero due to the symmetry condition of $u(\alpha, \beta)$. Because there is no dipoles inside Area(bcd), the integration inside Area(abdef) is equal to that inside Area(acef). Thus, we can write

$$\begin{aligned} B^d(H) &= \iint_{\text{acef}} u_x(\alpha)u_x(-\beta)d\alpha d\beta = \int_{-H}^{H_{sat}} u_x(\alpha)d\alpha \int_{-H_{sat}}^{H} u_x(-\beta)d\beta \\ &= \int_{-H}^{H_{sat}} u_x(\alpha)d\alpha \int_{-H}^{H_{sat}} u_x(\beta)d\beta \equiv F(-H) \cdot F(-H) \end{aligned} \tag{5.16}$$

where $F(H)$ is defined as

$$F(H) \equiv \int_{H}^{H_{sat}} u_x(\alpha)d\alpha \tag{5.17}$$

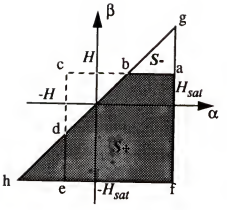

(a)

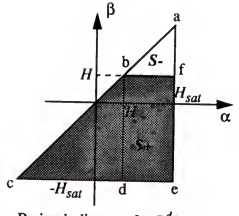

Preisach diagram for $B^d(H)$

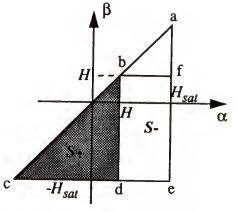

Preisach diagram for $B^u(H)$

(b)

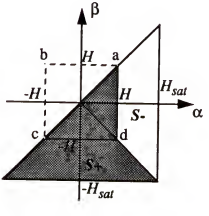

(c)

Figure 5.8 Preisach diagrams for deriving $B^d(H)$ for $H \geq 0$ (a); for deriving $B^d(H)$-$B^u(H)$ (b); and for deriving $B^m(H)$ (c); as functions of $F(H)$.

From (5.16), we can write

$$F(-H) = \sqrt{B^d(H)} \qquad \text{for } H \geq 0 \tag{5.18}$$

From Fig. 5.8(b), the difference between the downward limiting curve $B^d(H)$ and the upward limiting curve $B^u(H)$ is obtained by integrating $u(\alpha, \beta)$ inside the following area:

Integration area of $B^d(H)$ - integration area of $B^u(H)$

= [Area(bcef) - Area(abf)] - [Area(bcd) - Area(abde)]

= [Area(bcef) - Area(bcd)] + [Area(abde) - Area(abf)]

= 2 Area(bdef).

Thus, we can write

$$B^d(H) - B^u(H) = 2\int\int_{\text{bdef}} u_x(\alpha)u_x(-\beta)d\alpha d\beta = 2\int_{H}^{H_{sat}} u_x(\alpha)d\alpha \int_{-H_{sat}}^{H} u_x(-\beta)d\beta$$

$$= 2\int_{H}^{H_{sat}} u_x(\alpha)d\alpha \int_{-H}^{H_{sat}} u_x(\beta)d\beta = 2F(H)F(-H) \tag{5.19}$$

From (5.18) and (5.19), we can obtain

$$F(H) = \frac{B^d(H) - B^u(H)}{2\sqrt{B^d(H)}} = \frac{B^d(H) + B^d(-H)}{2\sqrt{B^d(H)}} \qquad \text{for } H \geq 0 \tag{5.20}$$

where a symmetric hysteresis loop is assumed, i.e., $B^u(H) = -B^d(-H)$ [Nai90]. Thus, the function $F(H)$ for both $H \geq 0$ and $H \leq 0$ can be calculated from $B^d(H)$ as defined in (5.18) and (5.20). The function $F(H)$ is useful in describing the minor loops, which will be discussed later.

From Fig. 5.8(c), the initial magnetization curve $B^m(H)$ is obtained by integrating $u(\alpha, \beta)$ inside Area(acd). Since the integration inside Area(acd) is equal to that inside Area(abcd), we can write

$$B^m(H) = \int\int_{abcd} u_x(\alpha)u_x(-\beta)d\alpha d\beta = \int_{-H}^{H} u_x(\alpha)d\alpha \int_{-H}^{H} u_x(-\beta)d\beta$$

$$= \int_{-H}^{H} u_x(\alpha)d\alpha \int_{-H}^{H} u_x(\beta)d\beta = [F(-H) - F(H)]^2$$

$$= \left[\sqrt{B^d(H)} - \frac{B^d(H) + B^d(-H)}{2\sqrt{B^d(H)}}\right]^2 = \frac{[B^d(H) - B^d(-H)]^2}{4B^d(H)} \qquad (5.21)$$

for $H \geq 0$. Thus, the initial magnetization curve $B^m(H)$ can be calculated from $B^d(H)$.

5.3.1.2 Minor loops

To describe the minor loops, we need to define the principal trajectories, for the trajectory of a minor loop starting from any arbitrary reversal point is parallel to the corresponding principal trajectory [Nai90]. The principal trajectories are those trajectories which start from a reversal point on the limiting hysteresis loop (the major loop). As shown in Fig. 5.9(a), the principal upward trajectory $B^u_{H_1}(H)$ starts from $H = H_1$ on the downward limiting curve $B^d(H)$ and moves upward to positive saturation; the principal downward trajectory $B^d_{H_2}(H)$ starts from $H = H_2$ on the upward limiting curve $B^u(H)$ and moves downward to negative saturation. Figure 5.9(b) shows the Preisach diagrams for path(5-6) and path(1-3-2). It is easily seen that path(5-6) is parallel to path(1-3-2) since the incremental integration areas in both paths are the same. In general, the upward (downward) trajectory of a minor loop is parallel to the corresponding principal upward (downward) trajectory, which is the basic rule for generating the minor loops.

From Fig. 5.9(c), the difference between $B^d(H)$ and $B^d_{H_2}(H)$ is obtained by integrating $u(\alpha, \beta)$ inside the following area:

Integration area of $B^d(H)$ - integration area of $B^d_{H_2}(H)$

= [Area(bcef) - Area(abf)] - [Area(bcdg) - Area(abgde)]

= [Area(bcef) - Area(bcdg)] + [Area(abgde - Area(abf)]

= 2 Area(defg).

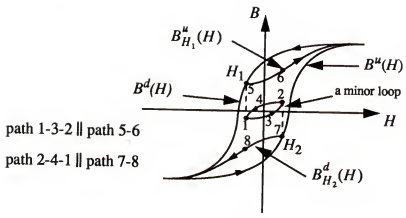

(a)

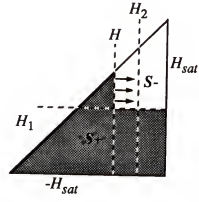

Preisach diagram for path(5-6)

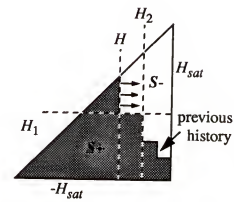

Preisach diagram for path(1-3-2)

(b)

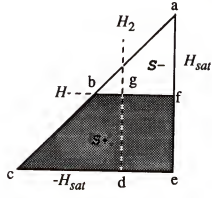

Preisach diagram for $B^d(H)$

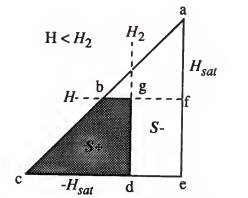

Preisach diagram for $B^d_{H_2}(H)$

(c)

Figure 5.9 Principal trajectories and a minor loop in the *B-H* plane (a); Preisach diagrams for path(5-6) and path(1-3-2) (b); Preisach diagrams for deriving $B^d(H)$ - $B^d_{H_2}(H)$ (c).

Thus, we can write

$$B^d(H) - B^d_{H_2}(H) = 2\int\int_{defg} u_x(\alpha)u_x(-\beta)d\alpha d\beta = 2\int_{H_2}^{H_{sat}} u_x(\alpha)d\alpha \int_{-H_{sat}}^{H} u_x(-\beta)d\beta$$

$$= 2\int_{H_2}^{H_{sat}} u_x(\alpha)d\alpha \int_{-H}^{H_{sat}} u_x(\beta)d\beta = 2F(H_2)F(-H) \qquad (5.22)$$

Similarly, from Fig. 5.10, we can write

$$B^u_{H_1}(H) - B^u(H) = 2\int\int_{defg} u_x(\alpha)u_x(-\beta)d\alpha d\beta = 2\int_{H}^{H_{sat}} u_x(\alpha)d\alpha \int_{-H_{sat}}^{H_1} u_x(-\beta)d\beta$$

$$= 2\int_{H}^{H_{sat}} u_x(\alpha)d\alpha \int_{-H_1}^{H_{sat}} u_x(\beta)d\beta = 2F(H)F(-H_1) \qquad (5.23)$$

Equations (5.22) and (5.23) yield

$$B^d_{H_2}(H) = B^d(H) - 2F(H_2)F(-H) \qquad (5.24)$$

$$B^u_{H_1}(H) = B^u(H) + 2F(H)F(-H_1) \qquad (5.25)$$

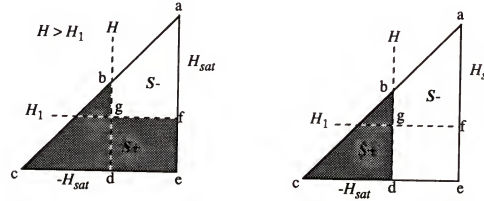

Figure 5.10 Preisach diagrams for deriving $B^u_{H_1}(H)$ - $B^u(H)$.

Since the upward (downward) trajectory of a minor loop is parallel to the corresponding upward (downward) principal trajectory, the trajectory of a minor loop from a reversal point can be obtained by shifting the corresponding principal trajectory to the reversal point. From Fig. 5.9(a), the vertical length(1-5) from a reversal point (H_1, B_1), node 1 in Fig. 5.9(a), to $B^d(H)$ is equal to $B^d(H_1)$-B_1. The upward trajectory $B^u_{H_1, B_1}(H)$ of a minor loop from the reversal point (H_1, B_1) is obtained by shifting down the principal upward trajectory $B^u_{H_1}(H)$ by the vertical length $B^d(H_1)$-B_1, i.e.,

$$\begin{aligned} B^u_{H_1, B_1}(H) &= B^u_{H_1}(H) - B^d(H_1) + B_1 \\ &= B^u(H) + 2F(H)F(-H_1) - B^d(H_1) + B_1 \\ &= -B^d(-H) + 2F(H)F(-H_1) - B^d(H_1) + B_1 \end{aligned} \tag{5.26}$$

for $H > H_1$. The vertical length(2-7) from a reversal point (H_2, B_2), node 2 in Fig. 5.9(a), to $B^u(H)$ is equal to B_2-$B^u(H_2)$. The downward trajectory $B^d_{H_2, B_2}(H)$ of a minor loop from the reversal point (H_2, B_2) is obtained by shifting up the principal downward trajectory $B^d_{H_2}(H)$ by the vertical length B_2-$B^u(H_2)$, i.e.,

$$\begin{aligned} B^d_{H_2, B_2}(H) &= B^d_{H_2}(H) - B^u(H_2) + B_2 \\ &= B^d(H) - 2F(H_2)F(-H) - B^u(H_2) + B_2 \\ &= B^d(H) - 2F(H_2)F(-H) + B^d(-H_2) + B_2 \end{aligned} \tag{5.27}$$

for $H < H_2$. The trajectories of minor loops are thus determined by (5.26) and (5.27), and the only information needed is $B^d(H)$. Note again that $F(H)$ in (5.26) and (5.27) can be obtained from $B^d(H)$ as derived in (5.18) and (5.20). Preisach's theory can also be used to model asymmetrical hysteresis loops, but we need both $B^d(H)$ and $B^u(H)$ to generate the major loop and the minor loops as can be seen from previous derivations.

It was reported [Cha91] that $B^d(H)$ can be modeled as

$$B^d(H) = B_{sat} \frac{H + H_c}{\left| H + H_c \right| + H_c \left(\frac{B_{sat}}{B_r} - 1 \right)} \tag{5.28}$$

In this work, it was found that $B^d(H)$ can be modeled more accurately as

$$B^d(H) = B_{sat}\frac{H + H_c}{|H + H_c| + H_c\left(\frac{B_{sat}}{B_r} - 1\right)\left(1 - \frac{|H|}{H_{sat}}\right)} \tag{5.29}$$

which satisfies the following conditions: a) when $H = -H_c$, $B^d(H) = 0$; b) when $H = 0$, $B^d(H) = B_r$; and c) when $H = \pm H_{sat}$, $B^d(H) = \pm B_{sat}$. Thus, only four parameters H_c, B_r, B_{sat}, and H_{sat} are needed in the model. Note that the magnitude of the magnetic field H should not exceed H_{sat} in using (5.29).

5.3.1.3 Wiping-out property

A general Preisach diagram for minor loops is shown in Fig. 5.11(a), where the interface between *S+* and *S-* is determined by the history and the present state of magnetization. A general hysteresis path (starting from the demagnetized state) for an upward trajectory can be written as [Eve55, Vec80]

$$B(H) = \begin{pmatrix} H_{u_1} & H_{u_2} & \cdots & H_{u_{n-1}} & H_{u_n} & H \\ 0 & H_{l_1} & H_{l_2} & \cdots & H_{l_{n-1}} & H_{l_n} \end{pmatrix} \tag{5.30}$$

where H_{u_i} and H_{l_i}, $i = 1$ to n, denote the n upper turning points and the n lower turning points in the previous history, respectively. The sequence of the turning points shown in (5.30) is H_{u_1}, H_{l_1}, H_{u_2}, H_{l_2}, ..., $H_{u_{n-1}}$, $H_{l_{n-1}}$, H_{u_n}, H_{l_n}. As shown in Fig. 5.11(b), if the current value of H exceeds the previous up-position turning point H_{u_n}, then the previous two turning points H_{l_n} and H_{u_n} will be wiped out (erased). The current value H will be placed in the up-position formerly occupied by H_{u_n}, i.e., using $H_{l_{n-1}}$ instead of H_{l_n} as the previous turning point for calculation, to get the hysteresis path as H increases further. Similarly, a general hysteresis path (starting from the demagnetized state) for a downward trajectory can be written as

$$B(H) = \begin{pmatrix} H_{u_1} & H_{u_2} & \cdots & H_{u_{n-1}} & H_{u_n} \\ 0 & H_{l_1} & H_{l_2} & \cdots & H_{l_{n-1}} & H \end{pmatrix} \tag{5.31}$$

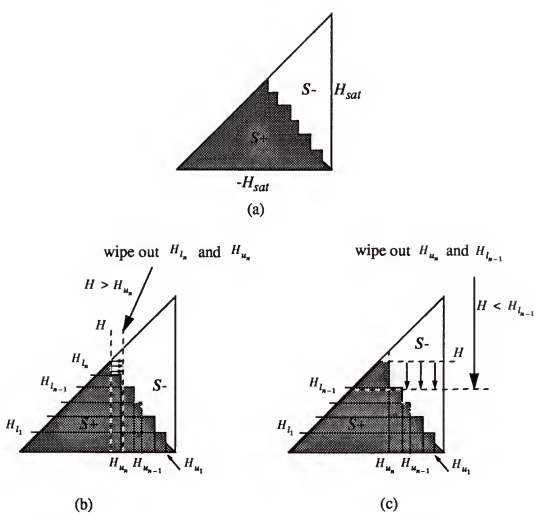

Figure 5.11 A general Preisach diagram for minor loops (a); and Preisach diagrams showing wiping out properties for an ascending curve (b); and for a descending curve (c).

As shown in Fig. 5.11(c), if the current value of H falls below the previous down-position turning point $H_{l_{n-1}}$, then the previous two turning points H_{u_n} and $H_{l_{n-1}}$ will be wiped out. The current value H will be placed in the down-position formerly occupied by $H_{l_{n-1}}$, i.e., using $H_{u_{n-1}}$ instead of H_{u_n} as the previous turning point for calculation, to get the hysteresis path as H decreases further.

Because of the wiping out property discussed above, the turning points (H_1, B_1) or (H_2, B_2) in (5.26) or (5.27) depend on the previous history, i.e., they need to be updated if the wiping out property occurs. Thus, to build the hysteresis model, the previous turning points need to be memorized and updated by monitoring the current magnetic field H.

5.3.1.4 Inclusion of reversible magnetization

Since the classical Preisach model computes only the irreversible component of the magnetization, therefore, a reversible magnetization has to be added to simulate a complete process. Equations (5.26) and (5.27) derived previously for the trajectories of minor loops are only used for computing the irreversible magnetization. To add the reversible magnetization, two approaches are applied in this work. In the first approach, an assumed function which represents the reversible component is added to (5.26) and (5.27), then the parameters for both the irreversible and the reversible components are extracted simultaneously from the experimental data by the Levenberg-Marquardt method [Pre92]. The reversible component can be expressed as

$$B_{rev} = c(B_{an} - B_{irr}) \tag{5.32}$$

since the amount of bending of the domain walls is dependent on the difference between the anhysteretic magnetization and the irreversible magnetization [Jil86]. Note that the notation B instead of M is used in (5.32) for convenience, and B_{an} is expressed as

$$B_{an} = B_{sat}\left[\coth\left(\frac{H + a_1 B}{a_2}\right) - \frac{a_2}{H + a_1 B}\right] \tag{5.33}$$

Thus, we can write

$$B(H) = B_{irr} + B_{rev} = (1-c)B_{irr} + cB_{sat}\left[\coth\left(\frac{H + a_1 B}{a_2}\right) - \frac{a_2}{H + a_1 B}\right] \tag{5.34}$$

where B_{irr} is determined from (5.26) for upward trajectories, and from (5.27) for downward trajectories. $B^d(H)$ in (5.26) and (5.27) now represents the downward limiting curve for the irreversible component only, and is expressed as

$$B^d(H) = \frac{B_{sat,\,irr}(H + H_{c,\,irr})}{\left|H + H_{c,\,irr}\right| + H_{c,\,irr}\left(\frac{B_{sat,\,irr}}{B_{r,\,irr}}\right)\left(1 - \frac{|H|}{H_{sat}}\right)} \tag{5.35}$$

Both B_{sat} and H_{sat} are chosen as constants, and the parameters to be extracted are $H_{c,irr}$, $B_{r,irr}$, $B_{sat,irr}$, c, a_1, and a_2. The notation irr in the subscript denotes that the corresponding term is only for the irreversible magnetization.

In the second approach, (5.26) and (5.27) which represent the irreversible magnetization are modified to include both the irreversible and the reversible components of magnetization. At each (experimental) minor loop with a maximum flux density B_{max}, three parameters H_c, B_r, and B_{sat} in (5.29) are extracted by the Levenberg-Marquardt method; then $H_c(B_{max})$, $B_r(H_{max})$, and $B_{sat}(B_{max})$ are fit by linear or parabolic functions using a linear least-squares method. The parameters to be extracted are the coefficients in the linear or parabolic functions. In this approach, H_{sat} is chosen as a large constant which determines the B_{sat} value, and B_{max} is determined from the flux density at the turning point in the computer simulation. Since B_{max} is difficult to be determined for the initial magnetizing curve, H_c, B_r, and B_{sat} in (5.29) for the initial magnetizing curve are approximately chosen as constants which are the same as those for the major loop.

For both approaches, we extract different sets of parameters at different temperatures, then we model these parameters as piecewise linear functions of temperature using the built-in function *pwl*1 in SABER. The accuracy of the first approach depends on the correctness of the assumed function for the reversible magnetization. Using (5.32), the major loop can be fit well, but the resulting minor loops are less accurate than those from the second approach; nevertheless both approaches produce more accurate results than the classical Preisach model.

5.3.2 Dynamic Model

Since the domain walls can not move as fast as the magnetic field if the changing rate of the magnetic field is above a critical value, the magnetization can not follow the magnetic field immediately. This phenomenon causes a broader hysteresis loop, or a delayed magnetization at higher operating frequencies. This is similar to the non-quasi-static effects of semiconductor devices, which is due to the finite (instead of infinite)

velocity of electron. The delay due to the non-quasi-static effects can be modeled by a low-pass filter as discussed in Chapter 4 for the power IGBT device.

Figure 5.12 shows the circuit models of the low-pass filter with first-order, second-order, and third-order approximations. In the s-domain (with C_i's = 1), we can write

$$\frac{B(s)}{B_{dc}(s)} = \frac{g}{R_1 s + 1} \tag{5.36}$$

for the first-order approximation,

$$\frac{B(s)}{B_{dc}(s)} = \frac{g}{L_1 s^2 + R_1 s + 1} \text{ or } \frac{g}{(R_a s + 1)(R_b s + 1)} \tag{5.37}$$

for the second-order approximation, and

$$\frac{B(s)}{B_{dc}(s)} = \frac{g}{(L_1 s^2 + R_1 s + 1)(R_2 s + 1)} \text{ or } \frac{g}{(R_a s + 1)(R_b s + 1)(R_c s + 1)} \tag{5.38}$$

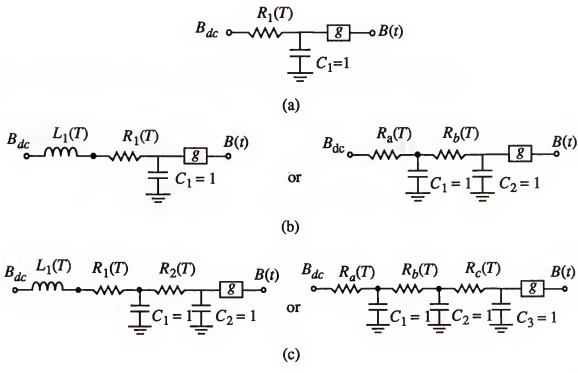

Figure 5.12 Circuit models of the dynamic block $h(t)$ with first-order approximation (a); second-order approximation (b); and third-order approximation (c).

for the third-order approximation. The parameters to be extracted are g and the values of the resistors and inductors. Similar to the static model, the temperature effects are included in the dynamic model by fitting the extracted parameters as piecewise linear functions of temperature using the built-in function *pwl*1 in SABER. Note that the dynamic model discussed in [Jil93] is simply a special case of the present dynamic model using the second-order approximation and $g = 1$. Equation (4) in [Jil93] is rewritten as

$$\frac{1}{\omega_n^2}\frac{d^2}{dt^2}M(t) + \frac{2\lambda}{\omega_n^2}\frac{d}{dt}M(t) + M(t) = M_{dc} \tag{5.39}$$

Comparing with the circuit equation describing the second-order approximation (with $g = 1$),

$$L_1\frac{di}{dt} + R_1 i + \frac{1}{C_1}\int i dt = V \tag{5.40}$$

it can be shown that

$$L_1 \approx \frac{1}{\mu_0\omega_n^2},\ R_1 \approx \frac{2\lambda}{\mu_0\omega_n^2} \tag{5.41}$$

with $C_1 = 1$, $\mu_0 M(t) \approx B(t) \equiv \int i dt$, and $\mu_0 M_{dc} \approx B_{dc} \equiv V$. Thus, the inductor L_1 in the dynamic model is related to the natural frequency ω_n, and the resistor R_1 is related to the damping constant λ and the natural frequency ω_n.

5.4 Parameter Extraction and Implementation

5.4.1 Extraction of Static Model Parameters

Since the hysteresis loops of ferrite materials are almost symmetric, only the experimental data of the downward trajectories of the minor loops are used for parameter extraction. The Levenberg-Marquardt method discussed in Appendix is used to extract the static model parameters.

In the first approach for the modification of the classical Preisach model, the downward trajectory of the major loop or a minor loop from a reversal point (H_2, B_2) can be written as

$$B(H) = (1-c)B_{irr} + cB_{an} = (1-c)[B^d(H) - 2F(H_2)F(-H) + B^d(-H_2) + \tilde{B}_2] + cB_{sat}\left[\coth\left(\frac{H + a_1 B}{a_2}\right) - \frac{a_2}{H + a_1 B}\right] \tag{5.42}$$

where $F(H)$ is defined in (5.18) and (5.20), and $B^d(H)$ is expressed in (5.35). Note that $\tilde{B}_2$ is the irreversible component of the flux density at the magnetic field H_2. For the experimental data obtained from sinusoidal input waveforms, we can approximate $\tilde{B}_2$ by the irreversible component of $B^m(H_2)$, where $B^m(H)$ defined in (5.21), and $B^d(H)$ defined in (5.35) are used. Thus, $\tilde{B}_2$ is also a function of the unknowns $H_{c,\,irr}$, $B_{r,\,irr}$, and $B_{sat,\,irr}$. Although $\tilde{B}_2$ is approximated by $B^m(H_2)$ in the parameter extraction, it is actually determined from the previous turning point in the computer simulation. Since H_{sat} and B_{sat} are chosen as constants which can be determined from the data books, only six parameters ($H_{c,\,irr}$, $B_{r,\,irr}$, $B_{sat,\,irr}$, c, a_1, and a_2) need to be extracted.

To apply the Levenberg-Marquardt method for parameter extraction, we need to find the first-order derivatives of $B(H)$ with respect to the six parameters. Let

$$x_1 \equiv H_{c,\,irr},\ x_2 \equiv B_{sat,\,irr},\ x_3 \equiv B_{r,\,irr}$$

$$v_1 \equiv B^d(H_2),\ v_2 \equiv B^d(-H_2),\ v_3 \equiv B^d(H),\ v_4 \equiv B^d(-H)$$

$$dB_i(H) \equiv \frac{dB^d(H)}{dx_i},\ i = 1, 2, 3 \tag{5.43}$$

the first-order derivatives are derived as

$$\frac{d}{dx_i}B(H) = \left[\frac{1}{4} - \frac{1}{4}\left(\frac{v_2}{v_1}\right)^2 + \frac{1}{2}\left(1 + \frac{v_2}{v_1}\right)\sqrt{\frac{v_3}{v_1}}\right]dB_i(H_2) + \left[\frac{1}{2} + \frac{1}{2}\left(\frac{v_2}{v_1}\right) - \sqrt{\frac{v_3}{v_1}}\right]dB_i(-H_2) + \left[1 - \frac{1}{2}\left(\frac{v_1 + v_2}{\sqrt{v_1 v_3}}\right)\right]dB_i(H),\ i = 1, 2, 3 \text{ for } H \geq 0 \tag{5.44}$$

$$\frac{d}{dx_i}B(H) = \left[\frac{1}{4} - \frac{1}{4}\left(\frac{\nu_2}{\nu_1}\right)^2 - \frac{1}{4}\left(1 - \frac{\nu_2}{\nu_1}\right)\left(\frac{\nu_3 + \nu_4}{\sqrt{\nu_1 \nu_4}}\right)\right] dB_i(H_2)$$
$$+ \left[\frac{1}{2} + \frac{1}{2}\left(\frac{\nu_2}{\nu_1}\right) - \frac{1}{2}\left(\frac{\nu_3 + \nu_4}{\sqrt{\nu_1 \nu_4}}\right)\right] dB_i(-H_2) + \left[1 - \frac{1}{2}\left(\frac{\nu_1 + \nu_2}{\sqrt{\nu_1 \nu_4}}\right)\right] dB_i(H)$$
$$+ \left[\frac{-1}{4}\left(1 - \frac{\nu_3}{\nu_4}\right)\left(\frac{\nu_1 + \nu_2}{\sqrt{\nu_1 \nu_4}}\right)\right] dB_i(-H) \text{ , i = 1, 2, 3 for } H < 0 \tag{5.45}$$

$$\frac{d}{dc}B(H) = B_{sat}\left[\coth\left(\frac{H + a_1 B}{a_2}\right) - \frac{a_2}{H + a_1 B}\right] \tag{5.46}$$

$$\frac{d}{da_1}B(H) = cB_{sat}\left\{\left[1 - \coth^2\left(\frac{H + a_1 B}{a_2}\right)\right]\left(\frac{B}{a_2}\right) + \frac{a_2 B}{(H + a_1 B)^2}\right\} \tag{5.47}$$

$$\frac{d}{da_2}B(H) = cB_{sat}\left\{\left[1 - \coth^2\left(\frac{H + a_1 B}{a_2}\right)\right]\left(\frac{-H - a_1 B}{a_2^2}\right) - \frac{1}{(H + a_1 B)}\right\} \tag{5.48}$$

where

$$dB_1(H) = \frac{B_{sat,\,irr} H\left[1 - \frac{B_{sat,\,irr}}{B_{r,\,irr}}\left(1 - \frac{|H|}{H_{sat}}\right) - \frac{|H|}{H_{sat}}\right]}{\left\{W + H_{c,\,irr}\left[\frac{B_{sat,\,irr}}{B_{r,\,irr}}\left(1 - \frac{|H|}{H_{sat}}\right) + \frac{|H|}{H_{sat}}\right]\right\}^2} \tag{5.49}$$

$$dB_2(H) = \frac{(H + H_{c,\,irr})\left(W + H_{c,\,irr}\frac{|H|}{H_{sat}}\right)}{\left\{W + H_{c,\,irr}\left[\frac{B_{sat,\,irr}}{B_{r,\,irr}}\left(1 - \frac{|H|}{H_{sat}}\right) + \frac{|H|}{H_{sat}}\right]\right\}^2} \tag{5.50}$$

$$dB_3(H) = \frac{\left(\frac{B_{sat,\,irr}}{B_{r,\,irr}}\right)^2 H_{c,\,irr}(H + H_{c,\,irr})\left(1 - \frac{|H|}{H_{sat}}\right)}{\left\{W + H_{c,\,irr}\left[\frac{B_{sat,\,irr}}{B_{r,\,irr}}\left(1 - \frac{|H|}{H_{sat}}\right) + \frac{|H|}{H_{sat}}\right]\right\}^2} \tag{5.51}$$

where $W = H$ for $H \geq -H_{c,\,irr}$, and $W = -H - 2H_{c,\,irr}$ for $H \leq -H_{c,\,irr}$.

For the second approach, the downward trajectory of the major loop or a minor loop can be written as

$$B(H) = B^d(H) - 2F(H_2)F(-H) + B^d(-H_2) + B_2 \tag{5.52}$$

where $B^d(H)$ is expressed in (5.29), and B_2 in (5.52) is a constant for each minor loop. Using similar notations as defined in (5.43) and neglecting *irr* in the subscript, the first-order derivatives of $B(H)$ with respect to H_c, B_{sat}, and B_r are derived as

$$\frac{d}{dx_i}B(H) = \left[\frac{1}{2}\left(1+\frac{v_2}{v_1}\right)\sqrt{\frac{v_3}{v_1}}\right]dB_i(H_2) + \left[1-\sqrt{\frac{v_3}{v_1}}\right]dB_i(-H_2)$$

$$+\left[1-\frac{1}{2}\left(\frac{v_1+v_2}{\sqrt{v_1 v_3}}\right)\right]dB_i(H)\,,\ i=1,2,3 \text{ for } H \geq 0 \tag{5.53}$$

$$\frac{d}{dx_i}B(H) = \left[-\frac{1}{4}\left(1-\frac{v_2}{v_1}\right)\left(\frac{v_3+v_4}{\sqrt{v_1 v_4}}\right)\right]dB_i(H_2) + \left[1-\frac{1}{2}\left(\frac{v_3+v_4}{\sqrt{v_1 v_4}}\right)\right]dB_i(-H_2)$$

$$+\left[1-\frac{1}{2}\left(\frac{v_1+v_2}{\sqrt{v_1 v_4}}\right)\right]dB_i(H) + \left[\frac{-1}{4}\left(1-\frac{v_3}{v_4}\right)\left(\frac{v_1+v_2}{\sqrt{v_1 v_4}}\right)\right]dB_i(-H)\,,\ i=1,2,3 \text{ for } H<0 \tag{5.54}$$

where $dB_i(H)$, i = 1, 2, 3, are defined in (5.49) - (5.51) by neglecting the notation *irr*. At each (experimental) minor loop with maximum flux density B_{max}, three parameters H_c, B_r, and B_{sat} in (5.29) are extracted, then $H_c(B_{max})$, $B_r(B_{max})$ and $B_{sat}(B_{max})$ are fit as linear or parabolic functions of B_{max}. The parameters in the static model are the coefficients in the linear or parabolic functions. For higher accuracies, higher-order functions can be used.

5.4.2 Extraction of Dynamic Model Parameters

We will use the second-order approximation, (5.37), to illustrate the procedure for extracting the dynamic model parameters. Using a bilinear transformation,

$$s = \frac{2}{T}\left(\frac{1-z^{-1}}{1+z^{-1}}\right) \tag{5.55}$$

(5.37) can be transformed from the s-domain to the z-domain as

$$\frac{B(z)}{B_{dc}(z)} = \frac{g(1+2z^{-1}+z^{-2})}{L_1\left[\frac{4}{T^2}(1-2z^{-1}+z^{-2})\right]+R_1\left[\frac{2}{T}(1-z^{-2})\right]+(1+2z^{-1}+z^{-2})} \tag{5.56}$$

where T is the sampling time. From $B(z) \to B(n)$, $z^{-1}B(z) \to B(n-1)$, and $z^{-2}B(z) \to B(n-2)$, a difference equation can be derived from (5.56) as

$$L_1\left[\frac{4}{T^2}(B(n)-2B(n-1)+B(n-2))\right]+R_1\left[\frac{2}{T}(B(n)-B(n-2))\right]$$
$$+\,g[-B_{dc}(n)-2B_{dc}(n-1)-B_{dc}(n-2)] = -B(n)-2B(n-1)-B(n-2) \tag{5.57}$$

The sequence $B(n)$ is acquired by the LabWindows software at a constant sampling time T from high-frequency experiments; while the sequence $B_{dc}(n)$ is calculated from the modified Preisach model implemented in SABER using a fixed time-step T. For N data points in the $B(n)$ and $B_{dc}(n)$ sequences, (5.57) can be written in a matrix form as

$$\boldsymbol{XR} = \boldsymbol{Y} \tag{5.58}$$

where $\boldsymbol{R} = [L_1\ R_1\ g]^T$, $\boldsymbol{Y} = [-B(3)\text{-}2B(2)\text{-}B(1)\ \ldots\ -B(N)\text{-}2B(N\text{-}1)\text{-}B(N\text{-}2)]^T$, and

$$\boldsymbol{X}(i,1) = \frac{4}{T^2}[B(i+2)-2B(i+1)+B(i)]$$

$$\boldsymbol{X}(i,2) = \frac{2}{T}[B(i+2)-B(i)]$$

$$\boldsymbol{X}(i,3) = -B_{dc}(i+2)-2B_{dc}(i+1)-B_{dc}(i),\ i = 1 \text{ to } N\text{-}2 \tag{5.59}$$

The coefficient vector $\boldsymbol{R}$ can be readily computed from (5.58) as

$$\boldsymbol{R} = [\boldsymbol{X}^T\boldsymbol{X}]^{-1}\boldsymbol{X}^T\boldsymbol{Y} \tag{5.60}$$

in the sense of least-squares estimation.

At different temperatures, we extract different sets of static and dynamic model parameters; then we model these parameters as piecewise linear functions of temperature using the built-in function *pwl*1 in SABER.

5.4.3 Implementation

As an example to illustrate the implementation, the proposed hysteresis model is incorporated into a transformer model implemented in SABER. Because of the wiping-out property, the previous turning (reversal) points in the Preisach diagram need to be memorized and compared with the current magnetic field H. Since the values of analog variables in SABER are not retained from one time to another, we need to use analog state variables to model (memorize) the turning points. An analog state is an event-driven signal (like the digital signal) that has any valid analog value (like the analog signal), but it is handled by the digital simulator. As in a digital state, the value of an analog state variable will be retained until updated by an event.

The electrical symbol of a (two-winding) transformer and its schematic structure are shown in Fig, 5.13. From the Ampere's law,

$$\oint H \bullet dl = \oint J \bullet dS \tag{5.61}$$

we can write

$$H_m l_m + H_{air} l_{air} = k_p N_p I_p + k_s N_s I_s \tag{5.62}$$

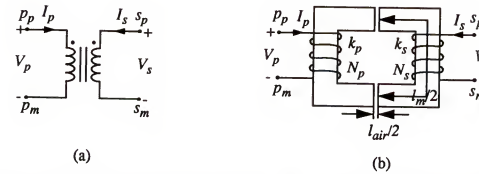

Figure 5.13 The electrical symbol of a transformer (a); and its schematic structure (b);

where H_m is the magnetic field inside the magnetic (ferrite) material, l_m the magnetic flux path inside the magnetic material, H_{air} the magnetic field inside the air-gap, l_{air} the length of the air-gap, k_p the coupling factor of the primary winding to the core, k_s the coupling factor of the secondary winding to the core, N_p the number of the primary winding, N_s the number of the secondary winding, I_p the primary current, and I_s the secondary current. Since the magnetic flux density inside the ferrite is the same as that inside the air-gap, i.e., $B_m = B_{air}$, and $H_{air} = B_{air}/\mu_0$, (5.62) can be written as

$$H_m l_m + \frac{B_m l_{air}}{\mu_0} = k_p N_p I_p + k_s N_s I_s \tag{5.63}$$

The primary and secondary voltages of the transformer are expressed as

$$V_p = N_p \frac{d\phi_m}{dt} + L_{ep}\frac{dI_p}{dt} = N_p \frac{d}{dt}(B_m S_c) + L_{ep}\frac{dI_p}{dt} \tag{5.64}$$

$$V_s = N_s \frac{d\phi_m}{dt} + L_{es}\frac{dI_s}{dt} = N_s \frac{d}{dt}(B_m S_c) + L_{es}\frac{dI_s}{dt} \tag{5.65}$$

where ϕ_m is the magnetic flux, S_c the cross-section area, L_{ep} the primary leakage inductor, and L_{es} the secondary leakage inductor. Equations (5.63) - (5.65) and the equivalent circuit model for the low-pass filter are written in the "equations" section of the nonlinear transformer template in SABER. The modified Preisach model is implemented in the "when" and "values" sections of the nonlinear transformer template.

5.5 Verification

A toroid made of Philips 3C85 material is used for measuring the experimental BH hysteresis loops at different operating frequencies and temperatures. The tested core part number is 768T188 with outer diameter OD = $1.27\text{x}10^{-2}$ m, inner diameter ID = $7.14\text{x}10^{-3}$ m, thickness = $4.78\text{x}10^{-3}$ m, magnetic path length $l_m = 2.95\text{x}10^{-2}$ m, and cross-section area $S_c = 1.28\text{x}10^{-5}$ m^2. A transformer with 18 turns of the primary and secondary windings

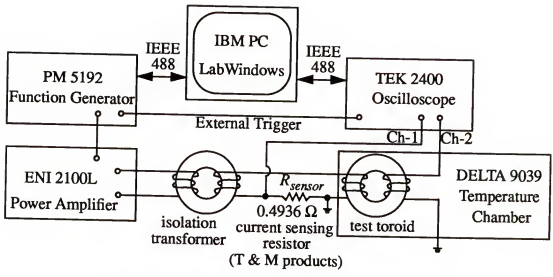

Figure 5.14 Experimental setup for the core-loss or BH-loop measurements.

wound in a bifilar fashion is used. The core-loss measurement setup shown in Fig. 5.14 is used to obtain the BH data acquired by the LabWindows software. The operating temperature is controlled by a DELTA 9039 temperature chamber. To ensure that the pre-set temperature in the chamber is the real temperature inside the material, the exciting voltage is not applied until the temperature inside the chamber becomes steady, and the period of the excitation voltage is controlled to only several cycles of the operating frequency to avoid the temperature rise inside the core. The magnetic field H is calculated from the measured current flowing in the current sensing resistor, i.e.,

$$H = \frac{n_1 I_{sensor}}{l_m} = \frac{n_1 V_1}{R_{sensor} l_m} \tag{5.66}$$

and the magnetic flux density B is numerically integrated from the measured secondary voltage V_2 (after an offset voltage correction) using the following relation:

$$B = \frac{1}{n_2 S_c} \int_0^t V_2 dt \tag{5.67}$$

Since the minimum available frequency provided by the ENI 2100L power amplifier is 10kHz, the static model parameters are extracted from the experimental data at

f = 10kHz, i.e., at the quasi-static condition. This is a good approximation, because it was found that all the hysteresis loops obtained at operating frequencies below 20kHz for the 3C85 material are almost identical and close to the static loop. To verify the proposed model, the second approach for modifying the classical Preisach model is used in the simulation. It was also found that the first-order and second-order approximations in the dynamic block give similar simulation results for the 3C85 material, because the higher pole is much larger than the lower pole in the second-order approximation; thus, only the first-order approximation in the dynamic block is used. The second-order and third-order approximations, however, may be useful for other magnetic materials working at higher operating frequencies. The simulated hysteresis loops generated by the proposed hysteresis model are compared with the experimental hysteresis loops in Fig. 5.15 for T = 25°C and f = 10kHz, in Fig. 16 for T = 90°C and f = 10kHz, in Fig. 5.17 for T = 25°C and f = 300kHz, in Fig. 5.18 for T = 50°C and f = 300kHz, and in Fig. 5.19 for T = 70°C and f = 500kHz. Both the simulated and the experimental major loops at two different operating temperatures (T = 25°C and T = 100°C) and f = 10kHz are shown in Fig. 5.20, which is similar to the plot shown in the data book. The satisfactory agreements between the simulated and the experimental results at different combinations of operating frequencies and temperatures validate the proposed rate-dependent and temperature-dependent hysteresis model.

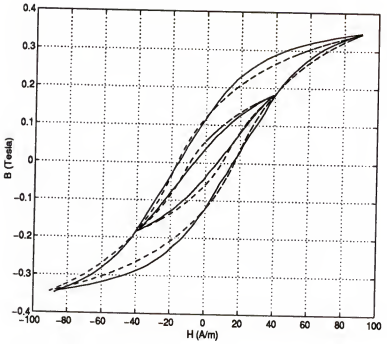

Figure 5.15 The experimental and simulated BH hysteresis loops at $T = 25^{o}$C and $f =$ 10kHz; solid lines: experimental results; dashed lines: simulated results

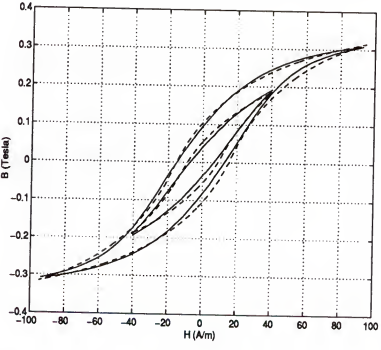

Figure 5.16 The experimental and simulated BH hysteresis loops at $T = 90^{o}$C and $f =$ 10kHz; solid lines: experimental results; dashed lines: simulated results.

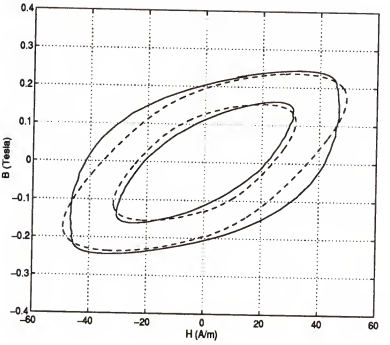

Figure 5.17 The experimental and simulated BH hysteresis loops at $T = 25^{o}$C and $f =$ 300kHz; solid lines: experimental results; dashed lines: simulated results.

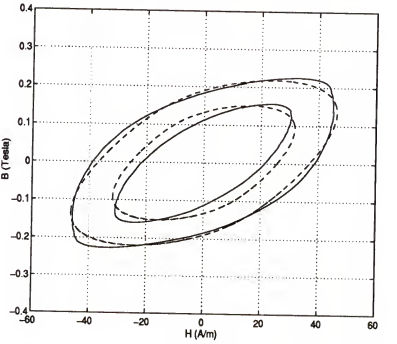

Figure 5.18 The experimental and simulated BH hysteresis loops at $T = 50^{o}$C and $f =$ 300kHz; solid lines: experimental results; dashed lines: simulated results.

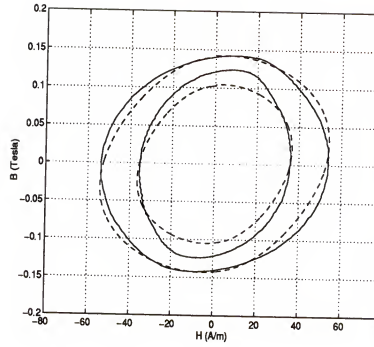

Figure 5.19 The experimental and simulated BH hysteresis loops at $T = 70^{o}$C and $f =$ 500kHz; solid lines: experimental results; dashed lines: simulated results.

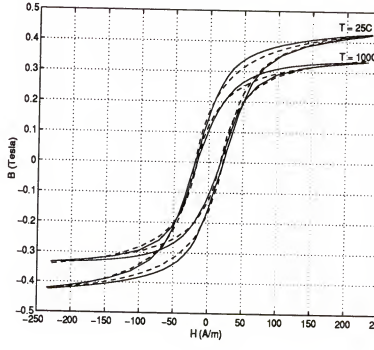

Figure 5.20 The experimental and simulated major loops at $T = 25^{o}$C and $T = 100^{o}$C ($f =$ 10kHz); solid lines: experimental results; dashed lines: simulated results.

5.6 Summary

A rate-dependent and temperature-dependent hysteresis model, which consists of both the irreversible and the reversible components of magnetization, has been presented. The proposed model structure provides an efficient way to incorporate the rate-dependent and temperature-dependent effects of the hysteresis phenomena into the classical Preisach model. To modify the classical Preisach model, two approaches have been discussed to include the reversible magnetization. The proposed hysteresis model gives satisfactory simulation results, and can be applied for magneto-thermal simulation.

CHAPTER 6
FIELD-BASED FINITE-ELEMENT CIRCUIT MODELS FOR MAGNETIC COMPONENTS WITH HYSTERESIS

6.1 Introduction

Along with the trend to increase the operating frequency and the use of low-profile cores and planar windings, there has been a renewed interest in employing field simulators [Han95] and coupled field/circuit simulation [Tsu93] for modeling of magnetic components. These field-based approaches are able to deal with geometry, frequency, large-signal, and waveshape effects, which have been found difficult to predict using conventional 1-D, low-frequency magnetic models. Field-based models are also "predictive," i.e., they can be synthesized with adequate degree of accuracy before the component is fabricated and measured, thus potentially reducing manufacturing cost.

This chapter describes a finite-element formulation for the development of field-based, geometry-dependent circuit models which enable coupled field/circuit simulation of circuits containing magnetic components with hysteresis. SABER templates are developed for the 2-D field-equivalent subcircuits representing the dynamic electromagnetic fields in the magnetic (ferrite), conductive (copper), and insulating elements, as well as for an interface network. SABER templates of equivalent subcircuits for the boundary infinite-elements [Zie83, Coo89] are also developed to account for the boundary condition at infinity. Hysteresis models such as the Jiles-Atherton model, the Preisach model, and the rate-dependent and temperature-dependent hysteresis model discussed in Chapter 5, are incorporated into the finite-element formulation of the ferrite model. Transient electromagnetic and circuit phenomena within and outside the magnetic components can be simulated simultaneously for a wide range of circuit topologies and excitation waveforms, using existing circuit simulators. The advantages of the Finite-Element

formulation described in this chapter over the Finite Difference approach [Per95, Ram95] are: a) conservation laws are exactly satisfied even by coarse approximations; b) meshings for irregular geometries are readily adaptive; and c) high-order approximations are more readily constructed. In addition, Finite-Difference method can be shown to be a special case of Finite-Element method.

Field-based finite-element circuit models have been reported [Tsu93, Dem92], but these models relied on mutual capacitors, mutual inductors, and mutual resistors, and no hysteresis model was included. In this work, a rational approach, discussed in Chapter 2, to construct circuit networks that do not use mutual capacitors/inductors/resistors is applied to derive field-based finite-element circuit models.

The inclusion of hysteresis in the finite-element analysis was discussed in Vecchio [Vec82] and Delince et al. [Del94]. This chapter will present an alternative finite-element formulation for hysteresis (including minor loops) which is easier to couple with circuit equations and is based on the conventional constitutive laws.

The fundamentals of finite-element method are reviewed in Section 6.2. The elemental field-equivalent subcircuits are derived in Section 6.3. The modeling methodology for the overall field-based circuit model is illustrated in Section 6.4, and verified in Section 6.5.

6.2 Fundamentals of Finite Element Method

The key words for the Galerkin finite-element method are trial solution, weighted residual method, Galerkin approximation, and fundamental lemma of calculus of variation (FLCV). The fundamentals of finite-element method will be illustrated by the derivation of the semi-discrete equations resulting from a discretization of the Maxwell's equations. The 2-D linear triangular finite-element and the boundary infinite-element are reviewed, and the resemblance between magnetic and circuit systems is discussed.

6.2.1 Derivation of Semidiscrete Equations

The physics-based magnetic circuit models are constructed from the semi-discrete equations derived from a discretization (in space) of the Maxwell's equations by finite-element method. A partial subset of Maxwell's equations is written as

$$\nabla \bullet \boldsymbol{B} = 0 \tag{6.1}$$

$$\nabla \times \boldsymbol{E} = -\dot{\boldsymbol{B}} \tag{6.2}$$

$$\nabla \times \boldsymbol{H} = \boldsymbol{J} = \boldsymbol{J}_{cond} + \dot{\boldsymbol{D}} \tag{6.3}$$

where $\boldsymbol{B}$ is the magnetic flux density, $\boldsymbol{H}$ the magnetic field strength, $\boldsymbol{E}$ the electric field strength, $\boldsymbol{D}$ the displacement, $\boldsymbol{J}$ the current density, $\boldsymbol{J}_{cond}$ the conduction current density, $\dot{\boldsymbol{B}}$ and $\dot{\boldsymbol{D}}$ are the time derivatives of $\boldsymbol{B}$ and $\boldsymbol{D}$, respectively, and $\dot{\boldsymbol{D}}$ is the displacement current density due to time-varying electric fields. The potential definitions are written as

$$\boldsymbol{B} = \nabla \times \boldsymbol{A} \tag{6.4}$$

$$\boldsymbol{E} = -\nabla \phi - \dot{\boldsymbol{A}} \tag{6.5}$$

where $\boldsymbol{A}$ is the magnetic vector potential, ϕ the electric scalar potential, and $\dot{\boldsymbol{A}}$ the time derivative of $\boldsymbol{A}$. Equation (6.4) is derived from (6.1) and the fact that the divergence of the curl operator is zero, and (6.5) is derived from (6.2), (6.4) and the fact that the curl of a gradient is zero. Using the time integral of electric scalar potential ψ, with $\phi = \dot{\psi}$ [Mac90], (6.5) can be expressed as

$$\boldsymbol{E} = -\nabla \dot{\psi} - \dot{\boldsymbol{A}} \tag{6.6}$$

The constitutive laws of the material properties are expressed as

$$\boldsymbol{J}_{cond} = \sigma \boldsymbol{E}, \; \boldsymbol{D} = \varepsilon \boldsymbol{E} \tag{6.7}$$

$$\boldsymbol{H} = \nu \boldsymbol{B} \text{ (for linear problems), and } \boldsymbol{B} = \mu_0(\boldsymbol{H} + \boldsymbol{M}) \text{ (for nonlinear problems)} \tag{6.8}$$

where σ is the conductivity, ε the dielectric permittivity, ν the reluctivity, μ_0 $(= 1/\nu_0)$ the

permeability in the free space, and $\boldsymbol{M}$ is the magnetization.

From (6.3) - (6.8), the governing equation of the electromagnetic system is derived as

$$\nabla\times(\nu\nabla\times\boldsymbol{A}) + \sigma(\nabla\dot{\psi} + \dot{\boldsymbol{A}}) + \varepsilon(\nabla\ddot{\psi} + \ddot{\boldsymbol{A}}) = 0 \text{ for linear problems} \tag{6.9}$$

or

$$\nabla\times(\nu_0\nabla\times\boldsymbol{A}) + \sigma(\nabla\dot{\psi} + \dot{\boldsymbol{A}}) + \varepsilon(\nabla\ddot{\psi} + \ddot{\boldsymbol{A}}) = \nabla\times\boldsymbol{M} \text{ for nonlinear problems} \tag{6.10}$$

with the initial condition

$$\boldsymbol{A} = 0 \text{ at } t = 0 \tag{6.11}$$

the homogeneous Neumann boundary condition [Sal90]

$$\nabla\boldsymbol{A}\bullet\boldsymbol{n} = \frac{\partial\boldsymbol{A}}{\partial\boldsymbol{n}} = 0 \text{ on } \partial\Omega \tag{6.12}$$

the Dirichlet boundary condition

$$\boldsymbol{A} = 0 \text{ at infinity} \tag{6.13}$$

and the boundary conditions for $\nabla\psi$, which are determined by the external circuitry. $\boldsymbol{n}$ is the outward normal vector to the boundary $\partial\Omega$. The electromagnetic system is coupled with the circuit system through $\boldsymbol{J}$ $(= \sigma(-\nabla\dot{\psi} - \dot{\boldsymbol{A}}) + \varepsilon(-\nabla\ddot{\psi} - \ddot{\boldsymbol{A}}))$ which is provided by

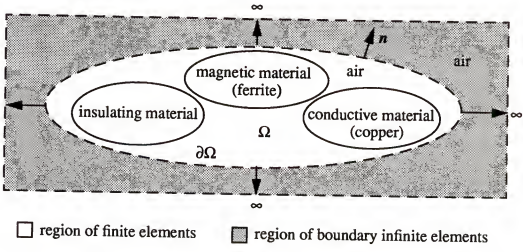

Figure 6.1 Mathematical domain of the electromagnetic system.

the external circuitry.

For the 2D electromagnetic problems, $\boldsymbol{A}$, $\boldsymbol{J}$ and $\boldsymbol{E}$ are z-directed and independent of z, and $-\nabla\phi = -\nabla\dot{\psi} = \Delta V / l_z$, where l_z is the (thickness) length of the 2D problem, and ΔV is the voltage difference in the z-direction. To ensure the uniqueness of the solutions, the Coulomb gauge $\nabla\bullet\boldsymbol{A} = 0$ is used. From

$$\nabla\times\nabla\times\boldsymbol{A} = \nabla(\nabla\bullet\boldsymbol{A}) - \nabla^2\boldsymbol{A} = -\nabla^2\boldsymbol{A} \tag{6.14}$$

(6.9) and (6.10) can be written as

$$\varepsilon\dot{\boldsymbol{A}} + \varepsilon\nabla\dot{\psi} + \sigma\boldsymbol{A} + \sigma\nabla\psi - \nu\nabla^2\boldsymbol{A} = 0 \text{ for linear problems} \tag{6.15}$$

$$\varepsilon\dot{\boldsymbol{A}} + \varepsilon\nabla\dot{\psi} + \sigma\boldsymbol{A} + \sigma\nabla\psi - \nu_0\nabla^2\boldsymbol{A} = \nabla\times\boldsymbol{M} \text{ for nonlinear problems} \tag{6.16}$$

The first step of applying Galerkin finite element method is to use trial solutions $\boldsymbol{A}_T$ and $\boldsymbol{u}_T$ to approximate $\boldsymbol{A}$ and $-\nabla\psi$, respectively; and the trial solutions are assumed to satisfy the boundary conditions. Note that $\boldsymbol{u}_T$ can also be chosen to approximate ψ, $\nabla\psi$ or $\nabla\dot{\psi}$, which will change the formulation slightly. Since the trial solutions may not exactly equal the exact solutions, a residue $\boldsymbol{r}$ will exist if replacing $\boldsymbol{A}$ and $-\nabla\psi$ by $\boldsymbol{A}_T$ and $\boldsymbol{u}_T$ in (6.15) and (6.16), i.e.,

$$\boldsymbol{r} = \varepsilon\dot{\boldsymbol{A}}_T - \varepsilon\dot{\boldsymbol{u}}_T + \sigma\boldsymbol{A}_T - \sigma\boldsymbol{u}_T - \nu\nabla^2\boldsymbol{A}_T \text{ for linear problems} \tag{6.17}$$

$$\boldsymbol{r} = \varepsilon\dot{\boldsymbol{A}}_T - \varepsilon\dot{\boldsymbol{u}}_T + \sigma\boldsymbol{A}_T - \sigma\boldsymbol{u}_T - \nu_0\nabla^2\boldsymbol{A}_T - \nabla\times\boldsymbol{M} \text{ for nonlinear problems} \tag{6.18}$$

Based on weighted residual method, Galerkin approximation, and FLCV, a set of semi-discrete equations which ensure $\boldsymbol{r} = 0$ in an approximated (weak) form can be constructed from (6.17) and (6.18) as follows. Multiplying (6.17) and (6.18) by a weighted function $\boldsymbol{w}$, then integrating over the domain Ω, we can write

$$\int_{\Omega} w r d\Omega = \varepsilon \int_{\Omega} w \dot{A}_T d\Omega - \varepsilon \int_{\Omega} w \dot{u}_T d\Omega$$

$$+ \sigma \int_{\Omega} w \dot{A}_T d\Omega - \sigma \int_{\Omega} w \dot{u}_T d\Omega - \nu \int_{\Omega} w(\nabla^2 A_T) d\Omega \tag{6.19}$$

for linear problems, and

$$\int_{\Omega} w r d\Omega = \varepsilon \int_{\Omega} w \dot{A}_T d\Omega - \varepsilon \int_{\Omega} w \dot{u}_T d\Omega + \sigma \int_{\Omega} w \dot{A}_T d\Omega - \sigma \int_{\Omega} w \dot{u}_T d\Omega$$

$$- \nu_0 \int_{\Omega} w(\nabla^2 A_T) d\Omega - \int_{\Omega} w(\nabla \times M) d\Omega \tag{6.20}$$

for nonlinear problems. The term including $\nabla^2 A_T$ in (6.19) and (6.20) can be written as

$$\int_{\Omega} w(\nabla^2 A_T) d\Omega = \int_{\Omega} \nabla \bullet (w \nabla A_T) d\Omega - \int_{\Omega} \nabla w \bullet \nabla A_T d\Omega \tag{6.21}$$

From the homogeneous Neumann boundary condition, we can obtain

$$\int_{\Omega} \nabla \bullet (w \nabla A_T) d\Omega = \int_{\partial\Omega} w \nabla A_T \bullet n d(\partial\Omega) = 0 \tag{6.22}$$

which gives

$$\int_{\Omega} w(\nabla^2 A_T) d\Omega = -\int_{\Omega} \nabla w \bullet \nabla A_T d\Omega = -\int_{\Omega} \text{grad} w \bullet \text{grad} A_T \, d\Omega \tag{6.23}$$

From the (Bubnov-)Galerkin approximation, the weighted function w, and the trial solutions A_T and u_T are approximated in a finite-dimensional subspace as

$$w(x, y) \approx w^h(x, y) = \sum_{i=1}^{n} c_i N_i(x, y) \tag{6.24}$$

$$A_T(x, y, t) \approx A^h(x, y, t) = \sum_{i=1}^{n} a_i(t) N_i(x, y) \tag{6.25}$$

$$u_T(x, y, t) \approx u^h(x, y, t) = \sum_{i=1}^{n} u_i(t) N_i(x, y) \tag{6.26}$$

where N_i's are the basis functions. Substitution of (6.23) - (6.26) into (6.19) and (6.20) yields

$$\int_\Omega w^h r d\Omega = \varepsilon \int_\Omega w^h \dot{\dot{A}}^h d\Omega - \varepsilon \int_\Omega w^h \dot{\dot{u}}^h d\Omega + \sigma \int_\Omega w^h \dot{A}^h d\Omega$$

$$-\sigma \int_\Omega w^h \dot{u}^h d\Omega + \nu \int_\Omega \text{grad} w^h \bullet \text{grad} A^h \, d\Omega \text{ for linear problems} \qquad (6.27)$$

$$\int_\Omega w^h r d\Omega = \varepsilon \int_\Omega w^h \dot{\dot{A}}^h d\Omega - \varepsilon \int_\Omega w^h \dot{\dot{u}}^h d\Omega + \sigma \int_\Omega w^h \dot{A}^h d\Omega - \sigma \int_\Omega w^h \dot{u}^h \Omega$$

$$+ \nu_0 \int_\Omega \text{grad} w^h \bullet \text{grad} A^h \, d\Omega - \int_\Omega w^h (\nabla \times M) d\Omega \text{ for nonlinear problems} \qquad (6.28)$$

The fundamental lemma of calculus of variation (FLCV) is stated as follows:

> Consider a function $r(x)$: [a, b] $\rightarrow \Re$ continuous such that $\int_a^b w(x) r(x) dx = 0$ for every $w(x)$ continuous on [a, b], (and $w(a) = w(b) = 0$), then $r(x) \equiv 0$.

If $\int_\Omega w^h r d\Omega = 0$ is satisfied for $w^h(x, y) = N_i(x, y)$, $i = 1$ to n, then we can conclude that $r \equiv 0$ from FLCV since every function in the subspace is a linear combination of the basis functions. Thus, we can write

$$\sum_{j=1}^{n} \dot{\dot{a}}_j \int_\Omega \varepsilon N_i N_j d\Omega - \sum_{j=1}^{n} \dot{\dot{u}}_j \int_\Omega \varepsilon N_i N_j d\Omega + \sum_{j=1}^{n} \dot{a}_j \int_\Omega \sigma N_i N_j d\Omega - \sum_{j=1}^{n} \dot{u}_j \int_\Omega \sigma N_i N_j d\Omega$$

$$+ \sum_{j=1}^{n} a_j \int_\Omega \nu (\text{grad} N_i \bullet \text{grad} N_j) \, d\Omega = 0, \, i = 1 \text{ to } n \qquad (6.29)$$

for linear problems, and

$$\sum_{j=1}^{n} \dot{\dot{a}}_j \int_\Omega \varepsilon N_i N_j d\Omega - \sum_{j=1}^{n} \dot{\dot{u}}_j \int_\Omega \varepsilon N_i N_j d\Omega + \sum_{j=1}^{n} \dot{a}_j \int_\Omega \sigma N_i N_j d\Omega - \sum_{j=1}^{n} \dot{u}_j \int_\Omega \sigma N_i N_j d\Omega$$

$$+ \sum_{j=1}^{n} a_j \int_{\Omega} \nu_0 (\text{grad} N_i \bullet \text{grad} N_j)\, d\Omega = \int_{\Omega} N_i (\nabla \times \boldsymbol{M}) d\Omega, \; i = 1 \text{ to } n \tag{6.30}$$

for nonlinear problems. Equations (6.29) and (6.30) can be rewritten in matrix forms as

$$\boldsymbol{M}_{AA}\ddot{\boldsymbol{a}} + \boldsymbol{M}_{A\psi}\ddot{\boldsymbol{u}} + \boldsymbol{B}_{AA}\dot{\boldsymbol{a}} + \boldsymbol{B}_{A\psi}\dot{\boldsymbol{u}} + \boldsymbol{K}_{AA}^{lin}\boldsymbol{a} = 0 \text{ for linear problems} \tag{6.31}$$

$$\boldsymbol{M}_{AA}\ddot{\boldsymbol{a}} + \boldsymbol{M}_{A\psi}\ddot{\boldsymbol{u}} + \boldsymbol{B}_{AA}\dot{\boldsymbol{a}} + \boldsymbol{B}_{A\psi}\dot{\boldsymbol{u}} + \boldsymbol{K}_{AA}^{nl}\boldsymbol{a} = \boldsymbol{I}_M \text{ for nonlinear problems} \tag{6.32}$$

where $\boldsymbol{a}$ is the vector of nodal magnetic vector potentials a_i's, and $\boldsymbol{u}$ is the vector of u_i's $= -\nabla\psi_i$'s, where ψ_i is the time integral of the electric scalar potential at node i. The vector $\boldsymbol{I}_M$ has only nonzero terms at the nodes inside the magnetic (ferrite) materials. From

$$\boldsymbol{J} = \boldsymbol{J}_{cond} + \dot{\boldsymbol{D}} = \sigma(-\nabla\dot{\psi} - \dot{\boldsymbol{A}}) + \varepsilon(-\nabla\ddot{\psi} - \ddot{\boldsymbol{A}}) \tag{6.33}$$

we can also derive

$$\boldsymbol{M}_{A\psi}^{T}\ddot{\boldsymbol{a}} + \boldsymbol{M}_{\psi\psi}\ddot{\boldsymbol{u}} + \boldsymbol{B}_{A\psi}^{T}\dot{\boldsymbol{a}} + \boldsymbol{B}_{\psi\psi}\dot{\boldsymbol{u}} = \boldsymbol{I} \tag{6.34}$$

Combining (6.31) and (6.34) yields

$$\begin{bmatrix} \boldsymbol{M}_{AA} & \boldsymbol{M}_{A\psi} \\ \boldsymbol{M}_{A\psi}^{T} & \boldsymbol{M}_{\psi\psi} \end{bmatrix} \begin{bmatrix} \ddot{\boldsymbol{a}} \\ \ddot{\boldsymbol{u}} \end{bmatrix} + \begin{bmatrix} \boldsymbol{B}_{AA} & \boldsymbol{B}_{A\psi} \\ \boldsymbol{B}_{A\psi}^{T} & \boldsymbol{B}_{\psi\psi} \end{bmatrix} \begin{bmatrix} \dot{\boldsymbol{a}} \\ \dot{\boldsymbol{u}} \end{bmatrix} + \begin{bmatrix} \boldsymbol{K}_{AA}^{lin} & \boldsymbol{0} \\ \boldsymbol{0} & \boldsymbol{0} \end{bmatrix} \begin{bmatrix} \boldsymbol{a} \\ \boldsymbol{u} \end{bmatrix} = \begin{bmatrix} \boldsymbol{0} \\ \boldsymbol{I} \end{bmatrix} \tag{6.35}$$

for linear problems, and combining (6.32) and (6.34) yields

$$\begin{bmatrix} \boldsymbol{M}_{AA} & \boldsymbol{M}_{A\psi} \\ \boldsymbol{M}_{A\psi}^{T} & \boldsymbol{M}_{\psi\psi} \end{bmatrix} \begin{bmatrix} \ddot{\boldsymbol{a}} \\ \ddot{\boldsymbol{u}} \end{bmatrix} + \begin{bmatrix} \boldsymbol{B}_{AA} & \boldsymbol{B}_{A\psi} \\ \boldsymbol{B}_{A\psi}^{T} & \boldsymbol{B}_{\psi\psi} \end{bmatrix} \begin{bmatrix} \dot{\boldsymbol{a}} \\ \dot{\boldsymbol{u}} \end{bmatrix} + \begin{bmatrix} \boldsymbol{K}_{AA}^{nl} & \boldsymbol{0} \\ \boldsymbol{0} & \boldsymbol{0} \end{bmatrix} \begin{bmatrix} \boldsymbol{a} \\ \boldsymbol{u} \end{bmatrix} = \begin{bmatrix} \boldsymbol{I}_M \\ \boldsymbol{I} \end{bmatrix} \tag{6.36}$$

for nonlinear problems. From (6.29) and (6.30), the expressions of the components in (6.35) and (6.36) are expressed as

$$(\boldsymbol{M}_{AA})_{ij} = -(\boldsymbol{M}_{A\psi})_{ij} = (\boldsymbol{M}_{\psi\psi})_{ij} = \int_{\Omega} \varepsilon N_i N_j d\Omega \tag{6.37}$$

$$(\boldsymbol{B}_{AA})_{ij} = -(\boldsymbol{B}_{A\psi})_{ij} = (\boldsymbol{B}_{\psi\psi})_{ij} = \int_{\Omega} \sigma N_i N_j d\Omega \tag{6.38}$$

$$(\boldsymbol{K}_{AA}^{lin})_{ij} = \int_{\Omega} \nu(\text{grad}N_i \bullet \text{grad}N_j)d\Omega \tag{6.39}$$

$$(\boldsymbol{K}_{AA}^{nl})_{ij} = \int_{\Omega} \nu_0(\text{grad}N_i \bullet \text{grad}N_j)d\Omega \tag{6.40}$$

$$\boldsymbol{I}_i = \int_{\Omega} N_i J d\Omega \tag{6.41}$$

$$\boldsymbol{I}_{Mi} = \int_{\Omega} N_i(\nabla \times \boldsymbol{M})d\Omega \tag{6.42}$$

The assumptions made in this work to simplify the system equations are: a) $-\nabla\phi$ is constant inside the 2-D cross-section area of a conductor [Meu88], i.e., $-\nabla\phi_i$'s at all nodes inside the same cross-section area of a conductor are equal; and b) the induced electric scalar potential inside the magnetic and insulating materials are neglected. Thus, the electric scalar potentials are only considered in the conductor regions, and have the same value in the same conductor region. For n finite-element mesh nodes and k conductors, the n unknowns in $\boldsymbol{u}$ are degenerated to k unknowns, and the dimensions of $\boldsymbol{M}_{A\Psi}(\boldsymbol{B}_{A\Psi})$ and $\boldsymbol{M}_{\Psi\Psi}(\boldsymbol{B}_{\Psi\Psi})$ are changed from n-by-n to n-by-k and k-by-k, respectively. Note that $\boldsymbol{M}_{\Psi\Psi}$ and $\boldsymbol{B}_{\Psi\Psi}$ become diagonal matrices now. Using a similar notation as defined before: $\dot{u}_j = -\nabla\dot{\phi}_j = -\nabla\dot{\Psi}_j = \Delta\dot{V}_j/l_z$, where $\dot{u}_j$ is now defined as the gradient of the electric scalar potential for all nodes inside the cross-section area of the j-th conductor (not for the j-th node), the expressions of the components in $\boldsymbol{M}_{A\Psi}$, $\boldsymbol{B}_{A\Psi}$, $\boldsymbol{M}_{\Psi\Psi}$, $\boldsymbol{B}_{\Psi\Psi}$ and $\boldsymbol{I}$ are changed to

$$(\boldsymbol{M}_{A\Psi})_{ij} = -\int_{S_j} \varepsilon N_i dS_j,\ (\boldsymbol{B}_{A\Psi})_{ij} = -\int_{S_j} \sigma N_i dS_j$$

$$(\boldsymbol{M}_{\Psi\Psi})_{jj} = \int_{S_j} \varepsilon dS_j,\ (\boldsymbol{B}_{\Psi\Psi})_{jj} = \int_{S_j} \sigma dS_j,\ \boldsymbol{I}_j = \int_{S_j} J dS_j \tag{6.43}$$

where S_j is the domain of the total area inside the j-th conductor region, and $\boldsymbol{I}_j$ is now defined as the total current flowing into the j-th conductor.

Equations (6.35) and (6.36) can be expressed in a general form as

$$\boldsymbol{M}_m\ddot{\boldsymbol{p}} + \boldsymbol{B}_m\dot{\boldsymbol{p}} + \boldsymbol{K}_m\boldsymbol{p} = \boldsymbol{F}_m \tag{6.44}$$

where $\boldsymbol{p} = [a \;\; \boldsymbol{u}]^T$, $\boldsymbol{M}_m$ is the mass matrix, $\boldsymbol{B}_m$ the damping matrix, $\boldsymbol{K}_m$ the stiffness matrix, and $\boldsymbol{F}_m$ is the force vector. The domain Ω is approximated by $\Omega = \sum\Omega_e$ where Ω_e is the domain of a finite-element, and the global matrices $\boldsymbol{M}_m$, $\boldsymbol{B}_m$, and $\boldsymbol{K}_m$ are assembled from local matrices $\boldsymbol{m}_e$, $\boldsymbol{b}_e$, and $\boldsymbol{k}_e$. Thus, only elemental matrices or elemental subcircuits need to be derived. In deriving the elemental matrices, the integration area is only over the finite-element domain Ω_e. Since the finite-element assembly method is the same as the Kirchhoff current law, the global circuit model is built from the elemental subcircuits by connecting those nodes which have the same global nodal numbers. The resulting matrix equation formulated by circuit simulators from the global circuit model is the same as the global matrix equation assembled from the elemental matrices by finite element method.

6.2.2 2-D Linear Triangular Finite Element

For a linear triangular finite element shown in Fig. 6.2, the basis functions are

$$N_i(x, y) = \frac{\alpha_i + \beta_i x + \gamma_i y}{2A_e} \qquad i = 1 \text{ to } 3 \tag{6.45}$$

where A_e is the area of a local triangular element, $\alpha_i = x_j^e y_k^e - x_k^e y_j^e$, $\beta_i = y_j^e - y_k^e$,

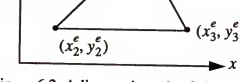

Figure 6.2 A linear triangular finite element

$\gamma_i = x_k^e - x_j^e$, and i, j, k are the cyclic permutation of 1, 2, 3. The analytical integral solutions can be derived as

$$\int_{\Omega_e} N_i N_j d\Omega_e = \begin{cases} \frac{1}{6}A_e, & \text{if } i = j \\ \frac{1}{12}A_e, & \text{if } i \neq j \end{cases}, \quad \int_{\Omega_e} N_i d\Omega_e = \frac{1}{3}A_e, \quad \int_{\Omega_e} d\Omega_e = A_e \tag{6.46}$$

$$\int_{\Omega_e} (\text{grad}N_i) \bullet (\text{grad}N_j) d\Omega_e = \frac{\beta_i\beta_j + \gamma_i\gamma_j}{4A_e} \tag{6.47}$$

The elemental matrices $\boldsymbol{m_e}$, $\boldsymbol{b_e}$, and $\boldsymbol{k_e}$ are derived using the results in (6.46) and (6.47).

6.2.3 Boundary Infinite Element

The boundary condition of the electromagnetic problems at infinity is modeled by the boundary infinite-element [Zie83, Coo89]. For a 1-D infinite-element, i.e., element n_1-n_2-n_3 shown in Fig. 6.3, the distance $l_c = x_2^e - x_1^e = x_1^e - x_0^e$ is a characteristic length of the element. For a mapping between the x-coordinate and the ξ-coordinate, we can write

$$x = M_1 x_1^e + M_2 x_2^e \tag{6.48}$$

where the mapping functions are

$$M_1 = \frac{-2\xi}{1-\xi}, \quad M_2 = \frac{1+\xi}{1-\xi} \tag{6.49}$$

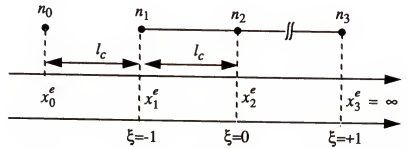

Figure 6.3 A 1-D boundary infinite element n_1-n_2-n_3 in the x-coordinate and the ξ-coordinate

In the mapping, it can be seen that

$$\xi = -1 \rightarrow x = x_1^e, \quad \xi = 0 \rightarrow x = x_2^e, \quad \xi = 1 \rightarrow x = x_3^e = \infty \tag{6.50}$$

and the mapping automatically places n_3 at infinity. For the present three-node (quadratic) infinite-element, the magnetic vector potential $\boldsymbol{A}$ can be expressed as

$$\boldsymbol{A} = \sum_{i=1}^{3} a_i N_i \tag{6.51}$$

where the basis functions in the ξ-coordinate are

$$N_1 = \frac{-\xi + \xi^2}{2}, \quad N_2 = 1 - \xi^2, \quad N_3 = \frac{\xi + \xi^2}{2} \tag{6.52}$$

Since the boundary condition at infinity is zero, i.e., $a_3 = 0$, (6.51) can be simplified to

$$\boldsymbol{A} = a_1 N_1 + a_2 N_2 \tag{6.53}$$

From (6.48) with $x = x_0^e + r$, we can derive

$$\xi = \frac{x - x_2^e}{x - 2x_1^e + x_2^e} = 1 - \frac{2l_c}{x - x_0^e} = 1 - \frac{2l_c}{r} \tag{6.54}$$

Substitution of (6.54) into (6.51) yields

$$\boldsymbol{A} = a_3 + (-a_1 + 4a_2 - 3a_3)\frac{l_c}{r} + (2a_1 - 4a_2 + 2a_3)\frac{l_c^2}{r^2} \tag{6.55}$$

from which it can be seen that as r approaches infinity, $\boldsymbol{A}$ approaches a_3 (= 0, the boundary condition). The term x_0^e represents the pole of the expansion of $\boldsymbol{A}$ in (6.55). In the present work, when applying the 1-D infinite element to the 2-D problems, n_0 is chosen as the origin of the x-y coordinate, and n_2 is obtained from the extension of the line drawn from n_0 to n_1 (which is a boundary node of the finite-element region). In fact, the only geometry information needed in the elemental circuit model is the characteristic length l_c, which can be easily calculated from the coordinate of a boundary node n_1.

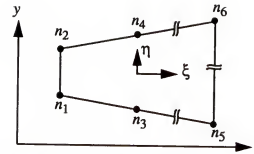

Figure 6.4 A 2-D boundary infinite-element

For a 2-D infinite-element shown in Fig. 6.4, we can write

$$x = \sum_{i=1}^{4} M_i x_i^e, \quad y = \sum_{i=1}^{4} M_i y_i^e \tag{6.56}$$

where the mapping functions are

$$M_1 = \left(\frac{-2\xi}{1-\xi}\right)\left(\frac{1-\eta}{2}\right), \quad M_2 = \left(\frac{-2\xi}{1-\xi}\right)\left(\frac{1+\eta}{2}\right)$$

$$M_3 = \left(\frac{1+\xi}{1-\xi}\right)\left(\frac{1-\eta}{2}\right), \quad M_4 = \left(\frac{1+\xi}{1-\xi}\right)\left(\frac{1+\eta}{2}\right) \tag{6.57}$$

The magnetic vector potential $\boldsymbol{A}$ can be expressed as

$$\boldsymbol{A} = \sum_{i=1}^{6} a_i N_i \tag{6.58}$$

where the basis functions in the ξ-η coordinate are

$$N_1 = \frac{1}{4}(-\xi+\xi^2)(1-\eta), \quad N_2 = \frac{1}{4}(-\xi+\xi^2)(1+\eta)$$

$$N_3 = \frac{1}{2}(1-\xi^2)(1-\eta), \quad N_4 = \frac{1}{2}(1-\xi^2)(1+\eta)$$

$$N_5 = \frac{1}{4}(\xi+\xi^2)(1-\eta), \quad N_6 = \frac{1}{4}(\xi+\xi^2)(1+\eta) \tag{6.59}$$

If a_5 and a_6 are set to zero as boundary conditions, N_5 and N_6 are not needed. The Jacobian J, and the elemental matrices $\boldsymbol{k}_e$ and $\boldsymbol{m}_e$ can be calculated numerically to build the elemental circuit model of the 2-D infinite-element.

6.2.4 Analogy between Magnetic and Circuit Systems

Figure 6.5 shows a parallel RLC circuit, which can be described by

$$C\begin{bmatrix}1 & -1\\ -1 & 1\end{bmatrix}\begin{bmatrix}\dot{V}_1\\ \dot{V}_2\end{bmatrix}+\frac{1}{R}\begin{bmatrix}1 & -1\\ -1 & 1\end{bmatrix}\begin{bmatrix}V_1\\ V_2\end{bmatrix}+\frac{1}{L}\begin{bmatrix}1 & -1\\ -1 & 1\end{bmatrix}\begin{bmatrix}\int V_1\\ \int V_2\end{bmatrix}=\begin{bmatrix}I_1\\ I_2\end{bmatrix} \tag{6.60}$$

Comparing with the semi-discrete equations, (6.44), it is easily seen that the mass matrix $\boldsymbol{M}_m$ can be realized by capacitor elements, the damping matrix $\boldsymbol{B}_m$ by resistor elements, the stiffness matrix $\boldsymbol{K}_m$ by inductor elements, and the force vector $\boldsymbol{F}_m$ by current sources.

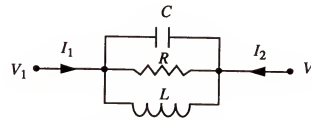

Figure 6.5 A parallel RLC circuit

6.3 Derivation of Elemental Field-Equivalent Subcircuits

6.3.1 Elemental Circuit Model of Magnetic Elements

For a triangular finite-element inside the magnetic (ferrite) materials, the unknowns are $\dot{a}_1$, $\dot{a}_2$, $\dot{a}_3$ and the variables in the hysteresis model. The elemental matrices are calculated to be

$$\boldsymbol{m}_e=\frac{\varepsilon A_e}{12}\begin{bmatrix}2 & 1 & 1\\ 1 & 2 & 1\\ 1 & 1 & 2\end{bmatrix},\ \boldsymbol{b}_e=\frac{\sigma A_e}{12}\begin{bmatrix}2 & 1 & 1\\ 1 & 2 & 1\\ 1 & 1 & 2\end{bmatrix}$$

$$\boldsymbol{k}_e = \left[\frac{\nu(\beta_i\beta_j + \gamma_i\gamma_j)}{4A_e}\right], i, j = 1 \text{ to } 3 \text{ for linear problems}$$

$$\boldsymbol{k}_e = \left[\frac{\nu_0(\beta_i\beta_j + \gamma_i\gamma_j)}{4A_e}\right], i, j = 1 \text{ to } 3 \text{ for nonlinear problems} \qquad (6.61)$$

The nonlinear current components are derived from the following transformation [Edg89]:

$$\int_S N_i(\nabla\times\boldsymbol{M}) \bullet d\boldsymbol{S} = \oint N_i\boldsymbol{M} \bullet d\boldsymbol{l} + \int_S (\boldsymbol{M} \times \text{grad}N_i) \bullet d\boldsymbol{S} \qquad (6.62)$$

Since the closed-loop line integral in (6.62) is zero, the nonlinear current components can be derived as

$$\boldsymbol{I}_{Mi} = \int_S N_i(\nabla\times\boldsymbol{M}) \bullet d\boldsymbol{S} = \int_S (\boldsymbol{M} \times \text{grad}N_i) \bullet d\boldsymbol{S} = \left(\frac{M_x\gamma_i - M_y\beta_i}{2A_e}\right)A_e$$

$$= \frac{1}{2}[M_x(x_k^e - x_j^e) - M_y(y_j^e - y_k^e)] = \frac{1}{2}\boldsymbol{M} \bullet \boldsymbol{L}_{jk} \qquad (6.63)$$

where $\boldsymbol{L}_{jk} = (x_k^e - x_j^e)\hat{x} + (y_k^e - y_j^e)\hat{y}$, and $\boldsymbol{M}$ is obtained from any hysteresis model. Based on the rules discussed in Chapter 2, the elemental matrix $\boldsymbol{m}_e$ is modeled by three equal-valued capacitors,

$$C_1 = \sum_{j=1}^{3} (\boldsymbol{m}_e)_{ij} = \frac{\varepsilon A_e}{3} \quad \text{for } i = 1, 2, 3 \qquad (6.64)$$

connecting the three element nodes to ground, and by the other three equal-valued capacitors,

$$C_2 = -(\boldsymbol{m}_e)_{ij} = \frac{-\varepsilon A_e}{12} \quad \text{for } i \neq j \qquad (6.65)$$

connected among the three element nodes. The elemental matrix $\boldsymbol{b}_e$ is modeled by three equal-valued resistors,

$$R_1 = 1/\sum_{j=1}^{3} (\boldsymbol{b}_e)_{ij} = \frac{3}{\sigma A_e} \quad \text{for } i = 1, 2, 3 \qquad (6.66)$$

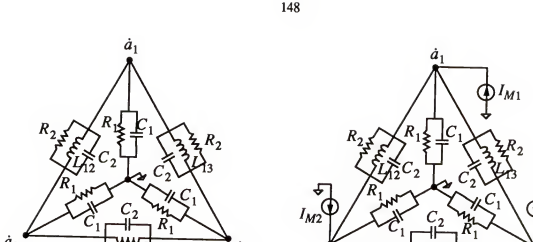

Figure 6.6 2-D field-equivalent subcircuit for a triangular linear magnetic element (a); and for a triangular nonlinear magnetic element (b).

connecting the three element nodes to ground, and by the other three equal-valued resistors,

$$R_2 = -1/(\boldsymbol{b}_e)_{ij} = \frac{-12}{\sigma A_e} \quad \text{for } i \neq j \tag{6.67}$$

connected among the three element nodes. The elemental matrix $\boldsymbol{k}_e$ is modeled by three inductors connected among the three element nodes,

$$L_{ij} = -1/(\boldsymbol{k}_e)_{ij} = \frac{-4A_e}{\nu(\beta_i\beta_j + \gamma_i\gamma_j)}, \quad 1 \le i < j \le 3 \text{ for linear problems}$$

$$L_{ij} = -1/(\boldsymbol{k}_e)_{ij} = \frac{-4A_e}{\nu_0(\beta_i\beta_j + \gamma_i\gamma_j)}, \quad 1 \le i < j \le 3 \text{ for nonlinear problems} \tag{6.68}$$

No inductor is needed to connect the element nodes to ground because the sum of those terms in the same row or column in $\boldsymbol{k}_e$ is zero. The elemental circuit models for the linear and nonlinear magnetic elements are shown in Fig. 6.6.

6.3.2 Elemental Circuit Models of Conductive and Insulating Elements

For a triangular finite-element inside the i-th winding conductor, the unknowns are $\dot{a}_1$, $\dot{a}_2$, $\dot{a}_3$, and $\dot{u}_i$, and the elemental matrices are calculated to be

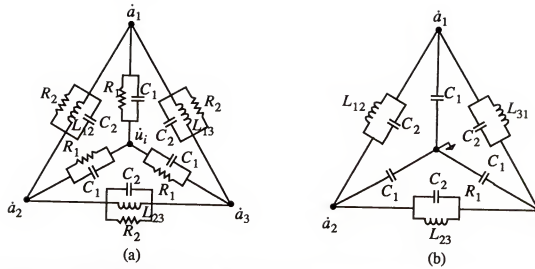

Figure 6.7 2-D field-equivalent subcircuit for a triangular conductive (copper) element (a); and for a triangular insulating (air) element (b).

$$\boldsymbol{m}_e = \frac{\varepsilon_0 A_e}{12}\begin{bmatrix} 2 & 1 & 1 & -4 \\ 1 & 2 & 1 & -4 \\ 1 & 1 & 2 & -4 \\ -4 & -4 & -4 & 12 \end{bmatrix}, \quad \boldsymbol{b}_e = \frac{\sigma A_e}{12}\begin{bmatrix} 2 & 1 & 1 & -4 \\ 1 & 2 & 1 & -4 \\ 1 & 1 & 2 & -4 \\ -4 & -4 & -4 & 12 \end{bmatrix} \tag{6.69}$$

$$\boldsymbol{k}_e = \left[\frac{\nu_0(\beta_i\beta_j + \gamma_i\gamma_j)}{4A_e}\right], \; i, j = 1 \text{ to } 3 \tag{6.70}$$

For a triangular finite-element inside the insulating materials (including air), the unknowns are $\dot{a}_1$, $\dot{a}_2$, and $\dot{a}_3$, and the elemental matrices are calculated to be

$$\boldsymbol{m}_e = \frac{\varepsilon_0 A_e}{12}\begin{bmatrix} 2 & 1 & 1 \\ 1 & 2 & 1 \\ 1 & 1 & 2 \end{bmatrix}, \quad \boldsymbol{k}_e = \left[\frac{\nu_0(\beta_i\beta_j + \gamma_i\gamma_j)}{4A_e}\right], \; i, j = 1 \text{ to } 3 \tag{6.71}$$

The elemental damping matrix $\boldsymbol{b}_e$ for the insulating elements is a null matrix since the conductivity is zero. Based on the rules discussed in Chapter 2, the derived elemental circuit models of the conductive and the insulating elements are shown in Fig. 6.7, where the RLC components are the same as those for the magnetic elements except ε is replaced by ε_0, and ν by ν_0. Note that no circuit component is needed to connect the element

nodes to ground for the conductive elements, because the sum of those terms in the same row or column in $\boldsymbol{m}_e$, $\boldsymbol{b}_e$, and $\boldsymbol{k}_e$ is zero.

6.3.3 Elemental Circuit Model of 1-D Infinite Element

The elemental circuit model of the 1-D infinite-element is derived analytically, and that of the 2-D infinite-element can be derived numerically. Only the derivation of the elemental circuit model for the 1-D infinite-element is discussed here. To derive the elemental circuit model, we need to find the Jacobian J, which is derived as

$$J = \frac{dx}{d\xi} = M_{1,\xi} x_1^e + M_{2,\xi} x_2^e = \frac{2l_c}{(1-\xi)^2} \tag{6.72}$$

The elemental matrices for the 1-D infinite-element are calculated to be

$$\boldsymbol{m}_e = \varepsilon_0 l_c \begin{bmatrix} \frac{1}{3} & \frac{-2}{3} \\ \frac{-2}{3} & \frac{16}{3} \end{bmatrix}, \quad \boldsymbol{k}_e = \frac{v_0}{l_c} \begin{bmatrix} \frac{23}{15} & \frac{-26}{15} \\ \frac{-26}{15} & \frac{32}{15} \end{bmatrix} \tag{6.73}$$

Based on the rules discussed in Chapter 2, the elemental matrix $\boldsymbol{m}_e$ is realized by three capacitors,

$$C_1^b = (\boldsymbol{m}_e)_{11} + (\boldsymbol{m}_e)_{12} = \frac{-\varepsilon_0 l_c}{3}$$

$$C_2^b = (\boldsymbol{m}_e)_{21} + (\boldsymbol{m}_e)_{22} = \frac{14\varepsilon_0 l_c}{3}$$

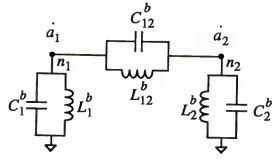

Figure 6.8 Elemental circuit model of a 1-D boundary infinite-element

$$C_{12}^{b} = -(\boldsymbol{m}_e)_{12} = \frac{2\varepsilon_0 l_c}{3} \tag{6.74}$$

and the elemental matrix $\boldsymbol{k}_e$ is realized by three inductors,

$$L_1^b = 1/[(\boldsymbol{k}_e)_{11} + (\boldsymbol{k}_e)_{12}] = \frac{-5l_c}{\nu_0}$$

$$L_2^b = 1/[(\boldsymbol{k}_e)_{21} + (\boldsymbol{k}_e)_{22}] = \frac{5l_c}{2\nu_0}$$

$$L_{12}^b = -1/(\boldsymbol{k}_e)_{12} = \frac{15l_c}{26\nu_0} \tag{6.75}$$

The elemental circuit model of the 1-D infinite-element is shown in Fig. 6.8, where node n_1 is connected to a boundary node of the finite-element region.

6.3.4 Interface Circuit Network

For the currents I_1 and I_2 flowing in the transformer windings as shown in Fig. 6.9(a), the corresponding currents in the conductors of the 2-D problems change signs alternately, and so are the corresponding electric fields. Since the voltage drop in a winding is

$$V = \Delta V_1 - \Delta V_2 + \Delta V_3 - \Delta V_4 \ \ldots = l_z\dot{u}_1 - l_z\dot{u}_2 + l_z\dot{u}_3 - l_z\dot{u}_4 \ \ldots \tag{6.76}$$

the interface network can be built by the controlled voltage and current sources as shown in Fig. 6.9(b), where n_1 and n_2 are the numbers of turns in the primary and secondary windings, respectively.

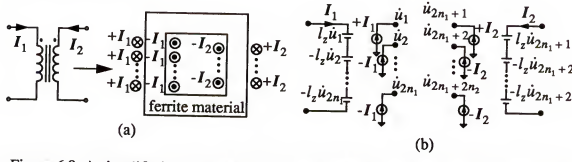

Figure 6.9 A simplified 2D geometry of a transformer (a); and an interface network (b).

6.3.5 Modification of the Elemental Circuit Models in Implementation

Since circuit simulators such as SABER can not simulate parallel inductors, the previously derived elemental circuit models have to be modified in the implementation. It is not convenient to assemble parallel inductors globally then perform the simulation, because the inductor currents in each finite-element are used to calculate the elemental magnetic flux density as will be discussed later. To avoid the problem, two approaches are applied. One is to add a very small resistor in series with each inductor in the elemental models. The other is to replace each inductor by an equivalent current source.

The inductor model between node i and node j in a triangular finite-element is written as

$$\dot{a}_i - \dot{a}_j = \frac{-4A_e}{\nu(\beta_i\beta_j + \gamma_i\gamma_j)}\frac{dI_{Lij}}{dt} \tag{6.77}$$

where I_{Lij} is the inductor current flowing from node i to node j, and $\nu = \nu_0$ for conductive, insulating, and nonlinear magnetic elements. Using the backward Euler approximation, we can write

$$I_{Lij}(t_n) = I_{Lij}(t_{n-1}) + \left[\frac{\nu(\beta_i\beta_j + \gamma_i\gamma_j)}{-4A_e}\right][\dot{a}_i(t_n) - \dot{a}_j(t_n)](t_n - t_{n-1}) \tag{6.78}$$

where I_{Lij} is modeled by the state variable in SABER so that the previous value can be retained in the model.

6.3.6 Inclusion of Hysteresis Models in the Magnetic Subcircuit

For the 2-D electromagnetic problems, we can write

$$\boldsymbol{B}(x,y,t) = \nabla\times\boldsymbol{A}(x,y,t) = \frac{\partial}{\partial y}A_z(x,y,t)\hat{x} - \frac{\partial}{\partial x}A_z(x,y,t)\hat{y}$$

$$= \left(\sum_{i=1}^{3} a_i(t)N_{i,y}(x,y)\right)\hat{x} - \left(\sum_{i=1}^{3} a_i(t)N_{i,x}(x,y)\right)\hat{y}$$

$$= \left(\sum_{i=1}^{3} \frac{a_i(t)\gamma_i}{2A_e} \right) \hat{x} - \left(\sum_{i=1}^{3} \frac{a_i(t)\beta_i}{2A_e} \right) \hat{y} \equiv B_x \hat{x} + B_y \hat{y} \tag{6.79}$$

where $A_z(x, y, t) = \sum_{i=1}^{3} a_i(t) N_i(x, y)$ for a 2-D triangular finite-element. From the elemental matrix equations, we can derive

$$a_1(t) - a_2(t) = -I_{L12}(t)/k_{12} \tag{6.80}$$

$$a_2(t) - a_3(t) = -I_{L23}(t)/k_{23} \tag{6.81}$$

$$a_3(t) - a_1(t) = -I_{L31}(t)/k_{31} \tag{6.82}$$

where $k_{ij} = \dfrac{\nu_0(\beta_i\beta_j + \gamma_i\gamma_j)}{4A_e}$ for the nonlinear magnetic elements. From (6.79) - (6.82), we can obtain

$$B_x = \frac{a_1\gamma_1 + a_2\gamma_2 + a_3\gamma_3}{2A_e} = \frac{x_3^e(a_1 - a_2) + x_2^e(a_3 - a_1) + x_1^e(a_2 - a_3)}{2A_e}$$

$$= \frac{-2}{\nu_0}\left[\frac{x_3^e I_{L12}}{\beta_1\beta_2 + \gamma_1\gamma_2} + \frac{x_2^e I_{L31}}{\beta_3\beta_1 + \gamma_3\gamma_1} + \frac{x_1^e I_{L23}}{\beta_2\beta_3 + \gamma_2\gamma_3} \right] \tag{6.83}$$

$$B_y = \frac{-a_1\beta_1 - a_2\beta_2 - a_3\beta_3}{2A_e} = \frac{y_3^e(a_1 - a_2) + y_2^e(a_3 - a_1) + y_1^e(a_2 - a_3)}{2A_e}$$

$$= \frac{-2}{\nu_0}\left[\frac{y_3^e I_{L12}}{\beta_1\beta_2 + \gamma_1\gamma_2} + \frac{y_2^e I_{L31}}{\beta_3\beta_1 + \gamma_3\gamma_1} + \frac{y_1^e I_{L23}}{\beta_2\beta_3 + \gamma_2\gamma_3} \right] \tag{6.84}$$

Thus, the magnetic flux densities B_x and B_y in a finite-element are calculated from the inductor currents I_{L12}, I_{L23}, and I_{L31}. From any hysteresis model, we can reversely solve H_x from B_x, and H_y from B_y, then find M_x and M_y so that the nonlinear current components I_{Mi}'s as defined in (6.63) can be computed. The unknowns B_x, B_y, H_x, H_y, M_x, M_y, I_{Lij}'s, I_{Mi}'s, and $\dot{a}_i$'s in the nonlinear subcircuit model are solved from the assembled global circuit using the built-in numerical solver in SABER. By controlling the sample-points and the newton-steps in SABER, the convergence problems can be avoided.

Two issues in the implementation of the model need to be pointed out. The first issue is that $\beta_i\beta_j + \gamma_i\gamma_j = 0$ if the angle at node k is a right angle (which can be proved analytically), and (6.83) - (6.84) need to be modified using the following relation:

$$\frac{I_{L12}}{\beta_1\beta_2 + \gamma_1\gamma_2} + \frac{I_{L23}}{\beta_2\beta_3 + \gamma_2\gamma_3} + \frac{I_{L31}}{\beta_3\beta_1 + \gamma_3\gamma_1} = 0 \tag{6.85}$$

which is obtained from (6.80) - (6.82). For example, if $\beta_1\beta_2 + \gamma_1\gamma_2 = 0$, (6.83) and (6.84) can be modified using (6.85) as

$$B_x = \frac{-2}{\nu_0}\left[\frac{(x_2^e - x_3^e)I_{L31}}{\beta_3\beta_1 + \gamma_3\gamma_1} + \frac{(x_1^e - x_3^e)I_{L23}}{\beta_2\beta_3 + \gamma_2\gamma_3}\right] \tag{6.86}$$

$$B_y = \frac{-2}{\nu_0}\left[\frac{(y_2^e - y_3^e)I_{L31}}{\beta_3\beta_1 + \gamma_3\gamma_1} + \frac{(y_1^e - y_3^e)I_{L23}}{\beta_2\beta_3 + \gamma_2\gamma_3}\right] \tag{6.87}$$

Similar equations can be derived for the cases when $\beta_2\beta_3 + \gamma_2\gamma_3 = 0$ and when $\beta_3\beta_1 + \gamma_3\gamma_1 = 0$.

The second issue is $|\boldsymbol{B}| = \sqrt{B_x^2 + B_y^2}$ may exceed the saturated flux density B_{sat} even when both B_x and B_y are below B_{sat}. To avoid this problem, the magnitude $|\boldsymbol{B}|$ is monitored in the model. Whenever $|\boldsymbol{B}|$ exceeds B_{sat}, both B_x and B_y are retained as the same values in the previous time-step. Another way to avoid this problem is to find $\boldsymbol{B}$ from B_x and B_y, then solve $\boldsymbol{H}$ and $\boldsymbol{M}$ from any hysteresis model, and finally decompose $\boldsymbol{M}$ into M_x and M_y to compute the nonlinear current components. Since $\boldsymbol{B}$ instead of B_x or B_y is used in the hysteresis model, $|\boldsymbol{B}| \le B_{sat}$ is always satisfied.

6.4 Field-Based Circuit Modeling Methodology

The field-based finite-element circuit models developed in the previous section are applied here to model magnetic components. To build the field-based circuit model for a magnetic component, the first step is to draw the geometry of the magnetic component on a meshmaker, and to make finite-element meshes in the defined region. The origin of the

x-y coordinates is chosen as the central point of the defined finite-element region, and corresponds to the n_0 node, i.e., the pole, for all 1-D infinite elements; thus, the circuit models for the 1-D infinite elements can be simply calculated from the coordinates of the external boundary nodes of the finite-element region.

Programs (/thesis_programs/mag_fem.m) are written to read the geometry data files (fileset2.pts, fileset2.lin, fileset2.tri) generated by the meshmaker, and to produce automatically a SABER template which describes the overall field-based circuit model for the magnetic component. The generated SABER template is then combined with the external circuitry to build a SABER input file for simulation of the coupled electrical and magnetic systems.

For example, a transformer made of a Philips 768T188-3C85 toroid, with 18 turns of primary windings and 18 turns of secondary windings, is drawn on the meshmaker, and the 2-D triangular meshes generated by the meshmaker are shown in Fig. 6.10(a), where each triangular mesh corresponds to a field-equivalent subcircuit. The coordinates of the nodes in the line boundary Γ_b are used to generate the circuit models for the 1-D infinite elements to account for the boundary condition at infinity. The generated meshes for a

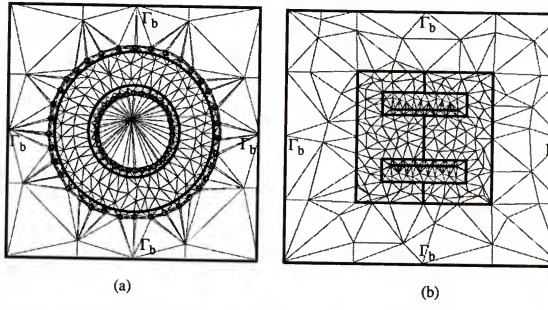

Figure 6.10 Generated 2-D triangular meshes for modeling of a transformer made of a 768T188-3C85 toroid (a); and E625-3C85 E-cores (b).

transformer made of Philips E625-3C85 E-cores, with 10 turns of primary windings and 10 turns of secondary windings, are also shown in Fig. 6.10(b). The overall field-based circuit models, including nonlinear magnetic (ferrite) subcircuits, for the transformers shown in Fig. 6.10 are generated automatically. As shown in Fig. 6.11, the overall field-based circuit model for a magnetic component consists of a "field-equivalent circuit" and an "interface network." The field-equivalent circuit is constructed from the elemental field-equivalent subcircuits according to a topology dictated by the geometry of the magnetic component, giving rise to a "geometry-dependent" dynamic circuit model for the electromagnetic fields within and outside the magnetic component. The interface network connects the field-equivalent circuit to the external circuitry. The resulting nonlinear transformer models will be verified by experimental data in next section.

The same modeling procedure is again repeated to generate an overall field-based circuit model, including linear magnetic (ferrite) subcircuits, for a transformer shown in Fig. 6.12(a). The resulting linear transformer model will be verified by the Maxwell finite-element software [Max93] in next section.

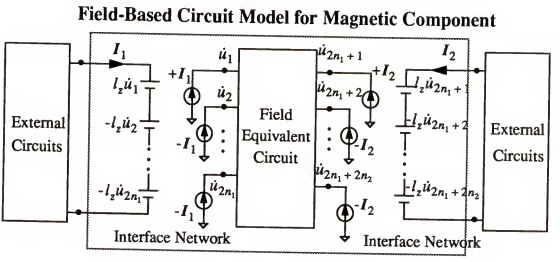

Figure 6.11 Constituents of the field-based circuit model for a magnetic component: the "field-equivalent circuit" and the "interface network."

6.5 Verification

The generated linear field-based circuit model for the transformer shown in Fig. 6.12(a) is verified by the simulation results from the Maxwell finite-element software. The simulated inductances from circuit simulation are compared with those from Maxwell simulation in Fig. 6.12(b). In the circuit simulation, the inductances are directly calculated from the simulated winding currents and voltages using the relation:

$$L = V_L \Big/ \left(\frac{di_L}{dt}\right) \tag{6.88}$$

while in the Maxwell simulation, the inductances are calculated from the elemental *B-H* solutions in all finite elements using the relation [Max93]:

$$L = \frac{1}{i_L^2} \int_{\Omega} H \cdot B d\Omega \tag{6.89}$$

where i_L is the excitation current, and $\Omega = \sum \Omega_e$. The slight differences in the inductance values may be due to the small error in determining di_L/dt and V_L from circuit simulation results, or due to the small error from the assumptions made in deriving the circuit models.

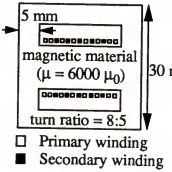

(a)

Methods / Inductances	Maxwell simulation	Circuit simulation
$L_p(uH)$	377	364
$L_s(uH)$	147	142
$L_{p,leakage}(nH)$	102	100
$L_{s,leakage}(nH)$	19	29

(b)

Figure 6. 12 2-D geometry of a tested transformer (shown without the test bed) (a); and the simulated inductance values from the Maxwell simulator and from the field-based circuit model (b).

The nonlinear magnetic subcircuit including a hysteresis model for the magnetic (ferrite) elements is verified by the experimental voltage and current waveforms which show the hysteresis effects. The experimental waveforms are acquired by the LabWindows software. Figure 6.13 shows a simple test circuit which includes the overall nonlinear field-based circuit model for the transformer shown in Fig. 6.10(a). In the simulation, the operating temperature is fixed at $T = 25^{o}C$, and the parameters of the hysteresis model are those extracted at $T = 25^{o}C$; while in the experiment, the period of the input excitation voltage is controlled to only several cycles of the operating frequency to avoid the temperature rise inside the core. To simulate the very large finite-element circuit network in SABER, the command "saber -config memory_model:flat file.sin", which dynamically allocates the memory, is used to simulate the file.sin input file. The simulated primary current i_1 and secondary voltage V_2 at $V_m = 9V$ are compared with the experimental waveforms in Fig. 6.14 and Fig. 6.15, respectively; and those at $V_m = 20V$ are compared with the experimental waveforms in Fig. 6.16 and Fig. 6.17. Note that the measured voltage and current waveforms by the oscilloscope do not include the magnetizing transients; thus, they are only compared with the simulated results after the first cycle. The satisfactory agreements between the simulated and the experimental results validate the proposed nonlinear magnetic subcircuit, and the finite-element/circuit formulation for the inclusion of hysteresis models in the finite-element analysis of magnetic devices.

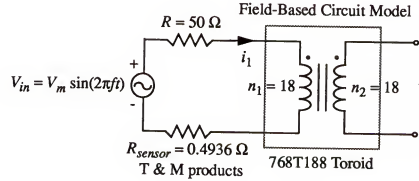

Figure 6.13 A simple test circuit for the verification of the nonlinear magnetic subcircuit; $f = 10$ kHz.

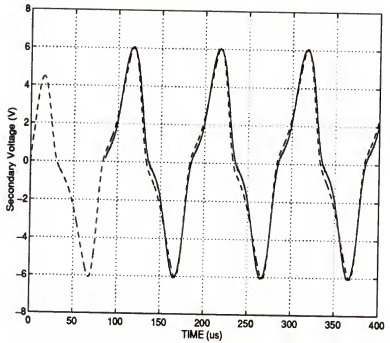

Figure 6.14 Simulated and experimental secondary voltages at $V_m = 9$ V; solid line: experimental waveform; dashed line: simulated waveform.

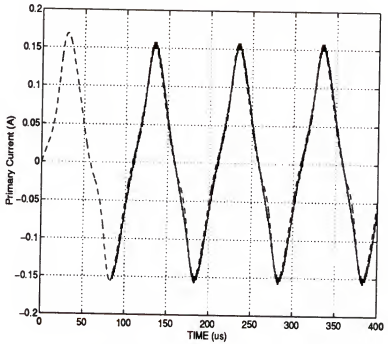

Figure 6.15 Simulated and experimental primary currents at $V_m = 9$ V; solid line: experimental waveform; dashed line: simulated waveform.

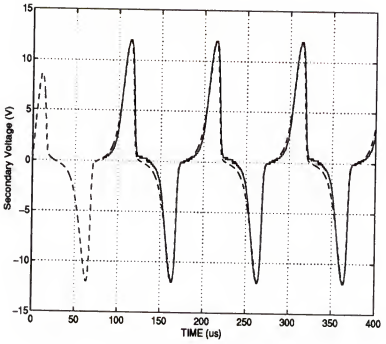

Figure 6.16 Simulated and experimental secondary voltages at $V_m = 20$ V; solid line: experimental waveform; dashed line: simulated waveform.

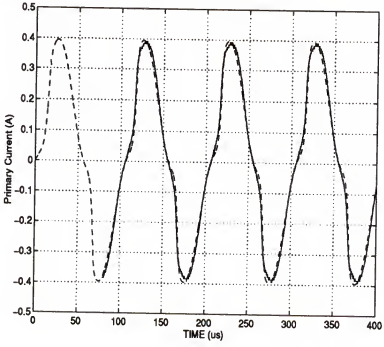

Figure 6.17 Simulated and experimental primary currents at $V_m = 20$ V; solid line: experimental waveform; dashed line: simulated waveform.

6.6 Summary

Field-based finite-element circuit models, which could take into account the hysteresis, geometry, frequency, large-signal, and waveshape effects, have been developed. The field-based modeling methodology allows the users of circuit simulators to perform finite-element simulation of magnetic devices coupled with a wide range of circuit topologies in the circuit simulators. A new finite-element/circuit formulation has also been developed to include any kind of hysteresis models in the finite-element analysis of magnetic devices.

CHAPTER 7
FINITE-ELEMENT CIRCUIT MODELS FOR MAGNETO-THERMAL SIMULATION OF MAGNETIC DEVICES

7.1 Introduction

With the development of high-frequency switching mode power supplies, the size of the magnetic devices is shrinking and thermal effects in the magnetic devices are becoming important factors in magnetic designs. High-frequency magnetic designs are limited by thermal considerations [Nel92], although conventional low-frequency magnetic designs are only limited by magnetic considerations. One important factor in high-frequency magnetic designs is that the maximum core temperature should not exceed the Curie temperature. To reduce the time and cost in high-frequency magnetic designs, it is desired to have CAD models which could simulate the dynamically coupled magnetic and thermal systems, and which could take into account the hysteresis, geometry, frequency, large-signal, and waveshape effects.

Numerical analyses of the coupled magnetic and thermal systems have been discussed in the area of induction heating [Lav83, Mas85, Gar87, Cha94]; however, only the eddy-current losses rather than the combination of eddy-current, hysteresis, and anomalous losses were considered. A 2-D finite-element axisymmetric magneto-thermal model was discussed in Nelson and Jessee [Nel92]; however, the model assumed a) the system is only excited by sinusoidal sources; b) only quasi-static thermal solutions are solved; c) only the heat transfer by conduction (without convection) is considered; and d) the magnetic field is only contained within the magnetic devices. The last assumption is valid for the simulation of high-permeability magnetic materials, but is not valid for the simulation of low-permeability magnetic materials which are useful in the design of high-frequency resonant inductors.

This chapter presents finite-element magneto-thermal circuit models for the coupled magnetic and thermal systems. The 2-D triangular thermal circuit models developed in Chapter 2, the rate-dependent and temperature-dependent hysteresis model developed in Chapter 5, and the field-based finite-element magnetic circuit models developed in Chapter 6, are combined to build the magneto-thermal circuit models for magneto-thermal simulation of magnetic devices. To increase the efficiency of magneto-thermal simulation, axisymmetric formulations are applied to develop 1-D magneto-thermal circuit models for magnetic devices made of toroids. The core losses evaluated from the experimentally verified hysteresis model include the hysteresis, eddy-current, and anomalous losses. Using the developed magneto-thermal circuit models, both the magnetic and the thermal transient phenomena in the magnetic devices can be simulated. To efficiently obtain the steady-state solutions of the coupled magnetic and thermal systems, an iterative process is also discussed.

The coupled magneto-thermal equations will be discussed in Section 7.2. The 2-D magneto-thermal subcircuits, and the 1-D axisymmetric magneto-thermal subcircuits for magnetic devices made of toroids are developed in Section 7.3. Evaluation of the internal heat generation in magnetic devices is discussed in Section 7.4. Simulation results and verification are presented in Section 7.5.

7.2 Coupled Magneto-Thermal Equations

This section will describe the system equations for the coupled magnetic and thermal systems, and discuss the coupling between these two systems. The magnetic system is governed by the partial subset of Maxwell's equations:

$$\nabla \bullet \boldsymbol{B} = 0 \tag{7.1}$$

$$\nabla \times \boldsymbol{E} = -\dot{\boldsymbol{B}} \tag{7.2}$$

$$\nabla \times \boldsymbol{H} = \boldsymbol{J} = \boldsymbol{J}_{cond} + \dot{\boldsymbol{D}} \tag{7.3}$$

From the potential definitions:

$$\boldsymbol{B} = \nabla \times \boldsymbol{A}\,,\ \boldsymbol{E} = -\nabla\phi - \dot{\boldsymbol{A}} \tag{7.4}$$

and the constitutive laws:

$$\boldsymbol{J}_{cond} = \sigma \boldsymbol{E}\,,\ \boldsymbol{D} = \varepsilon \boldsymbol{E}\,,\ \boldsymbol{B} = \mu_0(\boldsymbol{H} + \boldsymbol{M}) \tag{7.5}$$

the semi-discrete equations are derived from a Galerkin finite element projection as

$$\boldsymbol{M}_m \dot{\boldsymbol{p}}^{\cdot} + \boldsymbol{B}_m \dot{\boldsymbol{p}} + \boldsymbol{K}_m \boldsymbol{p} = \boldsymbol{F}_m \tag{7.6}$$

where $\boldsymbol{M}_m$, $\boldsymbol{B}_m$, $\boldsymbol{K}_m$, and $\boldsymbol{F}_m$ represent the mass matrix, damping matrix, stiffness matrix, and force vector for the magnetic system, respectively. $\boldsymbol{p} = [\boldsymbol{a}\ \ \boldsymbol{u}]^{\mathrm{T}}$, where $\boldsymbol{a}$ is the vector of nodal magnetic vector potentials a_i's, and $\boldsymbol{u}$ is the vector of u_i's $= -\nabla\psi_i$'s, where ψ_i is the time integral of the electric scalar potential at node i. The mass matrix can be realized by capacitor elements, the damping matrix by resistor elements, the stiffness matrix by inductor elements, and the force vector by current sources. The expressions of the components in $\boldsymbol{M}_m$, $\boldsymbol{B}_m$, $\boldsymbol{K}_m$, and $\boldsymbol{F}_m$ are shown in Chapter 6. The conductivity σ and the permittivity ε are assumed constants, and the conventional concept of reluctivity (or permeability) is implied in the rate-dependent and temperature-dependent hysteresis model. For the 2-D finite-element magneto-thermal circuit models, B_x, B_y, H_x, H_y, M_x, and M_y are needed, and there are two hysteresis models in each magnetic (ferrite) subcircuit. For the 1-D axisymmetric finite-element magneto-thermal circuit models, B, H, and M are needed, and there is only one hysteresis model in each magnetic (ferrite) subcircuit.

The thermal system for the coupled magneto-thermal problems is slightly different from that for the coupled electro-thermal problems. The main difference lies in the mathematical assumptions made for the power losses. In the coupled electro-thermal system, the power loss can be approximated as a boundary condition as discussed in Chapter 2, although it is actually due to the internal heat generation. In the coupled magneto-thermal system, the power loss can not be approximated as a boundary

condition, and it can be only modeled as the internal heat generation. The internal heat generation g with unit W/m^3 is in fact the core loss density for the magnetic devices.

The thermal system inside the magnetic devices is governed by

$$\mathrm{div}(\kappa\ \mathrm{grad}T) + g = \rho c_p \frac{\partial T}{\partial t} \text{ in } \Omega \tag{7.7}$$

with boundary condition

$$\kappa \mathrm{grad}T \bullet n = \kappa \frac{\partial T}{\partial n} = h(T_a - T) \text{ on } \Gamma \equiv \partial\Omega \tag{7.8}$$

and initial condition

$$T(x, 0) = T_a = 300K \tag{7.9}$$

where Ω represents the mathematical domain of the magnetic materials, and $\Gamma \equiv \partial\Omega$ the boundary touching the air. The material properties, i.e., the thermal conductivity κ, the specific heat c_p, and the mass density ρ in the thermal system are assumed constants [Nel92]. The coefficient h, which ideally includes both the convection and the radiation effects, is also assumed constant for simplicity. In this work, we concentrate on the analysis of the magneto-thermal coupling inside the magnetic (ferrite) materials; thus, only the core loss densities in the magnetic materials are considered. However, the copper loss densities in the windings can be incorporated into the analysis using a similar approach for the core loss densities.

The semidiscrete equation of (7.7) - (7.9), derived from a Galerkin finite element projection [Hug87], is

$$\boldsymbol{M}_T \dot{\boldsymbol{d}} + \boldsymbol{K}_T \boldsymbol{d} = \boldsymbol{F}_T \tag{7.10}$$

where $\boldsymbol{M}_T$, $\boldsymbol{K}_T$, and $\boldsymbol{F}_T$ represent the mass matrix, stiffness matrix, and force vector for the thermal system, respectively, and $\boldsymbol{d}$ is the vector of nodal temperatures. The mass matrix can be realized by capacitor elements, the stiffness matrix by resistor elements, and

the force vector by current sources. The global matrices $\boldsymbol{M}_T$, $\boldsymbol{K}_T$, and $\boldsymbol{F}_T$ are assembled from the elemental matrices $\boldsymbol{m}_e$, $\boldsymbol{k}_e$, and $\boldsymbol{f}_e$, and the expressions for the components in the elemental matrices are given below:

$$(m_e)_{ij} = \rho c_p \int_{\Omega_e} N_i N_j d\Omega_e \tag{7.11}$$

$$(k_e)_{ij} = \kappa \int_{\Omega_e} \text{grad}\, N_i \bullet \text{grad}\, N_j \, d\Omega_e + h \int_{\Gamma} N_i N_j d\Gamma \tag{7.12}$$

$$(f_e)_i = hT_a \int_{\Gamma} N_i d\Gamma + \int_{\Omega_e} g N_i d\Omega_e \tag{7.13}$$

where N_i's are the finite-element basis functions. Equation (7.11) and the first term of (7.12) are the conductive terms. The second term of (7.12) and the first term of (7.13) are the convective terms. The second term of (7.13) is the internal heat generation term.

Figure 7.1 shows a coupled magneto-thermal system, where the internal heat generation $\boldsymbol{g}(\boldsymbol{B}(\boldsymbol{d}), \boldsymbol{H}(\boldsymbol{d}))$ is obtained from the rate-dependent and temperature-dependent hysteresis model implemented in each magnetic (ferrite) subcircuit. From Fig. 7.1, it can be seen that the coupling between these two systems is based on the nodal temperatures $\boldsymbol{d}$ and the internal heat generations $\boldsymbol{g}$. Note that d_i's in $\boldsymbol{d}$ are treated as system variables in the SABER circuit simulator, and the coupled magnetic and thermal systems are solved simultaneously.

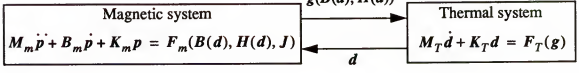

Figure 7.1 Coupled magneto-thermal system.

7.3 Finite-Element Magneto-Thermal Circuit Models

7.3.1 2-D Magneto-Thermal Subcircuits

In this section, the finite-element thermal circuit models developed in Chapter 2 and the finite-element magnetic circuit models developed in Chapter 6 are combined to build the finite-element magneto-thermal circuit models. The overall magneto-thermal circuit models consist of five elemental subcircuits, i.e., the magneto-thermal subcircuit for the magnetic (ferrite) elements, the convective thermal subcircuit, and the magnetic subcircuits for the conductive (copper) elements, insulating (air) elements, and boundary infinite elements. The 2-D triangular conductive thermal subcircuit is combined with the triangular magnetic subcircuit to formulate the magneto-thermal subcircuit for the magnetic (ferrite) elements; and the magneto-thermal subcircuit is shown in Fig. 7.2, where

$$C_1 = \frac{\varepsilon A_e}{3},\ C_2 = \frac{-\varepsilon A_e}{12},\ R_1 = \frac{3}{\sigma A_e},\ R_2 = \frac{-12}{\sigma A_e}$$

$$L_{ij} = \frac{-4A_e}{\nu_0(\beta_i\beta_j + \gamma_i\gamma_j)},\quad 1 \le i < j \le 3$$

$$I_{Mi} = \frac{1}{2}[M_x(x_k^e - x_j^e) + M_y(y_k^e - y_j^e)] \tag{7.14}$$

$$C_1^d = \rho c_p A_e/3,\ C_2^d = -\rho c_p A_e/12$$

$$R_{ij}^d = \frac{-4A_e}{\kappa(\beta_i\beta_j + \gamma_i\gamma_j)},\quad 1 \le i < j \le 3$$

$$I^g = \frac{gA_e}{3} \tag{7.15}$$

There are two unknowns in each elemental node of the magnetic (ferrite) elements, i.e., the nodal temperature d_i and the time-derivative of the nodal magnetic vector potential $\dot{a}_i$. The internal heat generation g will be determined in Section 7.4. The 2-D convective thermal subcircuit is shown in Fig. 7.3(a), where

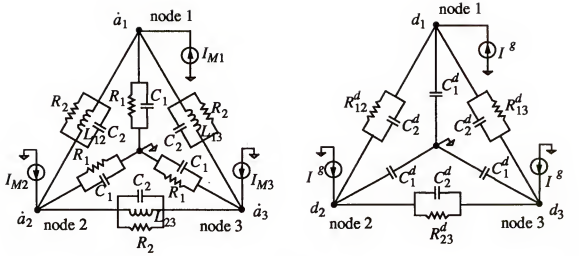

Figure 7.2 A triangular finite-element magneto-thermal subcircuit for the magnetic (ferrite) elements.

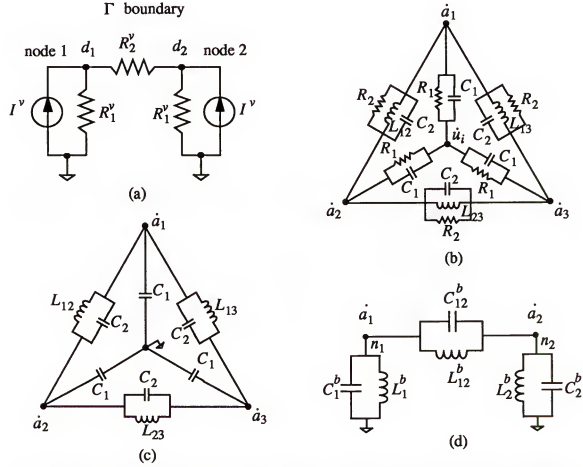

Figure 7.3 2-D convective thermal subcircuit (a); and subcircuits for the conductive (copper) elements (b); for the insulating (air) elements (c); and for the 1-D infinite elements (d).

$$R_1^v = 2/hL_\Gamma, R_2^v = -6/hL_\Gamma, I^v = hT_aL_\Gamma/2 \tag{7.16}$$

where L_Γ is the length of the Γ (convective) boundary line in a local triangular element. The subcircuits for the conductive and insulating elements are shown in Fig. 7.3(b) and Fig. 7.3 (c), respectively, where the RLC expressions are the same as those shown in (7.14), except that ε is replaced by ε_0. The subcircuit for the 1-D boundary infinite elements is shown in Fig. 7.3(d), where

$$C_1^b = \frac{-\varepsilon_0 l_c}{3}, C_2^b = \frac{14\varepsilon_0 l_c}{3}, C_{12}^b = \frac{2\varepsilon_0 l_c}{3}$$
$$L_1^b = \frac{-5l_c}{\nu_0}, L_2^b = \frac{5l_c}{2\nu_0}, L_{12}^b = \frac{15l_c}{26\nu_0} \tag{7.17}$$

These elemental circuit models are to be applied for the dynamic magneto-thermal simulation of magnetic devices. To increase the efficiency of magneto-thermal simulation, especially for a long-time magneto-thermal simulation, 1-D axisymmetric magneto-thermal circuit models are derived next.

7.3.2 1-D Axisymmetric Magneto-Thermal Subcircuits

To simplify the magneto-thermal circuit models for magnetic devices made of toroids, axisymmetric formulations are applied to develop 1-D axisymmetric magneto-thermal circuit models to account for the 2-D problems. Axisymmetric formulations are expressed in terms of cylindrical coordinates, i.e., r-θ coordinates for the 2-D problems. The basic hypothesis of axisymmetry is that all functions under consideration are independent of θ [Hug87]. For a 1-D linear finite-element shown in Fig. 7.4, the basis functions in the r-coordinate are expressed as

$$N_1 = \frac{r_1 - r}{r_1 - r_0}, N_2 = \frac{r - r_0}{r_1 - r_0} \tag{7.18}$$

Note that this 1-D linear finite-element actually represents a ring in the 2-D problems. We can express dS by $2\pi r dr$ in the expressions of the elemental components; and the integral

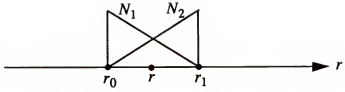

Figure 7.4 1-D linear finite-element

solutions for deriving the elemental circuit models are calculated as follows:

$$\int_S N_1 dS = \int_{r_0}^{r_1}\left(\frac{r_1 - r}{r_1 - r_0}\right)2\pi r dr = \frac{\pi(r_1 - r_0)(r_1 + 2r_0)}{3} \tag{7.19}$$

$$\int_S N_2 dS = \int_{r_0}^{r_1}\left(\frac{r - r_0}{r_1 - r_0}\right)2\pi r dr = \frac{\pi(r_1 - r_0)(2r_1 + r_0)}{3} \tag{7.20}$$

$$\int_S N_1 N_1 dS = \int_{r_0}^{r_1}\left(\frac{r_1 - r}{r_1 - r_0}\right)^2 2\pi r dr = \frac{\pi(r_1 - r_0)(r_1 + 3r_0)}{6} \tag{7.21}$$

$$\int_S N_1 N_2 dS = \int_{r_0}^{r_1}\left(\frac{r_1 - r}{r_1 - r_0}\right)\left(\frac{r - r_0}{r_1 - r_0}\right)2\pi r dr = \frac{\pi(r_1 - r_0)(r_1 + r_0)}{6} \tag{7.22}$$

$$\int_S N_2 N_2 dS = \int_{r_0}^{r_1}\left(\frac{r - r_0}{r_1 - r_0}\right)^2 2\pi r dr = \frac{\pi(r_1 - r_0)(3r_1 + r_0)}{6} \tag{7.23}$$

$$\int_S N_{i,x} N_{j,x} dS = \begin{cases} \dfrac{\pi(r_1 + r_0)}{r_1 - r_0} & \text{for } i = j \\ \dfrac{-\pi(r_1 + r_0)}{r_1 - r_0} & \text{for } i \neq j \end{cases} \tag{7.24}$$

$$\int_S dS = \pi(r_1^2 - r_0^2) \tag{7.25}$$

The elemental matrices for the magnetic (ferrite) elements are calculated to be

$$\boldsymbol{m}_e = \frac{\varepsilon\pi(r_1 - r_0)}{6}\begin{bmatrix} r_1 + 3r_0 & r_1 + r_0 \\ r_1 + r_0 & 3r_1 + r_0 \end{bmatrix}$$

$$\boldsymbol{b}_e = \frac{\sigma\pi(r_1 - r_0)}{6}\begin{bmatrix} r_1 + 3r_0 & r_1 + r_0 \\ r_1 + r_0 & 3r_1 + r_0 \end{bmatrix}$$

$$k_e = \frac{\nu_0 \pi (r_1 + r_0)}{r_1 - r_0} \begin{bmatrix} 1 & -1 \\ -1 & 1 \end{bmatrix} \tag{7.26}$$

and the nonlinear current components are derived as

$$I_M = \pi (r_1 + r_0) M \begin{bmatrix} 1 \\ -1 \end{bmatrix} \tag{7.27}$$

The elemental matrices for the thermal system by the axisymmetric formulations are calculated to be

$$m_e^d = \frac{\rho c_p \pi (r_1 - r_0)}{6} \begin{bmatrix} r_1 + 3r_0 & r_1 + r_0 \\ r_1 + r_0 & 3r_1 + r_0 \end{bmatrix}$$

$$k_e^d = \frac{\kappa \pi (r_1 + r_0)}{r_1 - r_0} \begin{bmatrix} 1 & -1 \\ -1 & 1 \end{bmatrix}$$

$$I^g = \frac{\pi (r_1 - r_0)}{3} \begin{bmatrix} r_1 + 2r_0 \\ 2r_1 + r_0 \end{bmatrix} \tag{7.28}$$

The 1-D axisymmetric magneto-thermal subcircuit for the magnetic (ferrite) elements is shown in Fig. 7.5(a), where

$$C_1 = \frac{\varepsilon \pi (r_1 - r_0)(r_1 + 2r_0)}{3}, \; C_{12} = \frac{-\varepsilon \pi (r_1 - r_0)(r_1 + r_0)}{6}$$

$$C_2 = \frac{\varepsilon \pi (r_1 - r_0)(2r_1 + r_0)}{3}, \; R_1 = \frac{3}{\sigma \pi (r_1 - r_0)(r_1 + 2r_0)}$$

$$R_{12} = \frac{-6}{\sigma \pi (r_1 - r_0)(r_1 + r_0)}, \; R_2 = \frac{3}{\sigma \pi (r_1 - r_0)(2r_1 + r_0)},$$

$$L_{12} = \frac{r_1 - r_0}{\nu_0 \pi (r_1 + r_0)}, \; I_{M1} = \pi (r_1 + r_0) M, \; I_{M2} = -\pi (r_1 + r_0) M \tag{7.29}$$

$$C_1^d = \frac{\rho c_p \pi (r_1 - r_0)(r_1 + 2r_0)}{3},\ C_{12}^d = \frac{-\rho c_p \pi (r_1 - r_0)(r_1 + r_0)}{6}$$

$$C_2^d = \frac{\rho c_p \pi (r_1 - r_0)(2r_1 + r_0)}{3},\ R^d = \frac{r_1 - r_0}{\kappa \pi (r_1 + r_0)}$$

$$I_1^g = \frac{g\pi (r_1 - r_0)(r_1 + 2r_0)}{3},\ I_2^g = \frac{g\pi (r_1 - r_0)(2r_1 + r_0)}{3} \tag{7.30}$$

There are two unknowns, i.e., $\dot{a}_i$ and d_i, in each elemental node of the magnetic (ferrite) elements. The elemental matrices for the conductive (copper) elements are calculated to be

$$\boldsymbol{m}_e = \frac{\varepsilon_0 \pi (r_1 - r_0)}{6} \begin{bmatrix} r_1 + 3r_0 & r_1 + r_0 & -2(r_1 + 2r_0) \\ r_1 + r_0 & 3r_1 + r_0 & -2(2r_1 + r_0) \\ -2(r_1 + 2r_0) & -2(2r_1 + r_0) & 6(r_1 + r_0) \end{bmatrix}$$

$$\boldsymbol{b}_e = \frac{\sigma \pi (r_1 - r_0)}{6} \begin{bmatrix} r_1 + 3r_0 & r_1 + r_0 & -2(r_1 + 2r_0) \\ r_1 + r_0 & 3r_1 + r_0 & -2(2r_1 + r_0) \\ -2(r_1 + 2r_0) & -2(2r_1 + r_0) & 6(r_1 + r_0) \end{bmatrix}$$

$$\boldsymbol{k}_e = \frac{\nu_0 \pi (r_1 + r_0)}{r_1 - r_0} \begin{bmatrix} 1 & -1 \\ -1 & 1 \end{bmatrix} \tag{7.31}$$

The elemental matrices for the insulating (air) elements are calculated to be

$$\boldsymbol{m}_e = \frac{\varepsilon_0 \pi (r_1 - r_0)}{6} \begin{bmatrix} r_1 + 3r_0 & r_1 + r_0 \\ r_1 + r_0 & 3r_1 + r_0 \end{bmatrix}$$

$$\boldsymbol{k}_e = \frac{\nu_0 \pi (r_1 + r_0)}{r_1 - r_0} \begin{bmatrix} 1 & -1 \\ -1 & 1 \end{bmatrix},\ \boldsymbol{b}_e = 0 \tag{7.32}$$

The 1-D axisymmetric subcircuits for the conductive (copper) and insulating (air) elements are shown in Fig. 7.5(b) and Fig. 7.5(c), respectively, where the expressions for

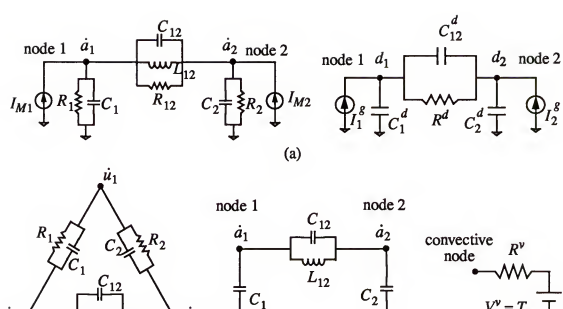

Figure 7.5 1-D axisymmetric magneto-thermal subcircuit for the magnetic (ferrite) elements (a); 1-D axisymmetric subcircuits for the conductive (copper) elements (b); for the insulating (air) elements (c); and 1-D convective thermal subcircuit (d).

the RLC components are the same as those shown in (7.29), except that ε is replaced by ε_0. The 1-D convective thermal subcircuit is shown in Fig. 7.5(d), where

$$R^v = \frac{1}{2\pi r_x h}, V^v = T_a = 300K \tag{7.33}$$

and $r_x = r_o$ (the outer radius) or $r_x = r_i$ (the inner radius). The subcircuit for the 1-D boundary infinite element, as shown in Fig. 7.3(d), is used to account for the boundary condition at infinity. For the axisymmetric formulations, the expressions of the circuit components for the 1-D boundary infinite element are changed to

$$C_1^b = \frac{-4l_c^2\pi\varepsilon_0}{3}, C_{12}^b = \frac{8l_c^2\pi\varepsilon_0}{3}, C_2^b = \frac{56l_c^2\pi\varepsilon_0}{3}$$

$$L_1^b = \frac{-3}{\nu_0\pi}, L_{12}^b = \frac{1}{4\nu_0\pi}, L_2^b = \frac{3}{4\nu_0\pi} \tag{7.34}$$

where we choose the origin of the x-y coordinates as the pole n_0 of the 1-D boundary infinite elements, and $l_c = r_0$. Note that a ring conductor was considered in the axisymmetric formulation for the 2-D problems. To account for the real area of one winding conductor, a small fitting parameter α can be used, i.e., the expressions of the components in the conductive (copper) subcircuit can be modified as

$$C_1 = \frac{\varepsilon\alpha\pi(r_1 - r_0)(r_1 + 2r_0)}{3},\ C_{12} = \frac{-\varepsilon\alpha\pi(r_1 - r_0)(r_1 + r_0)}{6}$$

$$C_2 = \frac{\varepsilon\alpha\pi(r_1 - r_0)(2r_1 + r_0)}{3},\ R_1 = \frac{3}{\sigma\alpha\pi(r_1 - r_0)(r_1 + 2r_0)}$$

$$R_{12} = \frac{-6}{\sigma\alpha\pi(r_1 - r_0)(r_1 + r_0)},\ R_2 = \frac{3}{\sigma\alpha\pi(r_1 - r_0)(2r_1 + r_0)}$$

$$L_{12} = \frac{r_1 - r_0}{\nu_0\alpha\pi(r_1 + r_0)} \tag{7.35}$$

Figure 7.6 shows a 2-D magneto-thermal problem which is simplified to a 1-D axisymmetric magneto-thermal problem for a transformer made of a toroid. The overall 1-D axisymmetric magneto-thermal circuit model is shown in Fig. 7.7, where n_1 and n_2 are the numbers of the primary and the secondary winding turns, respectively. The magneto-thermal circuit network is constructed by the subcircuits developed previously for the magneto-thermal system. The interface network connects the magneto-thermal circuit network to the external circuitry. Note that only one turn is considered in the 1-D axisymmetric formulation for both the primary and the secondary windings, and the actual numbers of turns are modeled in the interface network.

To include any hysteresis model in the 1-D axisymmetric finite-element analysis, the magnetic flux density in a magnetic (ferrite) subcircuit is derived as

$$B = \nabla\times A = -\left(\frac{\partial A_z}{\partial r}\right)\hat{\theta} = -[a_1 N_{1,r} + a_2 N_{2,r}]\hat{\theta}$$

$$= \left[\frac{a_1 - a_2}{r_1 - r_0}\right]\hat{\theta} = \left[\frac{I_{L12}}{\nu_0\pi(r_1 + r_0)}\right]\hat{\theta} \tag{7.36}$$

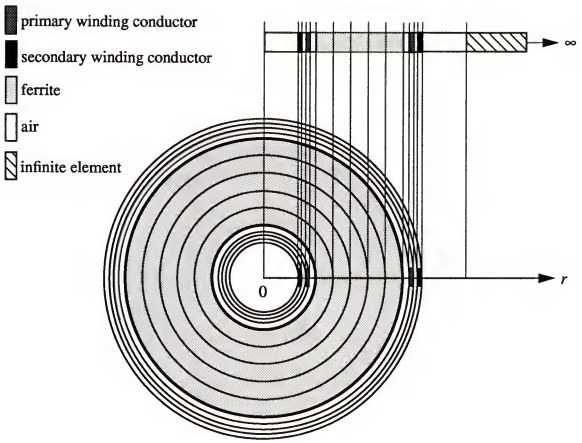

Figure 7.6 A 2-D magneto-thermal problem simplified to a 1-D axisymmetric magneto-thermal problem for a transformer made of a toroid.

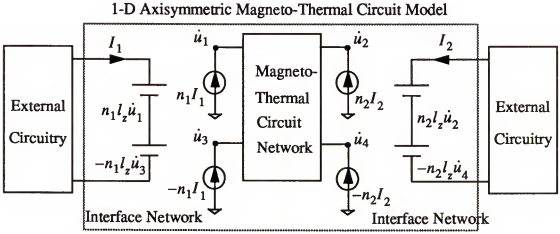

Figure 7.7 Configuration of the1-D axisymmetric magneto-thermal circuit model for a transformer made of a toroid.

where we use the following relation:

$$a_1 - a_2 = \frac{I_{L12}(r_1 - r_0)}{\nu_0 \pi (r_1 + r_0)} \tag{7.37}$$

which is derived from the elemental matrix equations. From (7.36), the magnetic flux density B is calculated from the inductor current I_{L12}, and the magnetic field H can be reversely calculated from B and any hysteresis model. The magnetization M is then obtained from B and H to formulate the nonlinear current components as derived in (7.27). These nonlinearly coupled unknowns in each magnetic (ferrite) subcircuit are solved simultaneously from the assembled global circuit model using the built-in numerical solver in SABER.

7.4 Evaluation of Internal Heat Generation

The total core losses consist of hysteresis, eddy-current, and anomalous losses. The eddy-current losses are Joule's effect losses due to induced currents. The anomalous losses are due to spin relaxation losses or domain relaxation losses [Gar94]. The hysteresis BH-loop area calculated from the static hysteresis model is usually called hysteresis energy loss. The BH-loop area calculated from the dynamic hysteresis model, however, takes into account all types of magnetic losses, i.e., hysteresis, eddy-current, and anomalous losses [Gar94].

7.4.1 Core Loss Density Averaged Over One Cycle

The hysteresis losses per unit volume averaged over one cycle is usually calculated from the formula [Vec82]:

$$P_{d,avg} = \frac{1}{T}\int_0^T \left(H \cdot \frac{\partial B}{\partial t}\right) dt = \frac{1}{T}\oint H \cdot dB \tag{7.38}$$

where T is the period of the excitation source. If the BH-loop is closed, (7.38) can be simply expressed as

$$P_{d,\,avg} = A_{BH-loop} \cdot f \tag{7.39}$$

where $A_{BH-loop}$ is the BH-loop area, and $f = 1/T$ is the operating frequency. Since we use an experimentally verified rate-dependent hysteresis model in each finite-element subcircuit, the total losses per unit volume averaged over one cycle, calculated from (7.38) or (7.39), should include the total effects of hysteresis, eddy-current, and anomalous losses.

Since the time constant of the thermal system is much larger than that of the magnetic system, it is a reasonable assumption to use the averaged core loss density calculated at the previous cycle as the averaged internal heat generation in the present cycle. This will only introduce a small error in the dynamic solutions of the thermal system. Thus, the internal heat generation g can be approximated by $P_{d,\,avg}$ in the magneto-thermal simulation.

7.4.2 Instantaneous Internal Heat Generation

To obtain more accurate simulation results for the dynamic magneto-thermal simulation of magnetic devices, instantaneous internal heat generations can be used. Using the instantaneous internal heat generations, the following problems or errors can be avoided: a) if the BH-loop is not closed for each minor loop; and b) if the operating frequency is unknown or consists of several harmonic components.

The instantaneous core loss density can be calculated from

$$P_d = H \cdot \frac{\partial B}{\partial t} \tag{7.40}$$

P_d in (7.40), however, is not the real instantaneous internal heat generation, for it consists of both the reactive part and the dissipated part. The reactive part is a pure sinusoidal waveform, and has no contributions to the internal heat generation. The dissipated part is

always positive, and causes the internal heat generation. Thus, to find the instantaneous internal heat generation, we need to find a way to separate the reactive part and the dissipated part in P_d.

P_d in (7.40) can be separated into two components as follows:

$$P_d = H \cdot \frac{\partial}{\partial t}(B - B_{reactive}) + H \cdot \frac{\partial B_{reactive}}{\partial t} \tag{7.41}$$

where the first component is the dissipated part which results in the internal heat generation, and the second component is the reactive part. The internal heat generation in magnetic devices is mainly due to the energy lost to pinning in the domain wall motion, which is due to the irreversible magnetization B_{irr}; thus, we may approximate the reactive flux density $B_{reactive}$ by the reversible flux density B_{rev}, and approximate the instantaneous internal heat generation g as

$$g \approx H \frac{\partial B_{irr}}{\partial t} \tag{7.42}$$

7.5 Simulation and Verification

To verify the developed finite-element magneto-thermal circuit models, a transformer made of Philips 768T188-3C85 toroid, with 18 turns of primary windings and 18 turns of secondary windings, is simulated in the SABER circuit simulator. The 1-D axisymmetric meshes for the toroid is shown in Fig. 7.6, and 20 elements are used in the simulation, i.e., five elements for the ferrite, eight elements for the copper (with two elements in each conductor), six elements for the air, and one boundary infinite element. A simple test circuit as shown in Fig. 6.13 for the core-loss measurement is simulated; and the applied voltage is a sinusoidal waveform with $V_m = 20$V and $f = 10$kHz. The material properties used in the simulation are: $\varepsilon = 1.9\text{x}10^5\varepsilon_0$, $\sigma = 0.625/(\Omega\text{-}m)$ for the ferrite; $\varepsilon = \varepsilon_0$, $\sigma = 5.8\text{x}10^7/(\Omega\text{-}m)$, $\nu = \nu_0$ for the copper; and $\varepsilon = \varepsilon_0$, $\sigma = 0$, $\nu = \nu_0$ for the air. Note that the reluctivity (or permeability) for the ferrite is implied in the rate-dependent and temperature-dependent hysteresis model. The thermal properties for the MnZn ferrite

obtained from data books are: thermal conductivity $\kappa \approx 4\,W/(m\text{-}K)$, specific heat $c_p \approx 1.1\,J/(g\text{-}K)$, and mass density $\rho \approx 4.7\text{x}10^6\,g/m^3$. In the simulation, the internal heat generation in each ferrite element is approximated by the core loss density averaged over one cycle.

The convective coefficient h can be extracted from the DC thermal network using the measured steady-state temperature and the core loss densities (at the steady-state temperature) in the ferrite elements. The core loss densities can be obtained from a magnetic simulation at the steady-state temperature, or can be estimated from data books based on the operating conditions. The convective coefficient h is extracted to be $11.2W/(m^2\text{-}K)$.

To verify the developed axisymmetric magneto-thermal subcircuits, the simulated magnetic field H and magnetic flux density B at the beginning of the transient (0 ~ 400us) in the five ferrite elements are compared with the experimental data in Fig. 7.8 and Fig. 7.9, respectively. Note that the experimental H and B are calculated from the experimental current and voltage waveforms using effective magnetic flux path and cross-sectional area; thus, the experimental H and B are close to those in the third (middle) ferrite element as expected. It is also seen that the simulated H in the ferrite element closest to the outer radius of the toroid is the smallest, as can be predicted from the Ampere's law. Since the magnetizing transient is not captured by the oscilloscope, the experimental H and B are only compared with the simulated results after the first cycle.

Because the time constant of the thermal system is much larger than that of the magnetic system, the computation takes long simulation time and huge disk space for the temperature to go steady. To avoid the difficulty found in the long-time magneto-thermal simulation, an iterative process is applied to obtain the steady-state nodal temperatures. The iterative process is summarized as follows: (1) a full magneto-thermal simulation is performed over a certain time (1ms) to determine the averaged internal heat generation in each ferrite element; (2) a DC simulation of the thermal system with the determined internal heat generations is then performed to estimate the steady-state nodal temperatures; (3) the steady-state nodal temperatures are used as initial conditions for

another full magneto-thermal simulation to determine the averaged internal heat generation in each ferrite element. The process is repeated until the temperatures and the averaged internal heat generations converge to steady-states.

The process converges after four iterations. Using the extracted convective coefficient $h \approx 11.2\, W/(m^2\text{-}K)$, the converged steady-state temperature at the outer radius of the toroid is close to the measured steady-state temperature 328K. To estimate the time constant of the thermal system inside the magnetic device, the converged internal heat generations in the ferrite elements are applied for a transient thermal simulation. As shown in Fig. 7.10, it takes about 2400 seconds for the temperature to go steady. Because of the small time constant of the magnetic system and because of the nonlinear hysteresis model in each ferrite element, it takes about one hour for the magneto-thermal simulation to go as far as 0.5 second. Based on the same simulation speed, it will take 4800 hours simulation time for the temperature to go steady. To avoid this problem, the iterative process as discussed above is needed for estimating the steady-state temperatures.

Two important tasks in the high-frequency magnetic designs are: a) determine the magnetizing transients so that the inrush of the magnetizing current is not too large; and b) assure that the steady-state core temperature does not exceed the Curie temperature. Using the developed magneto-thermal circuit models and the iterative process, both the magnetizing transient and the steady-state core temperature can be accurately simulated.

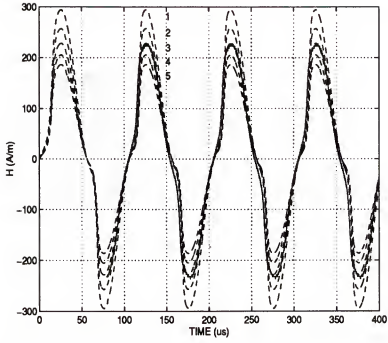

Figure 7.8 Comparison of the simulated H in the five ferrite elements with the experimental H calculated from the experimental current and the mean flux path; solid line: experimental H; dashed line: simulated H.

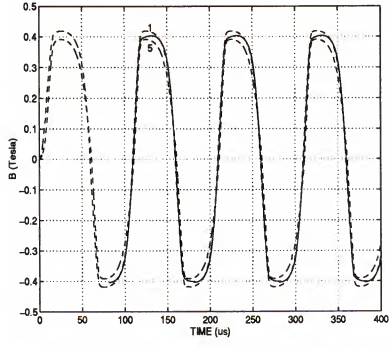

Figure 7.9 Comparison of the simulated B in the first and fifth ferrite elements with the experimental B calculated from the experimental voltage and the mean cross-sectional area; solid line: experimental B; dashed line: simulated B.

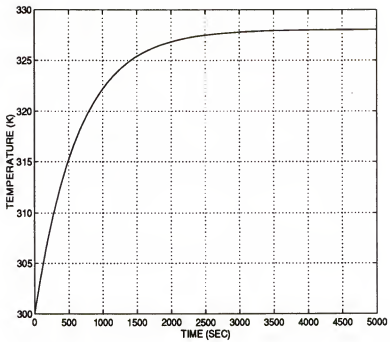

Figure 7.10 Simulated core temperature from a transient thermal simulation using the converged internal heat generations in the ferrite elements.

7.6 Summary

The finite-element magnetic and thermal circuit models, as well as the rate-dependent and temperature-dependent hysteresis model, have been combined to build the 2-D finite-element magneto-thermal circuit models. To increase the efficiency of magneto-thermal simulation, axisymmetric formulations are also applied to develop 1-D axisymmetric magneto-thermal circuit models for magnetic devices made of toroids. Using these circuit models, both the magnetic and the thermal transient phenomena in the magnetic devices can be simulated using existing circuit simulators. To reduce the simulation time, an iterative process has also been applied to determine the steady-state core temperatures.

CHAPTER 8
CONCLUSION AND FUTURE WORK

8.1 Conclusion

A new technique to formulate finite-element-based thermal circuit models has been developed. Different types of finite-elements are modeled as different types of lumped thermal circuit components, so that finite-element solutions of the thermal system are ready to be coupled with those of the electrical system in the electro-thermal simulation. This new technique can be generalized to formulate circuit models for any partial differential equations describing physical systems. The modeling methodology allows electrical engineers to obtain finite-element solutions for any partial differential equation using existing circuit simulators.

Several model reduction techniques have been discussed and applied to formulate reduced thermal circuit models, which increase the simulation speed while maintaining good accuracy. The modeling methodology may be generalized to build reduced models for any large linear systems. For example, the modeling methodology may be applied to build reduced circuit models for the interconnect circuit simulation.

Methodologies have been presented for efficient modeling of power semiconductor devices. The developed behavioral IGBT and VDMOS models give satisfactory simulation results for various test circuits in terms of efficiency and accuracy. It is believed that several linear and nonlinear system identification theories discussed in the literature can be applied to simplify the solutions from the semiconductor equations, so that efficient physics-based semiconductor device models can be obtained.

A rate-dependent and temperature-dependent hysteresis model, which consists of both the reversible and the irreversible components of magnetization, has been developed. The proposed model structure provides an efficient way to incorporate the rate-dependent and temperature-dependent effects of the hysteresis phenomena into the classical Preisach model. To modify the classical Preisach model, two approaches have been applied to include the reversible magnetization. The proposed hysteresis model gives satisfactory simulation results, and can be applied for magneto-thermal simulation.

Field-based finite-element circuit models, which could take into account the hysteresis, geometry, frequency, large-signal, and waveshape effects, have been developed and applied to model the magnetic components. The field-based circuit modeling methodology allows the users of circuit simulators to perform finite-element simulation of magnetic devices coupled with a wide range of circuit topologies in the circuit simulators. A new finite-element/circuit formulation has also been presented to include any kind of hysteresis models in the finite-element analysis of magnetic devices.

Field-based finite-element magneto-thermal circuit models have been developed. The 2-D triangular thermal circuit models developed in Chapter 2, the rate-dependent and temperature-dependent hysteresis model developed in Chapter 5, and the field-based finite-element magnetic circuit models developed in Chapter 6, have been combined to build 2-D finite-element magneto-thermal circuit models. To increase the efficiency of magneto-thermal simulation, axisymmetric formulations have also been applied to develop 1-D axisymmetric finite-element magneto-thermal circuit models for magnetic devices made of toroids. Using these models, both the magnetic and the thermal transient phenomena in the magnetic devices can be predicted. The designed high-frequency magnetic devices can be synthesized with adequate degree of accuracy before manufacturing, thus potentially reducing the manufacturing cost.

8.2 Future Work

Several research directions are recommended and discussed here for the extension of this research work.

One research direction is to find reduced nonlinear models for the nonlinear thermal systems for electro-thermal simulation. A possible approach is to apply the Hammerstein model to build reduced nonlinear thermal models. For example, random signals can be applied as the input power to the thermal system, which is discretized either by a finite-element mesh of by a finite-difference mesh. Then the transient nodal temperatures which are concerned can be solved by the finite-element method or finite-difference method. Using the calculated nodal temperatures as outputs, and the applied random signals as inputs, the parameters in the Hammerstein model may be extracted by several system identification procedures discussed in the literature [Nar66, Bil79, Gre89, Fal91, Bil80, Gal75, Esk91, Krz93].

The other research direction is to build reduced circuit models for the magnetic devices for efficient circuit simulation. Both Modal Superposition method and Component Mode Synthesis method may be applied to build reduced linear magnetic models. This modeling methodology will be very useful for modeling the integrated magnetics which consist of several magnetic components in the same ferrite plate, because it is very difficult to find analytical lumped models which could account for the coupling effects among different magnetic components in the same ferrite plate. Multi-Input Multi-Output Hammerstein models may be applied to build reduced nonlinear magnetic models, which take into account the hysteresis phenomena.

Another research direction is model reduction for the coupled magneto-thermal systems. To achieve efficient magneto-thermal simulation, one way is to find reduced magneto-thermal circuit models, the other way is to find efficient numerical algorithms for solving the coupled magnetic and thermal systems.

APPENDIX
LEAST-SQUARES METHODS

A.1 Least-Squares Method for Polynomial Fitting

For an input sequence $u(i)$ and an output sequence $y(i)$, the output sequence $y(i)$ can be approximated by a polynomial function of the input sequence $u(i)$ as

$$y(i) \approx \tilde{y}(i) \equiv \sum_{j=1}^{M} r_j [u(i)]^{j-1} \tag{A.1}$$

and the error sequence $e(i)$ between $y(i)$ and $\tilde{y}(i)$ is defined as

$$e(i) \equiv y(i) - \tilde{y}(i) \tag{A.2}$$

If there are N data points in the sequence, (A.1) and (A.2) can be written as

$$\begin{bmatrix} y(1) \\ y(2) \\ \vdots \\ y(N) \end{bmatrix} = \begin{bmatrix} 1 & u(1) & [u(1)]^2 & .. & [u(1)]^{M-1} \\ 1 & u(2) & [u(2)]^2 & .. & [u(2)]^{M-1} \\ \vdots & \vdots & \vdots & \vdots & \vdots \\ 1 & u(N) & [u(N)]^2 & .. & [u(N)]^{M-1} \end{bmatrix} \begin{bmatrix} r_1 \\ r_2 \\ \vdots \\ r_M \end{bmatrix} + \begin{bmatrix} e(1) \\ e(2) \\ \vdots \\ e(N) \end{bmatrix} \tag{A.3}$$

or in the following form

$$Y = \Psi R + E \tag{A.4}$$

The least squares estimate of the coefficient vector,

$$R \approx \tilde{R} = [\tilde{r}_1 \;\; \tilde{r}_2 \;\; \ldots \;\; \tilde{r}_M]^T \tag{A.5}$$

can be readily computed as

$$\tilde{R} = [\Psi^T\Psi]^{-1}\Psi^T Y \tag{A.6}$$

A.2 Levenberg-Marquardt Method [Pre92]

The output sequence $y(i)$ sometimes can be approximated by a nonlinear function of the input sequence $u(i)$ as

$$y(i) \approx \tilde{y}(i) \equiv \tilde{y}(u(i);R) \tag{A.7}$$

and a merit function can be defined as

$$\chi^2(R) \equiv \sum_{i=1}^{N} [y(i) - \tilde{y}(u(i);R)]^2 \tag{A.8}$$

where $R = [r_1 \ r_2 \ \dots \ r_M]^T$ is the coefficient vector to be estimated, and N the number of data points. The best estimate of R is obtained by minimizing the merit function $\chi^2(R)$, which can be approximated by

$$\chi^2(R) \approx \frac{1}{2} R \cdot A \cdot R - b \cdot R + c \tag{A.9}$$

where A is the Hessian matrix with $A_{ij} = \frac{\partial^2 \chi^2}{\partial r_i \partial r_j}$, b is a vector, and c is a constant. The derivative of χ^2 with respect to R is expressed as

$$\nabla\chi^2(R) = A \cdot R - b \tag{A.10}$$

The minimum point R_m (in M dimension) satisfies

$$A \cdot R_m = b \tag{A.11}$$

and at any point R_j, whatever it is, satisfies

$$A \cdot R_j = \nabla\chi^2(R_j) + b \tag{A.12}$$

The previous two equations yield

$$A \cdot \delta R \equiv A \cdot (R_m - R_j) = -\nabla\chi^2(R_j) \tag{A.13}$$

where δR is the incremental coefficient vector for the next iteration approaching the minimum point R_m. Define the elements of a matrix α and a vector β as follows:

$$\alpha_{jk} \equiv \frac{1}{2}\frac{\partial^2\chi^2}{\partial r_j \partial r_k} = \sum_{i=1}^{N} \left\{ \frac{\partial\tilde{y}(u(i);R)}{\partial r_j}\frac{\partial\tilde{y}(u(i);R)}{\partial r_k} - [y(i) - \tilde{y}(u(i);R)]\frac{\partial^2}{\partial r_j \partial r_k}\tilde{y}(u(i);R) \right\} \tag{A.14}$$

$$\beta_j \equiv -\frac{1}{2}\frac{\partial\chi^2}{\partial r_j} = \sum_{i=1}^{N} [y(i) - \tilde{y}(u(i);R)]\frac{\partial\tilde{y}(u(i);R)}{\partial r_j} \tag{A.15}$$

It is seen that $\alpha = \frac{1}{2}A$ and $\beta = -\frac{1}{2}\nabla\chi^2$. Equation (A.13) can be written as

$$\alpha \cdot \delta R = \beta \tag{A.16}$$

from which the incremental coefficient vector δR is calculated. By replacing R by $R + \delta R$, the iteration continues until R converges to a reasonable precision. In the Levenberg-Marquardt method, the mathematics is further simplified. The second derivative term in (A.14) is neglected, i.e., (A.14) is replaced by

$$\alpha_{jk} = \sum_{i=1}^{N} \left[\frac{\partial\tilde{y}(u(i);R)}{\partial r_j}\frac{\partial\tilde{y}(u(i);R)}{\partial r_k} \right] \tag{A.17}$$

and a new matrix $\tilde{\alpha}$ is defined according to

$$\tilde{\alpha}_{jj} \equiv \alpha_{jj}(1+\lambda)$$

$$\tilde{\alpha}_{jk} \equiv \alpha_{jk} \quad \text{for} \quad j \neq k \tag{A.18}$$

where λ is a scaling factor in the iterative algorithm. When λ is very large, the method is close to the steepest descent method; and when λ approaches zero, the method is close to the inverse-Hessian method [Pre92]. The incremental coefficient vector δR in the Levenberg-Marquardt method is solved from

$$\tilde{\alpha} \cdot \delta R = \beta \tag{A.19}$$

The algorithm of the Levenberg-Marquardt method is summarized as follows:

Initial state:

Solve $\chi^2(R)$ from an initial guess of R; pick a modest value for λ, say $\lambda = 0.001$.

Iterative state:

(*) Solve δR from (A.19) (update $\tilde{\alpha}$ and β if necessary), and evaluate $\chi^2(R+\delta R)$.

do while $|\chi^2(R+\delta R) - \chi^2(R)| > \varepsilon$

if $\chi^2(R+\delta R) \geq \chi^2(R)$

increase λ by a factor of 10 (or any substantial factor) and go back to (*)

elseif $\chi^2(R+\delta R) < \chi^2(R)$

decrease λ by a factor of 10, update the trial solution $R \leftarrow R + \delta R$, and go back to (*)

end

end

The algorithm is stopped when $|\chi^2(R+\delta R) - \chi^2(R)| < \varepsilon$, for a change in R that changes χ^2 by an amount $\varepsilon << 1$ is not statistically meaningful.

REFERENCES

[Ana92] D. F. Anastasakis, N. Gopal, S. Y. Kim, and L. T. Pillage, "On the Stability of Moment-Matching Approximations in Asymptotic Waveform Evaluation," *ACM/IEEE Design Automation Conference Record*, Anaheim, California, 1992, pp. 207-212.

[Arn85] R. R. Arnold and R. L. Citerley, "Application of Ritz Vectors for Dynamic Analysis of Large Structures," *Computers and Structures*, Vol. 21, No. 5, pp. 901-907, 1985.

[Ath87] D. L. Atherton, B. Szpunar, and J. A. Szpunar, "A New Approach to Preisach Diagrams," *IEEE Transactions on Magnetics*, Vol. 23, No. 3, pp. 1856-1865, May 1987.

[Bar77] J. J. Barnes and R. J. Lomax, "Finite Element Methods in Semiconductor Device Simulation," *IEEE Transactions on Electron-Devices*, Vol. ED-34, No. 8, pp. 1082-1088, August 1977.

[Ben71] W. A. Benfield and R. F. Hruda, "Vibration Analysis of Structures by Component Mode Substitution," *AIAA Journal*, Vol. 9, No. 7, pp. 1255-1261, July 1971.

[Ben91] J. K. Bennighof and J. Y. Wu, "Parallel Transient Algorithm with Multistep Substructure Computation," *AIAA Journal*, Vol. 29, No. 6, pp. 984-991, June 1991.

[Ber92] G. Bertotti, "Dynamic Generalization of Scalar Preisach Model of Hysteresis," *IEEE Transactions on Magnetics*, Vol. 28, No. 5, pp. 2599-2601, September 1992.

[Bil79] S. A. Billings and S. Y. Fakhouri, "Nonlinear System Identification Using the Hammerstein Model," *International Journal of Systems Sciences*, Vol. 10, No. 5, pp. 567-578, 1979.

[Bil80] S. A. Billings, "Identification of Nonlinear Systems--A Survey," *IEE Proceedings*, Vol. 127, Pt. D, No. 6, pp. 272-285, November 1980.

[Bra91] J. R. Brauer, B. E. MacNeal, L. A. Larkin, and V. D. Overbye, "New Method of Modeling Electronic Circuits Coupled with 3-D Electromagnetic Finite Element Models," *IEEE Transactions on Magnetics*, Vol. 27, No. 5, pp. 4085-4088, September 1991.

[Bud94] I. Budihardjo, P. O. Lauritzen, and H. A. Mantooth, "Performance Requirements for Power MOSFET Models," *IEEE Power Electronics Specialists Conference Record*, Taipei, Taiwan, 1994, pp. 69-76.

[Cha91] J. H. Chan et al., "Nonlinear Transformer Model for Circuit Simulation," *IEEE Transactions on Computer-Aided Design*, Vol. 10, No. 4, pp. 476-482, April 1991.

[Cha92] T. F. Chan and D. Goovaerts, "On the Relationship between Overlapping and Nonoverlapping Domain Decomposition Methods," *SIAM Journal of Matrix Analysis Applications*, Vol. 13, No. 2, pp. 663-670, April 1992.

[Cha94] C. Chaboudez et al., "Numerical Modeling of Induction Heating of Long Workpieces," *IEEE Transactions on Magnetics*, Vol. 30, No. 6, pp. 5028-5037, November 1994.

[Chi92] E. Chiprout and M. Nakhla, "Generalized Moment-Matching Methods for Transient Analysis of Interconnect Networks," *ACM/IEEE Design Automation Conference Record*, Anaheim, California, 1992, pp. 202-206.

[Coo89] R. D. Cook, D. S. Malkus, and M. E. Plesha, *Concepts and Applications of Finite Element Analysis*, Third Edition, John Wiley & Sons, New York, 1989.

[Cra68] R. R. Craig, "Coupling of Substructures for Dynamic Analysis," *AIAA Journal*, Vol. 6, No. 7, pp. 1313-1319, July 1968.

[Cra85] R. R. Craig, "A Review of Time-Domain and Frequency-Domain Component Mode Synthesis Method," *Combined experimental/analytical modeling for dynamic structural systems, AMD, ASME*, Vol. 67, pp. 1-30, 1985.

[Cra88] R. R. Craig and A. L. Hale, "Block-Krylov Component Synthesis Method for Structural Model Reduction," *Journal of Guidance, Control, and Dynamics*, Vol. 11, No. 6, pp. 562-570, Nov. - Dec. 1988.

[Dau90] R. Dautray and J. L. Lions, *Mathematical Analysis and Numerical Methods for Science and Technology*, Springer-Verlag, New York, 1990.

[Dea94] J. H. B. Deane, "Modeling the Dynamics of Nonlinear Inductor Circuits," *IEEE Transactions on Magnetics*, Vol. 30, No. 5, pp. 2795-2801, September 1994.

[Del94] F. Delince et al, "Influence of Hysteresis on the Behaviour of Coupled Finite Element - Electric Circuit Models," *IEEE Transactions on Magnetics*, Vol. 30, No. 5, pp. 3383-3386, September 1994.

[Dem92] A. Demenko, "Equivalent RC Network with Mutual Capacitances for Electromagnetic Field Simulation of Electrical Machine Transients," *IEEE Transactions on Magnetics*, Vol. 28, No. 2, pp. 1406-1409, March 1992.

[Dow72] E. H. Dowell, "Free Vibration of an Arbitrary Structure in terms of Components Modes," *Journal of Applied Mechanics*, Vol. 39, pp. 727-732, 1972.

[Edg89] R. S. Edgar, *Field Analysis and Potential Theory*, Lecture Notes in Engineering, Vol. 44, edited by C. A. Brebbia and S. A. Orszag, Springer-Verlag, New York, 1989

[Esk91] E. Eskinat, S. H. Johnson, and W. L. Luyben, "Use of Hammerstein Models in Identification of Nonlinear Systems," *AIChE Journal*, Vol. 37, No. 2, pp. 255-268, 1991.

[Eve54] D. H. Everett, "A General Approach to Hysteresis--Part 3: A Formal Treatment of the Independent Domain Model of Hysteresis," *Trans. Faraday Soc.*, Vol. 50, pp. 1077-1096, 1954.

[Eve55] D. H. Everett, "A General Approach to Hysteresis Part 4 - An Alternative Formulation of the Domain Model," *Trans. Faraday Soc.*, Vol. 51, pp. 1551-1557, 1955.

[Ewi93] R. E. Ewing, R. D. Lazarov, J. E. Pasciak, and P. S. Vassilevski, "Domain Decomposition Type Iterative Techniques for Parabolic Problems on Locally Refined Grids," *SIAM Journal of Numerical Analysis*, Vol. 30, No. 6, pp. 1537-1557, December 1993.

[Fal91] A. H. Falkner, "Identification of the System Comprising Parallel Hammerstein Branches," *International Journal of Systems Sciences*, Vol. 22, No. 11, pp. 2079-2087, 1991.

[Far92] C. Farhat and M. Geradin, "A Hybrid Formulation of a Component Mode Synthesis Method," *in 33rd AIAA/ASME/AHS/ASC Structures, Structural Dynamics and Materials Conference*, University of Colorado, Boulder, AIAA-92-2383-CP, pp. 1783-1796, April 1992.

[Fat93] B. Fatemizadeh and D. Silber, "A Versatile Electrical Model for IGBT Including Thermal Effects," *IEEE Power Electronics Specialists Conference Record*, University of Washington, Seattle, 1993, pp. 85-92.

[Fos88] J. G. Fossum and R. J. McDonald, "Network Representations of LIGBT Structures for CAD of Power Integrated Circuits," *IEEE Transactions on Electron Devices*, Vol. 35, No. 4, pp. 507-514, April 1988.

[Fuk76] K. Fukahori and P. R. Gray, "Computer Simulation of Integrated Circuits in the Presence of Electrothermal Interaction," *IEEE Transactions on Solid-State Circuits*, Vol. SC-11, No. 6, pp. 834-846, December 1976.

[Gal75] P. G. Gallman, "An Iterative Method for the Identification of Nonlinear Systems Using a Uryson Model," *IEEE Transactions on Automatic Control*, pp. 771-775, December 1975.

[Gar87] V. K. Garg et al., "Magneto-Thermal Coupled Finite Element Calculations in Multiconductor Systems," *IEEE Transactions on Magnetics*, Vol. MAG-23, No. 5, pp. 3296-3298, September 1987.

[Gar94] J. R. Garcia et al., "A Method for Calculating the Workpiece Power Dissipation in Induction Heating Processes," *IEEE Applied Power Electronics Conference Record*, Orlando, Florida, 1994, pp. 302-307.

[Gol69] R. L. Goldman, "Vibration Analysis by Dynamic Partitioning," *AIAA Journal*, Vol. 7, No. 6, pp. 1152-1154, June 1969.

[Gre89] W. Greblicki and M. Pawlak, "Nonparametric Identification of Hammerstein Systems," *IEEE Transactions on Information Theory*, Vol. 35, No. 2, pp. 409-418, 1989.

[Han95] P. Han et al., "Finite Element Method for Ferrite Coreloss Calculation," *IEEE Applied Power Electronics Conference Record*, Dallas, Texas, 1995, pp. 348-353.

[Hee92] H. Heeb and A. E. Ruehli, "Three-Dimensional Interconnect Analysis Using Partial Elemental Equivalent Circuits," *IEEE Transactions on Circuits and Systems*, Vol. 39, No. 11, pp. 974-982, November 1992.

[Hef88] A. R. Hefner, Jr. and D. L. Blackburn, "An Analytical Model for the Steady-State and Transient Characteristics of the Power Insulated-Gate Bipolar Transistor," *IEEE Transactions on Solid-State Electronics*, Vol. 31, No. 10, pp. 1513-1532, 1988.

[Hef91] A. R. Hefner and D. M. Diebolt, "An Experimentally Verified IGBT Model Implemented in the Saber Circuit Simulator," *IEEE Power Electronics Specialists Conference Record*, Massachusetts Institute of Technology, Cambridge, 1991, pp. 10-19.

[Hef93] A. R. Hefner and D. L. Blackburn, "Simulating the Dynamic Electro-Thermal Behavioral of Power Electronic Circuits and Systems," *IEEE Transactions on Power Electronics*, Vol. 8, No. 4, pp. 376-385, October 1993.

[Hei91] R. H. V. Heiden, A. A. Arkadan, J. R. Brauer, and G. T. Hummert, "Finite Element Modeling of a Transformer Feeding a Rectified Load: The Coupled Power Electronics and Nonlinear Magnetic Field Problem," *IEEE Transactions on Magnetics*, Vol. 27, No. 6, pp. 5217-5219, November 1991.

[Hin75] R. M. Hintz, "Analytical Method in Component Modal Synthesis," *AIAA Journal*, Vol. 13, No. 8, pp. 1007-1016, August 1975.

[Ho75] C. W. Ho, A. E. Ruehli, and P. A. Brennan, "The Modified Nodal Approach to Network Analysis," *IEEE Transactions on Circuits and Systems*, Vol. CAS-22, No. 6, pp. 504-509, June 1975.

[Hou69] S. N. Hou, "Review of Modal Synthesis Techniques and a New Approach," *Shock and Vibration Bulletin*, Vol. 40, No. 4, pp. 25-30, 1969.

[Hsu94] J. T. Hsu and L. Vu-Quoc, "A Rational Formulation of Thermal Circuit Models for Electro-Thermal Simulation by Finite Element Method and Model Reduction Techniques, " *IEEE 4th Workshop on Computers in Power Electronics Conference Record*, University of Quebec, Canada, 1994, pp. 67-72.

[Hsu95a] J. T. Hsu and K. D. T. Ngo, "A Behavioral Model of the IGBT for Circuit Simulation," *IEEE Power Electronics Specialists Conference Record*, Atlanta, Georgia, 1995, pp. 865-871.

[Hsu95b] J. T. Hsu and K. D. T. Ngo, "Behavioral Modeling of the IGBT Using the Hammerstein Configuration," submitted for review.

[Hsu95c] J. T. Hsu and L. Vu-Quoc, "A Rational Formulation of Thermal Circuit Models for Electro-Thermal Simulation--Part I: Finite Element Method," accepted by *IEEE Transactions on Circuits and Systems*, 1995.

[Hsu95d] J. T. Hsu and L. Vu-Quoc, "A Rational Formulation of Thermal Circuit Models for Electro-Thermal Simulation--Part II: Model Reduction Techniques," accepted by *IEEE Transactions on Circuits and Systems*, 1995.

[Hsu96] J. T. Hsu and K. D. T. Ngo, "Field-Based Finite-Element Circuit Models for Magnetic Components with Hysteresis," accepted by *IEEE Applied Power Electronics Conference*, San Jose, California, 1996.

[Hug87] T. J. R. Hughes, *The Finite Element Method*, Prentice Hall, Englewood Cliffs, New Jersey, 1987.

[Hui94] S. Y. R. Hui and J. Zhu, "Magnetic Hysteresis Modeling and Simulation Using the Preisach's Theory and TLM Technique," *IEEE Power Electronics Specialists Conference Record*, Taipei, Taiwan, 1994, pp. 837-842.

[Hur65] W. C. Hurty, "Dynamic Analysis of Structural Systems Using Component Modes," *AIAA Journal*, Vol. 3, No. 4, pp. 678-685, April 1965.

[Huy83] P. S. Huyakorn and G. F. Pinder, *Computational Methods in Subsurface Flow*, Academic Press, New York, 1983.

[Jil86] D. C. Jiles and D. L. Atherton, "Theory of Ferromagnetic Hysteresis," *Journal of Magnetism and Magnetic Materials*, Vol. 61, pp. 48-60, 1986.

[Jil89] D. C. Jiles and J. B. Thoelke, "Theory of Ferromagnetic Hysteresis: Determination of Model Parameters from Experimental Hysteresis Loops," *IEEE Transactions on Magnetics*, Vol. 25, No. 5, pp. 3928-3930, September 1989.

[Jil91] D. C. Jiles, *Introduction to Magnetism and Magnetic Materials*, Chapman and Hall, New York, 1991.

[Jil92] D. C. Jiles, J. B. Thoelke, and M. K. Devine, "Numerical Determination of Hysteresis Parameters for the Modeling of Magnetic Properties Using the Theory of Ferromagnetic Hysteresis," *IEEE Transactions on Magnetics*, Vol. 28, No. 1, pp. 27-35, Jan. 1992.

[Jil93] D. C. Jiles, "Frequency Dependence of Hysteresis Curves in Non-Conducting Magnetic Materials," *IEEE Transactions on Magnetics*, Vol. 29, No. 6, pp. 3490-3492, November 1993.

[Kik87] M. Kikuta, H. Togoh, and M. Tanaka, "Boundary Element Analysis of Nonlinear Transient Heat Conduction Problems Consisting of Subdomains with Different Properties," in Masataka Tanaka and Qing Hua Du, editors, *Theory and Applications of Boundary Element Method*, Pergamon Press, New York, 1987.

[Kim90] Y. K. Kim and J. G. Fossum, "Physical DMOST Modeling for High-Voltage IC CAD," *IEEE Transactions on Electron Devices*, Vol. 37, No. 3, pp. 797-803, March 1990.

[Kim93] H. S. Kim et al., "Parameter Extraction for the Static and Dynamic Model of IGBT," *IEEE Power Electronics Specialists Conference Record*, University of Washington, Seattle, 1993, pp. 71-74.

[Kok76] P. V. Kokotovic, R. E. O'Malley, and P. Sannuti, "Singular Perturbations and Order Reduction in Control Theory--An Overview," *Automatica*, Vol. 12, pp. 123-132, 1976.

[Krz93] A. Krzyzak, "Identification of Nonlinear Systems by Recursive Kernel Regression Estimates," *International Journal of Systems Sciences*, Vol. 24, No. 3, pp. 577-598, 1993.

[Kub82] K. Kubomura, "A Theory of Substructure Modal Synthesis," *Journal of Applied Mechanics*, Vol. 49, pp. 903-909, December 1982.

[Kuh74] E. J. Kuhar and C. V. Stahle, "Dynamic Transformation Method for Modal Synthesis," *AIAA Journal*, Vol. 12, No. 5, pp. 672-678, May 1974.

[Kuo86] D. S. Kuo and C. Hu, "An Analytical Model for the Power Bipolar-MOS Transistor," *IEEE Transactions on Solid-State Electronics*, Vol. 29, No. 12, pp. 1229-1237, 1986.

[Kuw87] T. Kuwahara and T. Takeda, "A Formula of Boundary Integral for Potential Problem and its Consideration," in Masataka Tanaka and Qing Hua Du, editors, *Theory and Applications of Boundary Element Method*, Pergamon Press, New York, 1987.

[Lau90] P. O. Lauritzen, "Power Semiconductor Device Models for Use in Circuit Simulators," *IEEE IAS Conference Record*, Seattle, 1990, pp. 1559-1563.

[Lav83] J. D. Lavers, "Numerical Solution Methods for Electroheat Problems," *IEEE Transactions on Magnetics*, Vol. MAG-19, No. 6, pp. 2566-2572, 1983.

[Lee85] K. Lee and S. B. Park, "Reduced Modified Nodal Approach to Circuit Analysis," *IEEE Transactions on Circuits and Systems*, Vol. CAS-32, No. 10, pp. 1056-1060, October 1985.

[Leu88] A. Y. T. Leung, "A Simple Dynamic Substructure Method," *Earthquake Engineering and Structural Dynamics*, Vol. 16, pp. 827-837, 1988.

[Lin88] F. A. Lindholm and C. T. Sah, "Circuit Technique for Semiconductor-Device Analysis with Junction Diode Open Circuit Voltage Decay Example," *IEEE Transactions on Solid-State Electronics*, Vol. 31, No. 2, pp. 197-204, 1988.

[Mac71] R. H. MacNeal, "A Hybrid Method of Component Mode Synthesis," *Computers and Structures*, Vol. 1, pp. 581-601, 1971.

[Mac90] B. E. MacNeal, J. R. Brauer, and R. N. Coppolino, "A General Finite Element Vector Potential Formulation of Electromagnetics Using a Time-Integrated Electric Scalar Potential," *IEEE Transactions on Magnetics*, Vol. 26, No. 5, pp. 1768-1770, September 1990.

[Man87] P. Mancini, C. Turchetti, and G. Masetti, "A Non-Quasi-Static Analysis of the Transient Behavior of the Long Channel MOST Valid in All Regions of Operation," *IEEE Transactions on Electron Devices*, Vol. 34, pp. 325-334, Feb. 1987.

[Man93] H. A. Mantooth and A. R. Hefner, "Electro-Thermal Simulation of an IGBT PWM Inverter," *IEEE Power Electronics Specialists Conference Record*, University of Washington, Seattle, 1993, pp. 75-84.

[Mas85] P. Masse, B. Morel, and T. Breville, "A Finite Element Prediction Correction Scheme for Magneto-Thermal Coupled Problem During Curie Transition," *IEEE Transactions on Magnetics*, Vol. MAG-21, No. 5, pp. 1871-1873, 1985.

[Max93] MAXWELL User's Manual, ANSOFT Corporation, Pittsburgh, PA, 1993.

[May88] I. D. Mayergoyz and G. Friedman, "Generalized Preisach Model of Hysteresis," *IEEE Transactions on Magnetics*, Vol. 24, No. 1, pp. 212-217, Jan. 1988.

[May91] I. D. Mayergoyz, *Mathematical Model of Hysteresis*, Springer-Verlag, New York, 1991.

[Mcc88] W. J. McCalla, *Fundamentals of Computer-Aided Circuit Simulation*, Kluwer Academic Publishers, Boston, 1988.

[Mei81] L. Meirovitch and A. L. Hale, "On the Substructure Synthesis Method," *AIAA Journal*, Vol. 19, No. 7, pp. 940-947, July 1981.

[Mei91] L. Meirovitch and M. K. Kwak, "Rayleigh-Ritz Based Substructure Synthesis for Flexible Multibody Systems," *AIAA Journal*, Vol. 29, No. 10, pp. 1709-1719, October 1991.

[Mei92] L. Meirovitch and M. K. Kwak, "Inclusion Principal for the Rayleigh-Ritz Based Substructure Synthesis," *AIAA Journal*, Vol. 30, No. 5, pp. 1344-1351, May 1992.

[Meu88] G. Meunier et al., "Modelisation of 2D and Axisymmetric Magnetodynamic Domain by the Finite Element Method," *IEEE Transactions on Magnetics*, Vol. 24, No. 1, pp. 166-169, January 1988.

[Mih92] F. Mihalic et al., "IGBT SPICE Macro Model," *IEEE IECON (Industrial Electronics, Control and Instrumentation) Conference Record*, San Diego, California, 1992, pp. 240-245.

[Moo81] B. C. Moore, "Principal Component Analysis in Linear Systems: Controllability, Observability, and Model Reduction," *IEEE Transactions on Automatic Control*, Vol. AC-26, No. 1, pp. 17-32, February 1981.

[Nai90] S. R. Naidu, "Simulation of the Hysteresis Phenomenon Using Preisach's Theory," *IEE Proceedings*, Vol. 137, Pt. A, No. 2, pp. 73-79, March 1990.

[Nar66] K. S. Narendra and P. G. Gallman, "An Iterative Method for the Identification of Nonlinear Systems Using a Hammerstein Model," *IEEE Transactions on Automatic Control*, Vol. 12, pp. 546-550, July 1966.

[Nel92] D. J. Nelson and J. P. Jessee, "A Coupled Thermal Magnetic Model for High Frequency Transformers: Part I - Model Formulation and Material Properties," *IEEE Transactions on Components Hybrids, and Manufacturing Technology*, Vol. 15, No. 5, pp. 730-739, October 1992

[Oha94] R. C. O'Handley, EMA6938 (*Magnetic Material Properties*) class notes, University of Florida, Spring 1994.

[Ong91] C. K. Ong, P. O. Lauritzen and I. Budihardjo, "A Mathematical Model for Power MOSFET Capacitances," *IEEE Power Electronics Specialists Conference Record*, Massachusetts Institute of Technology, Cambridge, 1991, pp. 423-429.

[Ozi80] M. N. Ozisik, *Heat Conduction*, John Wiley & Sons, New York, 1988.

[Par92] H. J. Park, P. K. Ko, and C. Hu, "A Non-Quasi-Atatic MOSFET Model for SPICE - AC Analysis," *IEEE Transactions on Computer Aided Design*, Vol. 11, No. 10, pp. 1247-1257, October 1992.

[Pau83] J. J. Paulos and D. A. Antoniadis, "Limitation of Quasi-Static Capacitance Models for the MOS Transistor," *IEEE Transactions on Electron Device Letters*, Vol. EDL-4, pp. 221-224, 1983.

[Per95] A. M. Pernia, F. Nuno, and J. M. Lopera, "1D/2D Transformer Electric Model for Simulation in Power Converters," *IEEE Power Electronics Specialists Conference Record*, Atlanta, Georgia, 1995, pp. 1043-1049.

[Pil90] L. T. Pillage and R. A. Rohrer, "Asymptotic Waveform Evaluation for Timing Analysis," *IEEE Transactions on Computer Aided Design*, Vol. 9, No. 4, pp. 352-366, April 1990.

[Pre35] V. F. Preisach, "UberDie Magnetische Nachwirkung," *Zeitschrift fur Physik*, Bd. 94, p. 277, 1935.

[Pre92] W. H. Press et al., *Numerical Recipes in C--The Art of Scientific Computing*, 2nd edition, Press Syndicate of the University of Cambridge, Cambridge, 1992.

[Rac92] A. Rachid and G. Hashim, "Model Reduction via Schur Decomposition," *IEEE Transactions on Automatic Control*, Vol. 37, No. 5, pp. 666-668, May 1992.

[Ram95] S. Ramakrishnan, *Development and Application of Geometry-Dependent Field-Equivalent Model for Power Magnetics*, Master's Thesis, University of Florida, Gainesville, 1995.

[Rub75] S. Rubin, "Improved Component-Mode Representation for Structural Dynamic Analysis," *AIAA Journal*, Vol. 13, No. 8, pp. 995-1006, August 1975.

[Sab92] *SABER User's Guide*, 3.1a edition, Analogy Inc., Beaverton, Oregon, 1992.

[Saf89] M. G. Safonov and R. Y. Chiang, "A Schur Method for Balanced-Truncation Model Reduction," *IEEE Transactions on Automatic Control*, Vol. 34, No. 7, pp. 729-733, July 1989.

[Sah70] C. T. Sah, "The Equivalent Circuit Model in Solid-State Electronics - III," *IEEE Transactions on Solid-State Electronics*, Vol. 13, pp. 1547-1575, 1970.

[Sal90] S. J. Salon et al., "Coupling of Transient Fields, Circuits, and Motion Using Finite Element Analysis," *Journal of Electromagnetic Waves and Applications*, Vol. 4, No. 11, pp. 1077-1106, 1990.

[Sco90] R. S. Scott and G. A. Franz, "An Accurate Model for Power DMOSFETs Including Interelectrode Capacitances," *IEEE Power Electronics Specialists Conference Record*, Texas A&M University, San Antonia, Texas, 1990, pp. 113-119.

[She91] K. Shenai, "A Circuit Simulation Model for High-Frequency Power MOSFET's," *IEEE Transactions on Power Electronics*, Vol. 6, No. 3, pp. 539-547, July 1991.

[She93] Z. Shen and T. P. Chow, "Modeling and Characterization of the Insulated Gate Bipolar Transistor (IGBT) for SPICE Simulation," *IEEE Conf. Rec. in 5th International Symposium on Power Semiconductor Devices and ICs*, 1993, pp. 165-170.

[Ske80] R. E. Skelton and P. C. Hughes, "Modal Cost Analysis for Linear Matrix-Second-Order Systems," *Journal of Dynamic Systems, Measurement, and Control*, Vol. 102, pp. 151-158, September 1980.

[Ske83] R. E. Skelton and A. Yousuff, "Component Cost Analysis of Large Scale Systems," *International Journal of Control*, Vol. 37, No. 2, pp. 285-304, 1983.

[Ske88] R. E. Skelton, *Dynamic Systems Control: Linear Systems Analysis and Synthesis*, John Wiley & Sons, New York, 1988.

[Ski82] G. G. Skitek and S. V. Marshall, *Electromagnetic Concepts and Applications*, Prentice-Hall, Englewood Cliffs, New Jersey, 1982.

[Su89] T. J. Su and R. R. Craig, "Model Reduction and Control of Flexible Structures Using Krylov Vectors," *Journal of Guidance, Control, and Dynamics*, Vol. 14, No. 2, pp. 260-267, March - April 1989.

[Su91] T. J. Su and R. R. Craig, "Krylov Model Reduction Algorithm for Undamped Structural Dynamics Systems," *Journal of Guidance, Control, and Dynamics*, Vol. 14, No. 6, pp. 1311-1313, Nov.- Dec.1991.

[Sua88] L. E. Suarez and M. P. Singh, "An Exact Component Mode Synthesis Approach," *Earthquake Engineering and Structural Dynamics*, Vol. 16, pp. 293-310, 1988.

[Sua91] L. E. Suarez and M. P. Singh, "Successive Synthesis of Substructure Modes," *Journal of Applied Mechanics*, Vol. 58, pp. 759-765, 1991.

[Tak95] M. D. Takach and P. O. Lauritzen, "Survey of Magnetic Core Models," *IEEE Applied Power Electronics Conference Record*, Dallas, Texas, 1995, pp. 560-566.

[Tor88] E. D. Torre and G. Kadar, "Vector Preisach and the Moving Model," *Journal of Applied Physics*, Vol. 63, No. 8, pp. 3004-3006, April 1988.

[Tor90] E. D. Torre, J. Oti, and G. Kadar, "Preisach Modeling and Reversible Magnetization," *IEEE Transactions on Magnetics*, Vol. 26, No. 6, pp. 3052-3058, November 1990.

[Tsa93] C. Y. Tsai and D. E. Burk, "A Physical Charge-Based Model for the Steady-State and Transient Characteristics of the Power VDMOS," *SRC Techcon'93 Conference Record*, p. 533.

[Tsu93] I. A. Tsukerman, A. Konrad, and J. C. Sabonnadiere, "Coupled Field-Circuit Problems: Trends and Accomplishments," *IEEE Transactions on Magnetics*, Vol. 29, No. 2, pp. 1701-1704, March 1993.

[Tui88] P. W. Tuinenga, *SPICE--A Guide to Circuit Simulation & Analysis Using PSPICE*, Prentice Hall, Englewood Cliffs, New Jersey, 1988.

[Tur86] C. Turchetti, P. Mancini, and G. Masetti, "A CAD-Oriented Non-Quasi-Static Approach for the Transient Analysis of MOS IC's," *IEEE Journal of Solid-State Circuits*, Vol. Sc-21, pp. 827-836, 1986.

[Tzo93] Y. Y. Tzou and L. J. Hsu, "A Practical SPICE Macro Model for the IGBT," *IEEE IECON (Industrial Electronics, Control and Instrumentation) Conference Record*, Hawaii, 1993, pp. 762-766.

[Vec80] R. M. D. Vecchio, "An Efficient Procedure for Modeling Complex Hysteresis Processes in Ferromagnetic Materials," *IEEE Transactions on Magnetics*, Vol. 16, No. 5, pp. 809-811, September 1980.

[Vec82] R. M. D. Vecchio, "The Inclusion of Hysteresis Processes in a Special Class of Electromagnetic Finite Element Calculations," *IEEE Transactions on Magnetics*, Vol. 18, No. 1, pp. 275-284, January 1982.

[Ver93] N. K. Verghese, S. S. Lee, and D. J. Allstot, "A Unified Approach to Simulating Thermal and Electrical Substrate Coupling Interaction in ICs," *SRC Technical Report, SRC Pub C93222*, Carnegie Mellon University, April 1993.

[Vil87] C. De Villemagne and R. E. Skelton, "Model Reduction Using a Projection Formulation," *International Journal of Control*, Vol. 46, No. 6, pp. 2141-2169, 1987.

[Vla92] V. Vlatkovic et al., "Small-Signal Analysis of the Phase-Shifted PWM Converter," *IEEE Transactions on Power Electronics*, Vol. 7, No. 1, Jan. 1992.

[Wat85] J. K. Watson, *Applications of Magnetism*, published by the author, Department of Electrical Engineering, University of Florida, Gainesville, 1985.

[Wil82] E. L. Wilson and M. W. Yuan, "Dynamic Analysis by Direct Superposition of Ritz Vectors," *Earthquake Engineering and Structural Dynamics*, Vol. 10, No. 6, pp. 813-821, November 1982.

[Wil86] E. L. Wilson, M. Asce, and E. P. Bayo, "Use of Special Ritz Vectors in Dynamic Substructure Analysis," *Journal of structural Engineering*, Vol. 112, No. 8, pp. 1944-1954, August 1986.

[Wu93] B. S. Wu, C. T. Chuang, and K. Chin, "Non-Quasi-Static Effects in Advanced High-Speed Bipolar Circuits," *IEEE Journal of Solid-State Circuits*, Vol. 28, No. 5, pp. 613-617, May 1993.

[Xu88] C. H. Xu and D. Schroder, "Modeling and Simulation of Power MOSFETs and Power Diodes," *IEEE Power Electronics Specialists Conference Record*, Kyoto, Japan, 1988, pp. 76-83.

[Yee88] H. P. Yee and P. O. Lauritzen, "SPICE Models for Power MOSFETs; an Update," *IEEE Applied Power Electronics Conference Record*, New Orleans, Louisiana, 1988, pp. 281-289.

[You93] A. Yousuff and M. Breida, "Model Reduction of Mechanical Systems," *Journal of Guidance, Control, and Dynamics*, Vol. 16, No. 2, pp. 408-410, March/April 1993.

[Zie83] O. C. Zienkiewicz, C. Emson, and P. Bettess, "A Novel Boundary Infinite Element," *International Journal for Numerical Methods in Engineering*, Vol. 19, pp. 393-404, 1983.

[Zie89] O. C. Zienkiewicz and R. L. Taylor, *The Finite Element Method*, Vol.1, fourth edition, McGraw-Hill, New York, 1989.

BIOGRAPHICAL SKETCH

Jia-Tzer Hsu was born in Taiwan, the Republic of China, on October 26, 1962. He received the B.S. degree in electrical engineering from the National Cheng-Kung University, Taiwan, in 1984, and the M.S. degree in electrical engineering from the University of Florida, Gainesville, in 1990. He also obtained a second M.S. degree in engineering mechanics from a concurrent degree program at the University of Florida, in 1994. His Ph.D. work focuses on the development of CAD models and the formulations for electro-/magneto-thermal simulation of power semiconductor and magnetic devices.

I certify that I have read this study and that in my opinion it conforms to acceptable standards of scholarly presentation and is fully adequate, in scope and quality, as a dissertation for the degree of Doctor of Philosophy.

Khai D. T. Ngo, Chairman
Associate Professor of Electrical and Computer Engineering

I certify that I have read this study and that in my opinion it conforms to acceptable standards of scholarly presentation and is fully adequate, in scope and quality, as a dissertation for the degree of Doctor of Philosophy.

Loc Vu-Quoc, Cochairman
Associate Professor of Aerospace Engineering, Mechanics, and Engineering Science

I certify that I have read this study and that in my opinion it conforms to acceptable standards of scholarly presentation and is fully adequate, in scope and quality, as a dissertation for the degree of Doctor of Philosophy.

Dennis P. Carroll
Professor of Electrical and Computer Engineering

I certify that I have read this study and that in my opinion it conforms to acceptable standards of scholarly presentation and is fully adequate, in scope and quality, as a dissertation for the degree of Doctor of Philosophy.

Carla Schwartz
Assistant Professor of Electrical and Computer Engineering

I certify that I have read this study and that in my opinion it conforms to acceptable standards of scholarly presentation and is fully adequate, in scope and quality, as a dissertation for the degree of Doctor of Philosophy.

Kenneth O
Assistant Professor of Electrical and Computer Engineering

I certify that I have read this study and that in my opinion it conforms to acceptable standards of scholarly presentation and is fully adequate, in scope and quality, as a dissertation for the degree of Doctor of Philosophy.

Renwei Mei
Associate Professor of Aerospace Engineering, Mechanics, and Engineering Science

This dissertation was submitted to the Graduate Faculty of the College of Engineering and to the Graduate School and was accepted as partial fulfillment of the requirements for the degree of Doctor of Philosophy.

December 1995

for Winfred M. Phillips
Dean, College of Engineering

Karen A. Holbrook
Dean, Graduate School